

INVESTIGATION OF SURFACE EVOLUTION FOR
ABDOMINAL AORTIC ANEURYSMS INTERACTING WITH SURROUNDING TISSUES

By

Alexander C. Dupay

A THESIS

Submitted to
Michigan State University
in partial fulfillment of the requirements
for the degree of

MASTER OF SCIENCE

Engineering Mechanics

2012

ABSTRACT

INVESTIGATION OF SURFACE EVOLUTION FOR ABDOMINAL AORTIC ANEURYSMS INTERACTING WITH SURROUNDING TISSUES

By

Alexander C. Dupay

Three-dimensional patient-specific models of abdominal aortic aneurysms (AAAs) were reconstructed from CT scans and vessel migration, eccentricity, and cross-section line curvature were identified as morphological features which are influenced by surrounding tissues during disease progression. A novel centerline algorithm was developed in Matlab and applied capable of qualitatively estimating vessel migration away from the vertebrae during disease progression and automatically parameterizing patient-specific surface models with respect to the generated centerline. The parameterized surface is then approximated using shape functions and reconstructed appropriately. Image analysis and reconstruction was performed through a commercial biomedical imaging software suite for a high-resolution CT dataset consisting of 51 scans across 11 patients which were obtained through collaboration with Dr. Whal Lee at Seoul National University Hospital (SNUH). A longitudinal dataset, multiple scans taken at multiple times per patient, presents additional challenges such as the need for accurate model registration and the unique opportunity of increasing our understanding of geometrical evolution during the progression of AAA. This study discovers that a rich and complex biomechanical relationship exists between an AAA and the spine during AAA disease progression. The most significant implication of these results highlights the necessity of incorporating surrounding tissue, whether patient-specific or idealized, for computational biomechanics stress simulations of AAAs to improve their accuracy and prediction of rupture potential. Incorporating such interactions would also considerably enrich documented analyses.

ACKNOWLEDGEMENTS

I would like to thank Dr. Seungik Baek for his mentorship and the vast amount of knowledge and support he has imparted on me throughout our work together. I would like to thank my committee members Dr. Tamara Reid Bush and Dr. Thomas Pence for their time and insight with regards to this work. The same can be said for the colleagues I've had the pleasure of working with in my lab: Dr. Shahrokh Zeinali-Davarani, Dr. Jungsil Kim, Byron Zambrano R, Paul Snyder, and Jared Kavinsky. They all helped me further understand our field of study and helped shape my own studies as we worked together. Upon shaping my studies our collaboration with Dr. Lee was the invaluable basis of this thesis, and for that I am grateful. I had the pleasure of working with Drew Kim and Angela Kolonich during the Summer semester of my studies through the Research Education for Teachers (RET) program, and would like to acknowledge the support given to me by Drew Kim and the research help rendered by Angie. Outside the lab I would like to thank my friends and family and foremost my wife Cori, who have been there to support me every step of the way.

TABLE OF CONTENTS

LIST OF TABLES	vi
CHAPTER 1. Introduction.....	1
1.1 Motivation	1
1.1.1 Clinical Review of AAAs	1
1.1.2 Biomechanics Research of AAAs.....	5
1.1.3 Surrounding Tissues.....	11
1.2 Objectives	14
1.3 Contributions.....	16
CHAPTER 2. Biomedical Image Processing: Segmentation and Registration	19
2.1 Introduction.....	19
2.1.1 Biomedical Image Processing Background	19
2.1.2 Biomedical Imaging Modalities.....	20
2.2 Methods.....	25
2.2.1 Data	25
2.2.2 Segmentation.....	30
2.2.3 3-D Modeling.....	34
2.3 Results.....	38
2.4 Discussion	47
CHAPTER 3. Morphological Features Influenced by Surrounding Tissue	50
3.1 Introduction.....	50
3.2 Method	52
3.3 Results.....	54
3.4 Discussion	61
CHAPTER 4. Parameterization of Luminal and AAA Surfaces	64
4.1 Introduction.....	64
4.2 Methods.....	65
4.2.1 Importing the data	65
4.2.2 Centerline Generation Algorithm	67
4.2.3 Smooth Centerline Approximation.....	72
4.2.4 Longitudinal Acquisition Plane Generation.....	76
4.2.5 Parameterization of Cross Sections into $r(s, \theta)$	80
4.2.6 Coordinate transformation from $r(s, \theta)$ to (x, y, z)	82
4.2.7 Surface Approximation.....	84
4.2.8 Eccentricity and Polyline Curvature	88
4.3 Results.....	90
4.3.1 Centerline generation	90
4.3.2 Eccentricity and Curvature	92

4.4 Discussion	94
4.4.1 Centerline Generation Algorithm	94
4.4.2 Parameterization and Surface Approximation	97
4.4.3 Morphological Parameters	99
4.4.4 Future Work	102
APPENDICES	105
APPENDIX A. Detailed information and measurements of CT scan data.....	105
APPENDIX B. MatLab code developed for automatic parameterization of AAAs.....	111
APPENDIX C. Results of centerline and surface approximation algorithm performance.....	148
REFERENCES	159

LIST OF TABLES

Table 1. Patient age, number of scans, and sex after discounting irrelevant scans.	27
Table 2. Statistical summary of the CT dataset discounting irrelevant scans. The surveillance interval refers to the time between individual scans, such as between J1 and J2 or J4 and J5. The total study length refers to the total time between the first and last scan of a patient, such as between J1 and J5.	27
Table 3. Optimal STL model generation parameters used for every STL model generated in the study. Contour interpolation results in a smoother model with less gaps and is recommended for medical CT applications [59]. Matrix Reduction is set to 1, equivalent to no matrix reduction, which inherently nullifies the need to select a matrix reduction algorithm as well (not shown).	36
Table 4. The number of employed smoothing iterations at a constant smoothing factor of 0.7 on each STL model after optimal model generation. The smoothing was limited to a maximum of 10 iterations to avoid significant loss of detail.	36
Table 5. Summary of the definition of techniques employed over the survey of 56 studies by approximate percentage [51–53]. Some groups reported multiple methods of measurement to be in use rather than a single method, resulting in total percentages not equal to 100%.	52
Table 6. Linear approximation of annual transverse maximum AAA tissue diameter growth and R^2 fit value.	56
Table 7. Linear approximation of annual transverse maximum AAA lumen diameter growth and R^2 fit value.	59
Table 8. Conditional table for shape function assignment of smooth line approximation.	74
Table 9. Conditional table for calculation of θ from a given r_h vector. First it is determined whether θ lies on the N_2 , N_3 , $-N_2$, or $-N_3$ axis. If it does not lie on an axis than the region it lies in is determined and θ is calculated appropriately.	81
Table A.1. Detailed scan resolution information for the CT data set studied.	106
Table A.2. Detailed scanner manufacturers and models, date of scans, and total time elapsed from initial scanning.	107
Table A.3. Tissue Measurements from individual patient CT scans.	109
Table A.4. Lumen Measurements from individual patient CT scans.	110

Table C.1. SSE values from surface approximations sorted first by N_η and then by N_θ 152

Table C.2. SSE approximations sorted based on SSE values 155

LIST OF FIGURES

Figure 1. A sample CT scan of a patient diagnosed with an AAA highlighting a coronal slice (left, upper-left), a sagittal slice (left, upper-right), a transverse slice (left, bottom), and the intersection of all three (right). White arrows are used to identify the AAA. For interpretation of the references to color in this and all other figures, the reader is referred to the electronic version of this thesis. The text is not meant to be readable this figure and other CT reference figures, and is for visual reference only..... 2

Figure 2. Transverse slice of a patient CT scan in the abdominal region (left), and a zoomed section of a transverse slice in the abdominal region (right) focusing on AAA transverse cross-sections exhibiting varying thickness of the arterial wall due to ILT presence shown by the arrows. The intensity scale is adjusted on the right to show clear contrast between lumen, tissue, and intraabdominal space..... 5

Figure 3. Near the lumbar vertebrae (white) the inferior vena cava (blue) runs opposite to the aorta (red) on its right lateral side. The inferior vena cava and the aorta are connected, most notably for AAAs, to the renal system (purple). The left renal vein crosses anteriorly over the aorta inferior to the superior mesenteric artery..... 12

Figure 4. A process diagram highlighting key elements of the biomedical imaging process from data obtainment to generating technical computing models..... 20

Figure 5. A 3-D left side view of F1 after initial processing. The lower scan boundary is equivalent to the bottom of the image which clearly does not contain the abdominal cavity nor the full presence of an AAA. The scan F1 was therefore discounted from this study on the basis of insufficient data. 28

Figure 6. A 3-D transparent frontal view of the tissue surface (green, left) and the ELG (blue, left), and the luminal surface (red, right) and the ELG (blue, right) of scan H8. The presence of an ELG indicates this to be data from a post-EVAR scan, which is not the focus of this study. The scans H8 – H9 were therefore discounted from this study on the basis of irrelevant data.... 29

Figure 7. a 3-D view overlaid on a respective CT scan coronal plane for scan K4 (left) and for scan K6 (right). The shape of the AAA from scan K6 does not represent natural AAA disease progression; it instead more closely represents a post-EVAR geometry. The focus of this study is pre-EVAR AAAs and K6 is therefore fully discounted..... 29

Figure 8. A 3-D view overlaid on a respective CT scan coronal plane for scan E1. A thoracic aneurysm is present, but no AAA is present. The focus of this study is AAAs, so the scans are discounted. 30

Figure 9. A segmented mask for the arterial lumen (red) and arterial tissue (green) of scan B2 shown for a coronal slice (left) and transverse slice (right). The transverse slice (right) highlights the rectangular nature of voxels which occupy a segmented mask. The arterial tissue is seen to contain a wide region on the upper-left, or left anterior, side indicating the presence of an ILT. 33

Figure 10. A 3-D AAA lumen STL reconstructed from scan B2. STL format describes a triangularly meshed surface, as can be clearly seen. The data exported from the 3-D models for Chapters 3 & 4 uses point cloud format. This format will only contain the vertex information from STL models. 35

Figure 11. Front coronal plane view of 3-D luminal STL models generated for all 11 patients. From top-left to bottom-right in reading order the STLs originate from scans: A2, B3, C2, D3, E2, F7, G6, H7, I6, J6, K5. 39

Figure 12. Right sagittal plane view of 3-D luminal STL models generated for all 11 patients. From top-left to bottom-right in reading order the STLs originate from scans: A2, B3, C2, D3, E2, F7, G6, H7, I6, J6, K5. 40

Figure 13. A 3-D STL model of a reconstructed infrarenal AAA luminal surface as seen from the left sagittal plane (left), front coronal plane (center), and right sagittal plane (right). A bounding box indicates the infrarenal region specifically to be exported to a technical computing software package. 41

Figure 14. An example of two registered vertebral models from scans I1 & I3 as viewed from the left (left), front (center), and right (right). Each model is the same color, and has been registered to match the position of its pair. Near the top and bottom of the models clipping can sometimes be observed, which highlights the boundaries of a model (red). In general, however, it is clear that the models' positions match extremely closely given that they are independently generated from different CT scans. The associated lumen and tissue models are also automatically registered (not shown) according to the transformation matrix generated by minimizing the distance field between vertebral models. 42

Figure 15. Transparent and registered front coronal plane view (left) and right sagittal plane view (second from left) of 3-D luminal STL models for B1 and B3. Transparent and registered front coronal plane view (second from right) and right sagittal plane view (right) of 3-D tissue STL models for B1 and B3. The lumen and tissue models presented are not to scale, as the lumen models are inherently always smaller than the tissue models..... 43

Figure 16. Transparent and registered front coronal plane view (left) and right sagittal plane view (right) of 3-D luminal and tissue STL models for B3..... 44

Figure 17. A transverse slice un-zoomed (upper-left) and zoomed (upper-right) from scan A2. A 3-D reconstruction of the AAA tissue geometry for scan A2 from the right (bottom-left) and an opened version of the AAA tissue geometry for scan A2 from the right (bottom-right). Red circles indicate linked areas between images. Within the red circles it is clear that the AAA tissue is interacting with the spine and that the local geometry of the tissue is affected..... 45

Figure 18. A transverse slice un-zoomed (upper-left) and zoomed (upper-right) from scan A2. A 3-D reconstruction of the AAA tissue geometry for scan A2 from the left (bottom-left) and an opened version of the AAA tissue geometry for scan A2 from the left (bottom-right). Red circles indicate linked areas between images. Within the red circles it is clear that the AAA tissue is interacting with the spine and that the local geometry of the tissue is affected..... 46

Figure 19. Reconstructed 3-D models for the vertebrae (white), AAA lumen (red), and inferior vena cava tissue/lumen (blue) as seen from the left (left), front (center), and right (right) for scan B2..... 47

Figure 20. A sagittal slice (left) of scan J5 and a transverse slice (right) of scan J5 with the segmented lumen/tissue (red/green). The blue line indicates an anteroposterior maximum AAA tissue diameter measurement axis in the transverse plane (left, right), the solid red line indicates an anteroposterior maximum AAA tissue diameter measurement in the longitudinal plane (left), the dashed red line indicates a crude longitudinal axis approximation (left), and the orange line is simply the AAA tissue diameter measurement at 90° in the transverse plane to the anteroposterior measurement axis. The caliper positioning for this case was external/tissue..... 53

Figure 21. A transverse slice of scan D2 with the segmented lumen (red), maximum internal/lumen diameter axis (blue) and axis 90° to the maximum internal/lumen diameter (red). It is clear that anteroposterior measurements will not yield maximal results in the presence of an eccentric ILT. This is the reason that the maximum diameter axis was used and anteroposterior was not strictly used in all cases. 54

Figure 22. 3D CT reconstruction of patient C as viewed from the right. Two aneurysmal sacs are present and the primary is referred to as Patient C, while the secondary is referred to as Patient C (sac)..... 55

Figure 23. The maximum transverse diameter of the arterial tissue vs. scanning date for each patient..... 56

Figure 24. The annual expansion rate of maximum AAA tissue diameter growth calculated on a successive scan basis for each patient..... 57

Figure 25. The tissue eccentricity based on eccentricity = $(D_{\max}) / (D @ 90^\circ \text{ to } D_{\max})$ for each patient scan..... 58

Figure 26. The maximum transverse diameter of the arterial lumen vs. scanning date for each patient..... 59

Figure 27. The annual expansion rate of maximum AAA lumen diameter growth calculated on a successive scan basis for each patient..... 60

Figure 28. The lumen eccentricity based on eccentricity = $(D_{\max}) / (D @ 90^\circ \text{ to } D_{\max})$ for each patient scan..... 61

Figure 29. The coordinate planes inherited from the anatomical planes where the coordinate axis is such that the x-y plane is parallel to the transverse plane (green), the y-z is parallel to the sagittal plane (red), and the x-z plane is parallel to coronal plane (blue). 66

Figure 30. The arterial surface (blue) with two maximally inscribed spheres (red) and their respective constraint planes (green) shown. The centerline (black) is shown within the lumen model for scan B2 as seen from an isometric point of view (left), parallel to the x-z or coronal plane (center), and the y-z or sagittal plane (right). 67

Figure 31. The lumen point cloud model for scan B2 colored by z-coordinate values with a red sphere at approximately (155, -180, -163) (left), and the sphere itself colored by z-coordinate values with vectors indicating the orientations of vectors *A* (blue), *B* (black), and *C* (red) for a sample center point (right). 70

Figure 32. The final collection of centerline points plotted within the lumen point cloud model for scan B2 colored by z-coordinate value as seen from an isometric point of view (left), parallel to the x-z or coronal plane (center), and the y-z or sagittal plane (right). 71

Figure 33. The meaning of *p*, *d*, and *l* can be hard to ascertain from equations alone. The variable *d* represents the point to point distances between *p* values. The variable *l* represents the sum of *d* values thus far at a given *l*. 72

Figure 34. The final collection of centerline points plotted within the point-cloud lumen model of scan B2 colored by z-coordinate value and the fitted centerline (black) as seen from an isometric point of view (left), parallel to the x-z or coronal plane (center), and the y-z or sagittal plane (right). 76

Figure 35. The vectors N_1 (red), N_2 (blue) and N_3 (green) are plotted for each *s* originating from the points X_k for $k = [1, m]$ for the lumen model of scan B2. 77

Figure 36. The imported point-cloud lumen model composed of points q_N for scan B2 colored by z-coordinate value with points on the smooth approximated centerline shown (black, left), and the subset of points v_h colored by z-coordinate value from the point-cloud lumen model for scan B2 which lie on longitudinal planes defined by (N_1, N_2, N_3) (right). For example, the vectors in r_h from X_k to the associated points on the surface v_h at the plane defined by (N_1, N_2, N_3) for $k = 40$ are shown in green (right). 78

Figure 37. The radii values are calculated for all *h* by $\|r_h\|$. The mean is then calculated at each longitudinal plane for the lumen of scan B2 (left), and the circles of mean longitudinal radii at each longitudinal plane can be visualized for the lumen of scan B2 (right). 80

Figure 38. Schematic representation for the calculation of θ from a given r_h vector. First it is determined whether θ lies on the N_2 , N_3 , $-N_2$, or $-N_3$ axis (left), and if it does not lie on an axis then the region it lies in is determined and θ is calculated appropriately (right). 82

Figure 39. Parameterized surface data (red) from scan B2 shown as $r(s, \theta)$ surface..... 83

Figure 40. Subset of the original point cloud data which lie on longitudinal planes (left) and the data reconstructed from the $r(s, \theta)$ data (right). 84

Figure 41. A sample arterial lumen surface from scan C2 (left) is shown to undergo the steps of parameterization (center) followed by surface approximation (right) with the optional reconstruction to Cartesian coordinates shown for clarity in both cases. 85

Figure 42. Parameterized surface data (red) and the respective points from the best fit surface (blue) from scan B2 shown as $r(s, \theta)$ surfaces..... 87

Figure 43. Plot of the residual error between the parameterized surface data and the respective points from the best fit surface from scan B2 shown as an $r(s, \theta)$ surface. 87

Figure 44. Parameterized surface data (red) and the respective cross-sectional lines from the best fit surface (blue) from scan B2 shown as $r(s, \theta)$ surfaces..... 88

Figure 45. Major axis (left, red) and minor axis (left, green) of a cross-section (blue) used for eccentricity determination. Terminology of the 3-point polyline curvature method is detailed (right). 89

Figure 46. Isometric view of the centerlines (left) and a transverse view (right) for scans H1 – H5 where black, blue, green, red, cyan, magenta represent H1, H2, H3, H4, H5, H6 respectively. In this case the general region of the spine is the x-z plane at $y = 100$ such that the arrow indicates migration away from the spine. 91

Figure 47. x-z/frontal/coronal view of the centerlines (left), and y-z/sagittal view of the centerlines (right) for scans H1 – H5 where black, blue, green, red, cyan, magenta represent H1, H2, H3, H4, H5, H6 respectively. In the x-z plane (left) migration of the vessel centerline is taking place towards the left, and in the y-z plane (right) migration is also taking place towards the left. In this case the general region of the spine is the x-z plane at $y = 100$ such that the arrow indicates migration away from the spine. 92

Figure 48. Eccentricity parameter values displayed for B2 lumen before surface approximation with a cutoff of 1.4 (left) and after surface approximation (right)..... 93

Figure 49. Curvature parameter values displayed for B2 lumen after surface approximation with a cutoff of mean + 1 standard deviation. 94

Figure 50. SSE values curve sorted by N_η and N_θ for 100 cases of shape function surface fitting. 99

Figure 51. SSE values curved sorted by SSE value for 100 case of shape function surface fitting. 99

Figure 52. Eccentricity of the arterial lumen surface of B2 pre-fit (blue) and post-fit (red). 101

Figure C.1. A 3-D model of the lumen for D3 as seen in the x-z plane (upper-left), a coronal, or x-z, slice from scan D3 (upper-right), an x-z (bottom-left), and a y-z (bottom-right) view of the centerline algorithm results for scan D3. It is clear that scan D3 features a geometric anomaly. This anomaly is highly unusual and tends to force the centerline generation to follow the observed path regardless of input parameters. 149

Figure C.2. An x-z (left) and y-z (right) view of the centerline algorithm results from scan F5. If the final approximation of a centerline point differs greatly from the initial guess, the vector between the previous centerline point and current centerline point becomes more extreme. In the case when the vector points directly at a vessel boundary the algorithm will tend to fail. This failure occurs because the minimum distance vector is nearly parallel to the axis normal to the projection plane used for translations, resulting in near-zero translational adjustment vectors. The algorithm assumes that at any given two points the vector between them is relatively parallel to the centerline of the vessel. 150

Figure C.3. An x-z (left) and y-z (right) view of the centerline algorithm results from scan H5. If the final approximation of a centerline point differs greatly from the initial guess, the vector between the previous centerline point and current centerline point becomes more extreme. In the case when the vector points directly at a vessel boundary the algorithm will tend to fail. This failure occurs because the minimum distance vector is nearly parallel to the axis normal to the projection plane used for translations, resulting in near-zero translational adjustment vectors. The algorithm assumes that at any given two points the vector between them is relatively parallel to the centerline of the vessel. For this case the algorithm was able to recover, but it resulted in a large erroneous region before recovery. 151

Figure C.4. An x-z (left) and y-z (right) view of the centerline algorithm results from scan K3. It is unclear why the centerline fluctuated from its expected center, but it is clearly erroneous and requires adjustment of operating parameters. 151

KEY TO ABBREVIATIONS

AAA – Abdominal Aortic Aneurysm

COPD – Chronic Obstructive Pulmonary Disease

CT – X-ray Computed Tomography

DICOM – Digital Imaging and Communications in Medicine

ELG – Endoluminal Graft

EVAR – Endovascular Aneurysm Repair

FEA – Finite Element Analysis

FSI – Fluid Structure Interaction

G&R – Growth and Remodeling

HU – Hounsfield Unit

ILT – Intraluminal Thrombus

MPR – Multi Planar Reconstruction

MRI – Magnetic Resonance Imaging

NMR – Nuclear Magnetic Resonance

PWS – Peak Wall Stress

RF – Radio Frequency

SSE – Sum of the Square Error

STL – Standard Tessellation Language

SNUH – Seoul National University Hospital

US - Ultrasound

CHAPTER 1. Introduction

1.1 Motivation

1.1.1 Clinical Review of AAAs

The aorta is the major artery which blood circulates through from the heart. It can be segmented into different sections such as the aortic arch, thoracic aorta, and abdominal aorta, or ascending and descending aorta. The infrarenal aorta is the section of the abdominal aorta which lies between the renal branches and the iliac bifurcation. The normal diameter of the infrarenal aorta is approximately 2 cm. An aortic aneurysm is identified as an enlargement of the aorta greater than 50% of the normal diameter, or in the case of the infrarenal aorta a diameter of greater than 3 cm (Figure 1). Aneurysms affecting part of the vessel's circumference are known as saccular, while those affecting an area spanning the entire circumference are known as fusiform. The vast majority of aortic aneurysms are AAAs (abdominal aortic aneurysms), and over 90% of AAAs occur specifically within the infrarenal aorta [1–3]. AAAs are a serious medical condition that when left untreated ends in vessel rupture with patient mortality rates up to 95% [4], [5]. AAAs are responsible for at least 10,000 deaths annually in the U.S. alone [1], [6], [7].

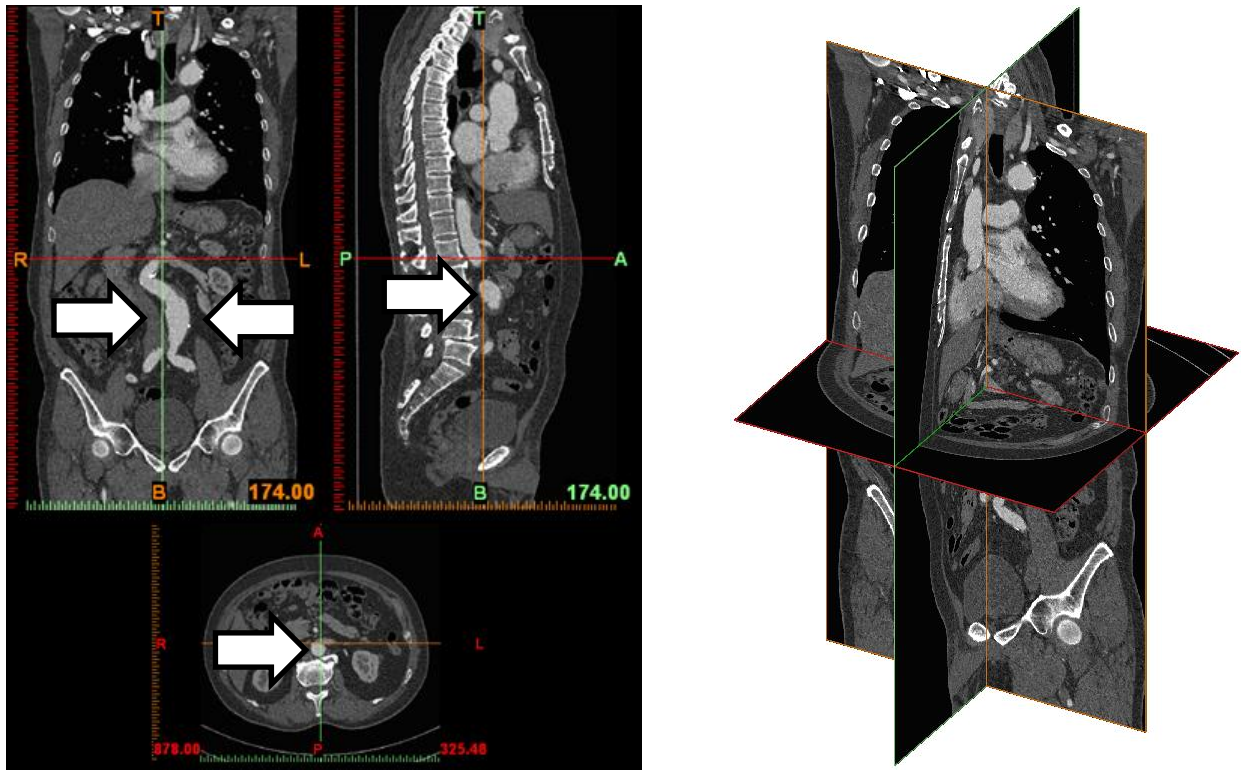


Figure 1. A sample CT scan of a patient diagnosed with an AAA highlighting a coronal slice (left, upper-left), a sagittal slice (left, upper-right), a transverse slice (left, bottom), and the intersection of all three (right). White arrows are used to identify the AAA. For interpretation of the references to color in this and all other figures, the reader is referred to the electronic version of this thesis. The text is not meant to be readable in this figure and other CT reference figures, and is for visual reference only.

The highest risk group is men over 65 years of age, and AAAs are less common for women than men and for individuals of black race/ethnicity [8]. The reasoning for this is not clear, and studies are underway suggesting things such as hormones and different anatomically influenced gender-based hemodynamics in the abdomen due to reproductive organs as possible reasons for gender differences while differences between race/ethnicity are harder to discern. Other risk factors include smoking, chronic obstructive pulmonary disease (COPD), high cholesterol, atherosclerosis, and hypertension; approximately 50% of individuals with AAAs also have hypertension [1], [2], [9]. Arterial tissue consists of three layers: the intima, media,

and adventitia. Loss of medial tissue and atherosclerosis, the stiffening of vessels due to internal plaque buildup commonly from high cholesterol, are the most common causes of AAAs. AAAs are usually asymptomatic until rupture, but can be associated with lower back and abdominal pain as they progress; as an AAA's size increases it may become palpable and/or tender [1], [10]. Rupture risk is the ultimate complication which clinicians consider for surgical decisions; rupture risk for aortic aneurysms with diameters larger than 5 cm, 6 cm, and 7 cm are approximately 20%, 40%, and 50% respectively based on documented diameters immediately following rupture [4], [9].

Currently medical professionals consider one geometrical parameter as the ultimate indicator of rupture risk for a patient diagnosed with an AAA: the maximum cross-sectional diameter. If the maximum cross-sectional diameter exceeds 5.0 cm or 5.5 cm an elective surgical intervention, either open surgical repair or EVAR (endovascular aneurysm repair), is suggested. Aortic replacement with a prosthetic graft was first introduced in 1952 by DuBost and has been the treatment of choice until the introduction of transfemoral intraluminal graft implantation in 1991 by Parodi [11], [12]. Implanting an ELG (endoluminal graft) promotes beneficial tissue remodeling to decrease the aneurysm sac size by redirecting blood to flow through the ELG to relieve pressure from the weakened aortic wall [13–15]. AAA research is usually divided into two sub-fields: the study of the natural progression of AAAs pre-EVAR, and the healing/recovery process of AAAs post-EVAR. This thesis will focus on pre-EVAR AAA pathology and biomechanics.

The 5.0 cm to 5.5 cm maximum cross-sectional diameter criteria was developed to set a clear boundary where the risk of rupture becomes appreciably greater than the risks involved in surgery, which has mortality rates of up to 5.8% - 6% [16], [17]. Statistically significant studies suggest continued monitoring for patients in lieu of early elective surgery carries a lower rate of mortality [7], [17], [18]. This diagnosis can best be made through the attainment of an Ultrasound (US), X-Ray Computed Tomography (CT), or Magnetic Resonance Imaging (MRI) screening of the region of interest for an individual; it is estimated that physical examination alone can miss more than one third of diagnoses [15], [19]. After the initial diagnosis is made, patient monitoring is required for an expansion rate to be determined and for general AAA stability to be assessed. From such scans parameters can be defined and analyzed based on morphological features to develop more sophisticated measures and attainment algorithms that account for more factors inherent to patient variance. Doing so will allow clinicians and patients to make more informed treatment decisions and allow for the more accurate estimation of rupture risk. Perhaps the least understood part of AAA pathology and rupture risk is the influence of an intraluminal thrombus (ILT) though clinical studies have shown that 75% of AAAs contain ILT [20]. An ILT is essentially a blood clot within the vessel which adheres to the intraluminal surface (Figure 2). Formation of an ILT is influenced by hemodynamic and biochemical factors.



Figure 2. Transverse slice of a patient CT scan in the abdominal region (left), and a zoomed section of a transverse slice in the abdominal region (right) focusing on AAA transverse cross-sections exhibiting varying thickness of the arterial wall due to ILT presence shown by the arrows. The intensity scale is adjusted on the right to show clear contrast between lumen, tissue, and intraabdominal space.

1.1.2 Biomechanics Research of AAAs

1.1.2.1 Introduction

The primary goals of current research of small pre-EVAR AAAs are the accurate quantification of morphological features and the accurate estimation of mechanical stress experienced by the arterial wall. Doing so builds a greater understanding of AAA disease progression on an individual level such that the estimation of rupture risk can shift from general statistic probabilities to estimates tailored to patient specific concerns. There exists much controversy on the merits of surgery for small AAAs less than 5-cm in diameter. In general it is assumed the risks of surgery outweigh the risk of rupture for such cases, but rupture of small AAAs is still responsible for high mortality rates [21], [22]. Understanding patient specific biomechanics is most beneficial for treatment decision making with regards to small AAAs

where rupture risk may exceed surgical risks but the AAA maximum diameter criterion suggests otherwise.

1.1.2.2 Arterial Wall Mechanics

Technical studies tend to focus on the geometrical analysis and finite element simulation of 3-D models generated from the segmentation of 2-D multi planar reconstructions (MPRs) of CT scans, which introduces the additional step of 3-D model generation. Many research groups have reconstructed 3-D AAA geometries from CT scans with the aim of evaluating wall stress through conventional finite element analysis (FEA). Giannoglou et al. evaluated peak wall stress (PWS) and found good correlation between PWS and mean centerline curvature, maximum centerline curvature, and maximum centerline torsion, but not with maximum diameter, the standard clinical correlation [23]. They based the surrounding tissue model on a uniform wall thickness derived from Raghavan and Vorp, whom are leading experts on AAA tissue wall material mechanics [24].

There have been significant developments for computational biomechanical models. Doyle et al. evaluated wall stress via FEA using validated realistic nonlinear material properties in an attempt to correlate wall stress to diameter and centerline asymmetry, finding that posterior wall stress increases with anterior centerline asymmetry by 38% [25]. Raghavan et al. incorporated a nonlinear biomechanical computational AAA tissue model in place of a conventional model into the reconstructed geometries to evaluate wall stress distribution, finding the PWS to be posterior in all cases and showing that AAA volume is a better predictor of PWS than maximum diameter, and therefore possibly a better indicator of rupture risk [26]. Wang et al. evaluated the effect of ILT on wall stress using a nonlinear large deformation algorithm

finding that PWS was reduced in the presence of ILT. The results showed an association between increase in ILT presence and decreases in peak wall stress of 6% - 38% from a range of 30 – 44 N/cm² to a range of 28 – 37 N/cm², compared to 12 N/cm² for a healthy aorta [20]. Georgakarakos et al. evaluated PWS in the presence and absence of an ILT and its relation to geometric parameters such as torsion, tortuosity, and mean curvature. They found a positive correlation between PWS and ILT volume, and in the presence of an ILT found significant correlation with the degree of centerline tortuosity and maximum diameter [27]. Speelman et al. focused on preserving wall calcifications, or mineralization of sections of the arterial wall, throughout 3-D model reconstruction and analyzing their effect on wall-stress [28]. Wall calcifications are an interesting part of AAA pathology which develop from unique biochemical conditions, but as they were rare in our dataset they were not modeled and considered. FEA methods quantifying wall stress have proven more effective than the maximum diameter measurement alone at predicting rupture risk. While it is clear AAA maximum diameter is not the measurement best correlated to rupture risk, it is not completely clear what is the best measure either.

1.1.2.3 Morphological Predictors of Arterial Wall Stress

There are a number of limitations when analyzing the clinical methods of rupture risk estimation. Simple parameters are not perfect measures and do not necessarily account for patient-specific information. This has prompted researchers to investigate more sophisticated parameters, but such investigations are also confronted with limitations. For example, it is known that the assumed 2 cm normal infrarenal aorta diameter can actually vary from 1.5-cm to 2.5-cm between individuals, but that a difference of 1 cm diameter can indicate much different

rupture risks [4], [9], [13]. Advanced geometrical parameter definitions & attainment algorithms will lead to more accurate risk predictions, increased sensitivity to patient-specific concerns, and form a foundation for defining more reliable indicators of rupture risk. Much research has been done to identify suitable geometric parameters to this end.

Martufi et al. evaluated geometric indices and validated an in-house automated software package, VESSEG, suggesting use of a geometrical index incorporating multiple morphological features [13]. Shum et al. evaluated geometric indices and regional variations in wall thickness based on novel segmentation algorithms [29]. A number of fluid structure interaction (FSI) simulations have also been performed in an attempt to link wall stress distribution to hemodynamic factors. Xenos et al. analyzed FSI with a focus on ruptured aneurysm [30]. Bluestein et al. analyzed FSI in the presence of ILT [31]. Fillinger et. al determined the wall stress distribution as a result of geometry and blood pressure using a hyperelastic nonlinear model [32]. Wolters et al. developed a novel patient-specific mesh generation algorithm to generate FSI meshes based on CT scan data [33]. Leung et al. compared a FSI model to a solid stress model [34]. Papaharilaou et al. performed a decoupled FSI-FEA simulation for estimating wall stress [35].

While not directly studying AAAs and CT scans, other works have contributed to the general discussion surrounding AAAs. Borghi et al. reconstructed 3-D geometries of thoracic aortic aneurysms from MRI by scanning the same region using different parameters optimized for resolution of the aneurysm lumen, thrombus, and wall to reconstruct a 3-D model detailing each component accurately [36]. Steinman et al. reconstructed a 3-D large intracranial aneurysm

model and performed a finite element computational fluid dynamics simulation of the 3-D pulsatile velocity field [37].

Current work makes frequent use of isolated patient-specific 3-D AAA geometries reconstructed from CT scans [13], [20], [23], [25–35]. Patient-specific 3-D aneurysm geometries are also useful for the study of thoracic aneurysms and large intracranial aneurysms [36], [37]. Conventional FEA wall stress studies for idealized and patient-specific geometries are more predictive of rupture than AAA maximum diameter, but many of these studies assume arterial tissue to be isotropic and linearly elastic as well as disregard vertebral interaction of an AAA during disease progression [23], [27], [28], [38–40]. The desire in the research community to use patient-specific models is clear, and the inclusion of longitudinal data and surrounding tissue would serve to directly enrich the findings of any of these existing works.

1.1.2.4 Intraluminal Thrombus

It has been shown that there is a correlation between an AAA diameter increase and ILT growth [41], [42]. It has been more recently suggested that there is not only an association, but that the ILT plays an active role in AAA pathology via mechanical stress shielding and pressure reduction [20], [43]. Such findings are important given that the basic mechanical definition of rupture of an AAA is when the wall stress at a surface exceeds the wall strength at that surface. Hinnen et al. extracted actual ILT samples and implanted them in model aneurysms composed of rubber and paraffin. The systolic circulatory pressure was measured as well as the systolic pressure at various depths within the ILT from the wall and it was found that the ILT served to reduce pressure as distance to the wall decreased. At 1 cm, 2 cm, and 3 cm from the wall pressure ratios between the systolic circulatory pressure and systolic ILT pressure were $0.9 \pm$

0.09, 0.86 ± 0.10 , and 0.81 ± 0.09 respectively [43]. The results carried two-fold importance: they experimentally verified the theory of stress-shielding presented by Wang [20], and they highlight the importance of considering ILT for FSI. The proper inclusion and modeling of ILT is another source of enrichment for current works, but there are significant challenges in such incorporation. Most technical studies of patient-specific AAAs reference CT data, which does not offer clear boundaries between the vessel wall and ILT. Idealized geometries often assume a uniform wall thickness ranging from 1.2 mm to 1.8 mm. High resolution CT scans can offer sub-millimeter resolution on the order of at least 0.5 mm / pixel, which does not offer a clear benefit over idealized thicknesses when other sources of error are taken into account. As ILTs become increasingly larger their accurate modeling becomes more realistic and worthwhile, however, as the error due to CT resolution is absolute and only a concern for low thicknesses.

1.1.2.5 Discussion

The weighing of rupture risk against surgical risk is the bottom line for treatment decision, and therefore a proper understanding of long-term AAA pathology and biomechanics is paramount to accurately estimating rupture risk. The last two decades have been a time of significant advancement for such understanding, leading to FEA / computational biomechanics studies utilizing patient-specific AAA geometries. Computational biomechanics considers vascular adaptations associated with AAA pathology through growth and remodeling (G&R) mathematical models. Conventional FEA is useful for studying present and short term deformations of patient-specific AAA geometries, but its inherent exclusion of vascular adaption limits its potential for long-term studies. The stress analyses of patient-specific AAA geometries producible through computational biomechanics have proven more effective than standard clinical measures at predicting rupture risk thereby affirming its potential usefulness, and

perhaps necessity, as a rupture risk assessment tool. One significant drawback hindering the incorporation of these methods clinically is their inability to explain why rupture occurs most often at the lateral / posterolateral regions of an AAA. There is no doubt that future expansion of studies not already doing so would benefit from the inclusion of patient specific geometries. It is clear from these studies that a generally accepted set of guidelines and methods exist for segmentation and model generation. For this study we additionally include the generation of the vertebrae model adjacent to the AAA for global registration.

1.1.3 Surrounding Tissues

The pathology of AAAs is such that enlargement of the aorta is associated with disease progression. As an AAA enlarges it becomes subject to increased reaction forces from surrounding tissue, especially from the vertebrae of the spine. The maximum diameter criterion may serve to distinguish stable and unstable aneurysms to an extent, but cannot necessarily explain the degree of stability. Back pain can be associated with AAAs due to aneurysm expansion exerting pressure on the lumbar nerve roots as a result of vertebral contact. It is also well known that there is an association between the presence of an AAA and vertebral erosion as well as evidence shown for ruptures tending towards the posterolateral surface of the aorta. There are not many studies that have been done considering the growth and remodeling interactions of an AAA, the lumbar region of the spine, the ILT, and surrounding tissues. Vorp et al. suggested that the “limitation of posterior expansion caused by the vertebral column might result in preferential anterior expansion of the aneurysmal wall and an asymmetric configuration” [44]. Watton et al. developed the first mathematical model to predict aneurysm growth including spinal contact based on this suggestion, but it was not paired with a

longitudinal study or additional tissue constraints [45]. In this study it is shown that different patients display different degrees of interaction with surrounding tissues. For a subset of the patients, however, a marked effect on AAA geometry is observed. Clearly defined morphological parameters describing these interactions would be of significant value.

The vena cava is the major vein for returning blood back to the heart. The superior vena cava returns blood from the upper half of the body to the heart while the inferior vena cava returns blood from the lower half of the body to the heart. The inferior vena cava, spine, renal system, and aorta interact as shown (Figure 3).

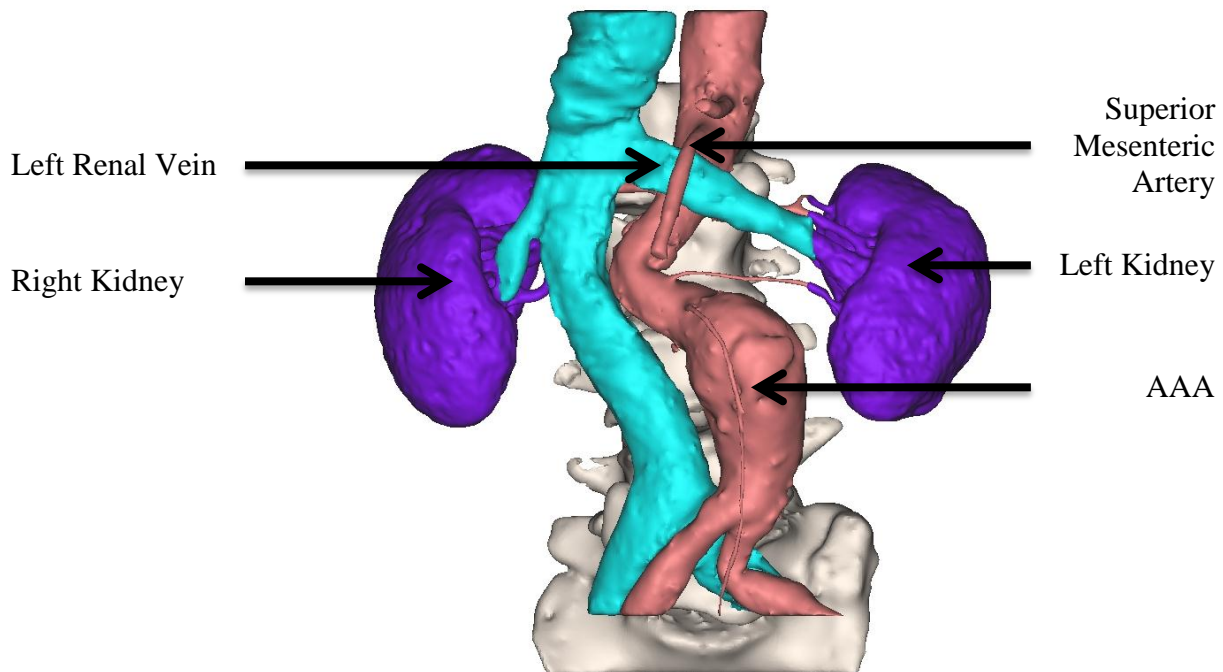


Figure 3. Near the lumbar vertebrae (white) the inferior vena cava (blue) runs opposite to the aorta (red) on its right lateral side. The inferior vena cava and the aorta are connected, most notably for AAAs, to the renal system (purple). The left renal vein crosses anteriorly over the aorta inferior to the superior mesenteric artery.

All renal arteries and renal veins segment and terminate at the respective kidneys. In healthy individuals the two vessels do not have substantial physical interaction, but in the presence of an AAA the inferior vena cava presents an asymmetric right-sided growth barrier to AAA geometrical evolution. Mean arterial blood pressure, which has a pulsatile flow, in healthy individuals usually ranges from 90 – 100 mm Hg compared to the non-pulsatile venous side of the circulation which is approximately 84 mm Hg less; mean venous blood pressure ranges from approximately 10 mm Hg at the venules to approximately 0 mm Hg at the heart [1]. Blood flow in the inferior vena cava is strongly influenced by the intraabdominal pressure (IAP), which typically ranges from 2 – 10 mm Hg [1]. When considering the influence of the inferior vena cava as a growth barrier of an AAA the mean venous pressure is thus far less influential than the biomechanical resistance the tissue itself provides.

Each kidney of the renal system is sheathed by a fibrous external capsule and surrounded by fatty connective tissue which, in combination with attached vessels and fascia, holds each kidney in place [1]. The kidneys have some freedom of movement to react to movement of the diaphragm, but otherwise remain relatively stable. As an AAA progresses it is possible for renal arteries or veins to become stressed or distended, though migration of the vessels is resisted by the other tissues serving to anchor the kidneys in place, most notably the left renal vein crossing anteriorly over the aorta.

The spine acts as a rigid boundary for AAA growth, and can therefore affect the remodeling of the aorta [44–46]. The interaction between vertebral contact & ILT position is also extremely important. It is believed that the circumferential position of an ILT can lead to

substantially different AAA growth & remodeling, especially with regards to accelerated tissue degradation. An anteriorly growing ILT may grow relatively unconstrained, while a posteriorly growing ILT presents additional considerations. Such an ILT could cause a general vessel centerline migration of the associated AAA away from the spine, as well as expose the posterior side of the associated AAA to compressive forces of the spine as a growth barrier. It is known that the arterial wall becomes thinner and weaker at areas contacting ILT, so it should be considered whether such an area is also contacting the spine and therefore under additional force. Additionally such a situation favors curvature flattening of the vessel at the region of spinal contact and such a geometrical profile changes the stress experienced by the vessel, especially at circumferential regions of significant and sudden curvature change.

1.2 Objectives

This thesis will detail an investigation of AAA surface evolution for a longitudinal CT scan dataset progressing from qualitative to quantitative methods. The identification of influential morphological features coupled with automated algorithms to obtain parameters representing those features will lend insight into the link between AAA pathology and AAA biomechanics and thereby provide a strengthening tool for computational biomechanics. In the selection of the parameters it is important that they should be intrinsically understood by medical professionals as integrated study of AAA pathology and biomechanics requires clear discourse between medical and research professionals. It is known that some morphological features arise from contact between an evolving AAA and vertebrae, but the impact of these effects on rupture risk is not fully known. The geometrical parameters investigated in this work will reflect interactions with surrounding tissues, most notably the lumbar vertebrae. A longitudinal study

serves to further justify the suitability of selected morphological parameters by investigating their respective evolution throughout AAA progression. Therefore the objectives of the study are as follows:

- Process a collection of CT scans to obtain fully segmented and registered 3-D models of the vertebral and arterial surfaces.
- Identify morphological features from the reconstructed CT scans and perform analysis akin to clinical measurements.
- Perform a relatively defined parameter study based on arterial centerlines generated by a developed program to assess morphological feature evolution during AAA progression.

Chapter 2 will introduce a working knowledge of medical image modalities such CT, MRI, and US. The advantages and disadvantages of each modality will be discussed with respect to AAA diagnosis, monitoring, and surgical planning. The processing methodology employed for our dataset will be covered in which 3-D models are reconstructed from CT scans. The sum of 3-D models for a patient form a longitudinal model set. Three dimensional models of the AAA luminal surface, AAA tissue surface, and lumbar vertebrae will be developed following established methods of image segmentation. Models belonging to longitudinal subsets of the data will additionally undergo an image registration process to find the spatial transform that maps their positions and orientations with respect to the lumbar vertebrae, which is assumed relatively unchanging over time. Image registration allows for an accurate investigation of the true spatial differences between scans at different times.

Chapter 3 will examine the CT scan slices concurrently with the generated 3-D models to identify morphological features influenced by surrounding tissue. It is theorized that certain morphological parameters may be more suitable for indicating or estimating rupture risk than the currently used maximum diameter criterion as such features may be indicative of unique sources of increased wall stress observable through FEA. Each CT scan will be imported to and visualized through biomedical imaging software for analysis and subsequent determination of suitable morphological parameters. Measurements of the maximum tissue and luminal diameters will be taken directly from the CT scans according to established clinical methodology.

Chapter 4 will cover parameterization of the surface. The centerline generation, smoothing, and parameterization of the surface will be described in detail. After parameterization of the surface is complete, the method for extracting morphological measurements from the surface will be covered. The centerlines serve as a reference, or an axis to parameterize the surface to, for each model which allows for parameterization of the surface and the relative definition of geometrical parameters. It is theorized that interaction with surrounding tissue, particularly the lumbar vertebrae, vena cava, and renal system, plays an important role in the evolution of the AAA surface geometry.

1.3 Contributions

It is believed that the evaluation of morphological parameters throughout AAA progression that can be used to quantify AAA surface evolution with respect to surrounding tissues is the pivotal next step in advancing the general understanding of AAA biomechanics.

Through collaboration with Dr. Whal Lee at Seoul National University Hospital (SNUH) in South Korea we have obtained a high resolution CT scan dataset for this purpose.

The influence of surrounding tissues is understudied in current works. Immediately upon visually reviewing the CT scans it could be seen that surrounding tissues, particularly the spine, were significantly interacting with the AAAs during their progression. A FEA or computational biomechanics study would typically involve the internal arterial pressure and vessel pre-stretch as the sole mechanical driving forces of surface evolution, but the addition of a growth barrier such as the lumbar vertebrae would introduce significant reaction forces. Considering the lumbar vertebrae would change the outcome of such simulations and offer more insight as to the complex biomechanics in effect under *in vivo* conditions. Consideration of the mechanical influence of other tissues such as the inferior vena cava, adipose tissue, and connective tissue would also lend insight into the link between AAA pathology and biomechanics, but the spine is focused upon for its clear contribution.

The dataset contains a total of 51 CT scans from 11 patients with a mean surveillance interval of 373 days between longitudinal scans allowing for the unique investigation of AAA surface evolution. Such data allows not only for the investigation of morphological parameter values, but their evolution as well. Studies including longitudinal data sets are seriously underrepresented as access to such data collections is rare, especially at high-resolutions. Typically 3-D meshes developed from patient-specific data are based on single CT scans of individual patients with no additional follow-up CT images for study, unlike access to a longitudinal dataset provides. The major contribution of this study is to showcase the

importance of considering surrounding tissue, particularly the spine, when performing stress studies and geometrical parameter indexing of ideal and patient-specific AAA geometries. The developed centerline algorithm is proposed to be superior to standard algorithms which calculate the 2-D transverse polyline centroids to develop a centerline [13], [23], [25], [29], [47–50].

CHAPTER 2. Biomedical Image Processing: Segmentation and Registration

2.1 Introduction

2.1.1 Biomedical Image Processing Background

This chapter serves to highlight the processes involved in fully visualizing and modeling the anatomical structure of an *in-vivo* patient-specific AAA. Medical professionals performing diagnosis, continued monitoring, or surgical planning of patients require clear visualization of the AAA geometry. Research groups performing morphological feature surveys, FEA, or growth and remodeling simulations of patient-specific AAA geometries need to have quantitative information about the geometry. In standard clinical practice the qualitative imaging resulting from US is most commonly used for diagnosis and continued monitoring. Use of CT and/or MRI scanning is typically reserved for surgical planning, though they offer the ability to record quantitative geometry data for delayed decision making and analysis [51–53]. From a qualitative image, whether from US, CT, or MRI, an accurate production of quantitative geometry measurements can result, though the AAA maximum external tissue diameter is the standard measure of interest. In clinical practice measurement is usually performed through the use of calipers on real-time US imaging [51–53]. Technical studies trying to quantify various parameters tend to focus on 3-D analyses, which involve additional processing of the data, usually CT scans, before analysis (Figure 4).

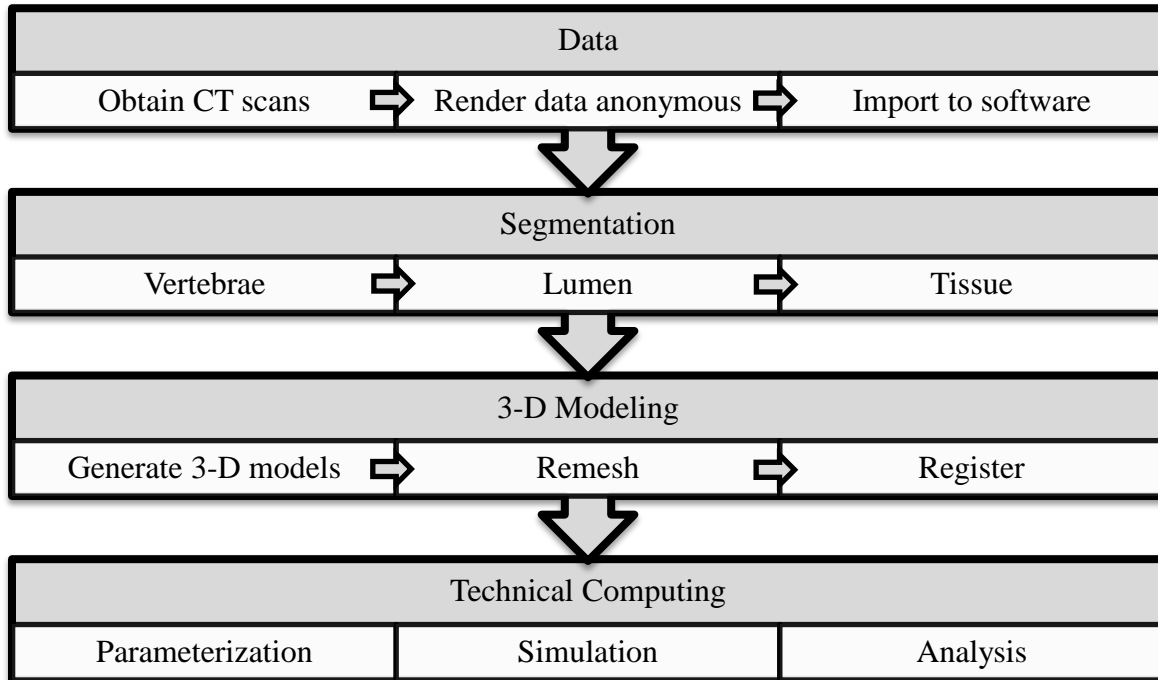


Figure 4. A process diagram highlighting key elements of the biomedical imaging process from data obtainment to generating technical computing models.

A brief review of the relevant biomedical imaging modalities is first presented. This serves to justify the use of CT scans seen by most studies and introduce key terminology associated with each modality. After this introduction the methods utilized for segmentation and 3-D modeling / image registration are covered.

2.1.2 Biomedical Imaging Modalities

To properly diagnose, perform continued monitoring, and perform surgical planning for an AAA, noninvasive imaging modalities are employed clinically; Acharya et al. provides an excellent resource to become familiar with noninvasive imaging modalities from which much of this summary is derived [54]. Noninvasive imaging modalities can visualize internal anatomical structures of the human body accurately and quickly, even providing real-time imagery in some

cases. With respect to diagnoses of AAAs US, MRI, and CT are the most widely favored modalities. A summary of each will be presented and discussed.

US refers to sound waves with high temporal frequencies. US imaging involves producing US signals, directing them to a particular area in the body with handheld probes, and receiving the signal at an appropriate detector array. Image reconstruction takes place in real-time on a monitor. As the signal passes through different layers of tissue and encounters tissue layer boundaries partial reflection and partial transmission of the signal occurs. There are a wide variety of electronic transducer arrays that can be employed to acquire different dimensionality and quality of this qualitative imagery, but the same basic principles apply for each setup. Many setups allow for the 2-D real-time visualization of structures within the body, which is particularly useful for cardiology. 3-D US was patented in 1987 but still sees contention for widespread clinical use mainly due to cost, training, and data storage [55]. US imaging is capable of not only acquiring qualitative imagery, but quantitative diagnostic information. Doppler Echocardiography, for example, can provide vector measurements of blood flow direction and magnitude. The major advantage of US is real-time feedback and equipment that is compact, lightweight, and of comparatively low-cost which also requires less specialized personnel compared to other imaging modalities' equipment.

MRI is based on Nuclear Magnetic Resonance (NMR), which is a phenomenon associated with physical chemistry. NMR was discovered in 1946 by Bloch and Purcell, who were later awarded the Nobel Prize in 1952 for the discovery, which was coincidentally the same year that aortic replacement surgery was introduced by DuBost [11], [54]. For an MRI scan a

magnetic field is generated and maintained enclosing the scanning area. MRI thus requires patients to be subject to extremely powerful magnetic fields within a gantry during the scanning process, which makes factors such as implants, pacemakers, and claustrophobia important to consider as contraindications. Radio Frequency (RF) energy is introduced into the scanning area to excite nuclei within the field, which releases RF energy as the MR signal to be recorded. The ideal element to perform MRI with is Hydrogen, which is also the most common element in biological tissue. MRI is capable of collecting images at any plane through a volume and is excellent for soft-tissue resolution. Automatic Multi Planar Reconstruction (MPR) of the image takes place after the scan data is reconstructed allowing for 3-D viewing of internal anatomical structures. MRI is extremely expensive and not widely available, rendering it an uncommon choice for AAA diagnosis and monitoring protocols. Usually MRI is only utilized for AAAs if an individual requires a CT scan but has contraindications for CT scanning.

CT scanning utilizes X-rays to acquire diagnostic images. A conventional radiograph produces a single 2-D image by placing the scanning area of a patient between an X-ray emitter and X-ray receiver. X-rays sent through the scanning area are linear and lose energy as they pass through tissue. The resultant X-ray energy is recorded for the field of view. The result is a radiograph, which is only a 2-D projection of a 3-D scanning area. CT, on the other hand, is capable of returning 3-D information as a series of 2-D slices based on the same principles. An X-ray source on one side of the scanning area propagates X-rays to an X-ray detector on the opposite side of the scanning area parallel through the axial plane. The detector is capable of electronically storing the information. Relative motion is applied to the system between the scanning apparatus and the scanning area such that the X-ray source and detector remain in the

axial plane, but at some fixed angle from their previous positions. The emission and detection process is repeated according to the parameters set by a given scanning algorithm. A total of 180° of rotation is required to fully image the plane in two dimensions. There exist many reconstruction algorithms, but in essence they all manage to reconstruct 2-D tissue density information from the saved collection of X-ray projection information. The 2-D imaged plane represents a finite 2-D matrix of tissue density values known as an axial or transverse slice. Slices have a thickness dimension, however, as well as a finite resolution as a result of the electronic digitization. Therefore each element of a slice matrix actually represents a voxel, or 3-D pixel, with dimensions fixed by the scanning algorithm and reconstruction algorithm. Some algorithms are inherent to the scanner used in that they produce identical resolution of data every time, but some scanners exist such as the Dynamic Spatial Reconstructor that are capable of dynamic algorithms to meet spatial resolution demands. CT scans are the method of choice for surgical planning of an AAA after US monitoring has identified the need for treatment [51–53].

There are advantages and disadvantages to US, MRI, and CT with respect to AAA diagnosis. US has the advantage of mobile compact equipment such that patient comfort is minimally affected whereas MRI and CT both require the patient to remain motionless during scanning, in addition to often presenting a claustrophobic environment which dissuades some patients from being comfortable with the process. US also presents both a low cost up-front for the medical provider and for the patient relative to MRI and CT which present much higher costs. US is additionally able to visualize motion of anatomical structures through real-time imaging and extract quantitative information such as blood flow direction and magnitude. If a medical professional wishes to quantify the maximum tissue diameter of an AAA for diagnosis

or continued monitoring, US provides a quick, low-cost, noninvasive method of accomplishing that goal, and studies have shown it is only marginally less reliable than CT for maximal diameter measurements [56]. Motion of the vessel from the cardiac cycle introduces intra-operator variability in maximal AAA tissue diameter measurements from US, however, and there is no standardized method to reduce this variability [57]. US sees widespread use in the United States as a diagnostic and monitoring tool as it provides clear information about AAA size. Obesity and the presence of bowel gas can render US diagnosis of an AAA less effective, however. AortaScan, a portable 3D ultrasound device which measures abdominal aortic tissue diameter automatically, was investigated against conventional CT scanning for the diagnosis of AAAs in 44 known AAA cases. Conventional CT diagnosis by trained screening personnel was able to correctly diagnose 43 / 44 cases, while AortaScan missed the diagnosis in 8 / 44 cases and reported 13 / 44 false positives [58]. This may not be a fault of US, but rather illustrates the shortcomings of automated diagnosis vs. the judgment of trained screening personnel. US is an ideal choice for visualizing small stable AAAs, but becomes inadequate when advanced investigation and/or surgical treatment planning is required.

CT and MRI are also effective at diagnosis, but considered unnecessary for small stable AAAs due to their higher cost, decreased patient throughput, lessened availability, and principle concerns. CT involves X-rays which are inherently harmful to tissue, and though permissible levels have been set, exposure should be limited as much as possible. In the case of CT for AAAs an intravenous dye is injected into the aorta to render the luminal volume easily differentiable from surrounding tissue. In some cases patients may have an allergic reaction or experience irritation of the kidneys due to the dye, especially patients with chronic kidney

concerns. For MRI the necessity of strong magnetic fields defines absolute contraindications for scanning. Such magnetic fields could disrupt the proper function of a pacemaker for example, as well as affect other implants in undesirable or fatal ways. US is the preferred clinical tool for initial diagnosis and continued monitoring due to low cost, wide availability, compact and mobile equipment, and minimal patient discomfort. If AAA disease progression warrants additional investigation and/or surgical planning CT scans with intravenous dye then become the preferred scanning method due to the clear and absolute depiction of volumetric information. CT scans are otherwise considered unnecessarily time and cost consuming for small stable AAAs even though they offer superior qualitative imagery [56]. If a patient has contraindications for CT scanning, MRI is then an adequate alternative for surgical planning. This review serves to illustrate the rarity of a longitudinal CT scan collection of small AAAs and the quality of information that can be extracted.

2.2 Methods

2.2.1 Data

A biomedical software, Mimics® (Materialise, Leuven, Belgium), is used to process the CT scans, which are axial/transverse slice stacks [59]. The software interface allows for viewing of up to 3 voxel domain, or slice, windows simultaneously through MPR and a 3-D rendering window. MPR is a general term that refers to the interpretation of additional planes based on known planes. Standard MPR results in the additional view of the sagittal and coronal planes from the transverse planes, but other methods exist that generate curvilinear planes based on arterial centerlines for example. Other commercial biomedical imaging software packages exist, as well as some in-house programs such as that used by Martufi et al. (VESSEG v.1.0.2,

Carnegie Mellon University, Pittsburgh, Pennsylvania) [13]. For the current study a collection of high resolution CT scans of patients with AAAs was obtained through collaboration with Dr. Lee's clinical group at SNUH according to an approved institutional IRB protocol; any identifiable information that could be traced back to the patient was removed prior to our obtainment of the dataset. Supplemental information was also provided: blood pressure measurements, age, and gender for each scan. Typically clinical small AAA monitoring is done using US, and a collection of CT scans of this caliber for small AAAs is rare, especially in the United States. Each scan features a contrast agent in the form of an intraluminal dye which renders the luminal volume easily differentiable from nearby tissue.

We obtained a total of 51 sets of CT images representing the longitudinal study of 11 patients termed patients A - K, with 2 to 9 sets of images from each patient and a mean surveillance interval of 373 days. The combination of patient ID and scan number will be adopted for this study such that the first scan from patient G would be known as scan G1, the second scan from patient G would be G2, etc. Of these 51 scans were included 3 post-EVAR scans, 2 thoracic aortic aneurysm scans, and 1 scan which failed to capture the AAA region completely.

Discounting the aforementioned scans reduces the dataset to a total of 45 sets of CT scans representing the longitudinal study of 10 patients, with 2 to 7 sets of images from each patient and a mean surveillance interval of 401 days. Each CT scan has dimensions of 512 px \times 512 px in the transverse plane and a 0° gantry tilt. The voxel resolution varies between scans as a result of the scanner brand/model, scanning algorithm, and reconstruction algorithm employed. The

total number of slices varies as well but usually includes the entire torso of the patient, presumably allowing for the additional diagnosis of thoracic aneurysms. It is possible for the geometry data to be scaled, but scaling of the entire dataset was at 100% upon obtainment and never altered or further considered henceforth. Patient information and a statistical summary of the scans are shown by Tables 1 and 2. More detailed information for every scan is located in Appendix A (Tables A.1 and A.2).

Table 1. Patient age, number of scans, and sex after discounting irrelevant scans.

Patient	# Scans	Age	Sex
A	2	68	M
B	3	71	M
C	2	69	M
D	3	63	F
F	6	78	F
G	6	65	M
H	7	68	M
I	6	66	M
J	5	54	M
K	5	62	M

Table 2. Statistical summary of the CT dataset discounting irrelevant scans. The surveillance interval refers to the time between individual scans, such as between J1 and J2 or J4 and J5. The total study length refers to the total time between the first and last scan of a patient, such as between J1 and J5.

# of Patients	10
Mean age	66.4
Minimum # scans	2
Maximum # scans	7
Mean # scans	4.5
Minimum surveillance interval	84 days
Maximum surveillance interval	1713 days
Mean surveillance interval	401 days
Minimum total study length	182 days
Maximum total study length	3325 days
Mean total study length	1502 days

Some scans were discounted from this study for different reasons, which are important to justify before moving on. Scan F1 is not focused on the abdominal region, and the scan is therefore fully discounted (Figure 5). Scans H8 – H9 are post-EVAR, and the presence of an ELG is clearly present (Figure 6). The focus of this study is AAAs pre-EVAR, and these scans are therefore fully discounted. Scan K6 appears to be post-EVAR but it is difficult to discern as no ELG is present, though it is possible a full aortic vessel graft is present (Figure 7). While the cause is unclear, it is clear that scan K6 does not represent natural progression of an AAA and the scan is therefore fully discounted. Scans E1 – E2 clearly feature a thoracic aneurysm only and the focus of this study is AAAs, so the scans discounted (Figure 8). Figures 5 - 8 clearly describe the reason for discounting the aforementioned scans and are detailed below. These figures feature 3-D results from the methodology covered in Chapter 2 for the sake of visual aid, but the same conclusions are clear from visual analysis of the CT scans without employing the methodology covered in Chapter 2.



Figure 5. A 3-D left side view of F1 after initial processing. The lower scan boundary is equivalent to the bottom of the image which clearly does not contain the abdominal cavity nor the full presence of an AAA. The scan F1 was therefore discounted from this study on the basis of insufficient data.

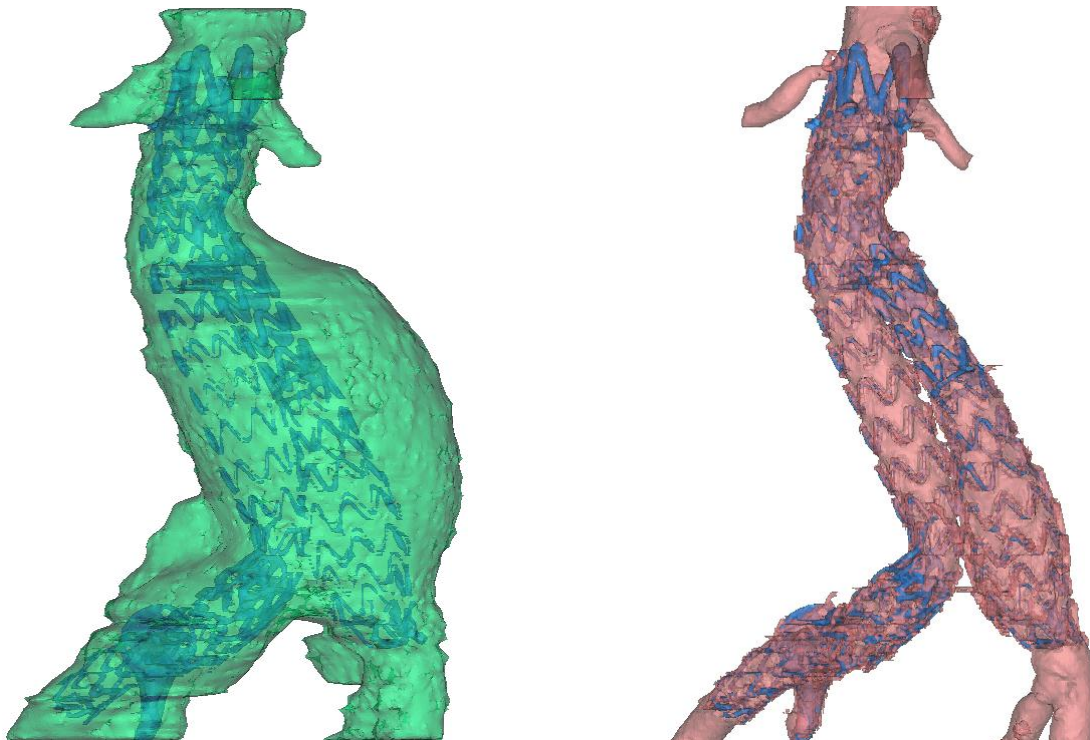


Figure 6. A 3-D transparent frontal view of the tissue surface (green, left) and the ELG (blue, left), and the luminal surface (red, right) and the ELG (blue, right) of scan H8. The presence of an ELG indicates this to be data from a post-EVAR scan, which is not the focus of this study. The scans H8 – H9 were therefore discounted from this study on the basis of irrelevant data.



Figure 7. a 3-D view overlaid on a respective CT scan coronal plane for scan K4 (left) and for scan K6 (right). The shape of the AAA from scan K6 does not represent natural AAA disease progression; it instead more closely represents a post-EVAR geometry. The focus of this study is pre-EVAR AAAs and K6 is therefore fully discounted.



Figure 8. A 3-D view overlaid on a respective CT scan coronal plane for scan E1. A thoracic aneurysm is present, but no AAA is present. The focus of this study is AAAs, so the scans are discounted.

2.2.2 Segmentation

The software interface allows for viewing of up to 3 voxel domain windows and a 3-D rendering window. The voxel domains, or slices, can be viewed from the sagittal, coronal, and transverse planes expectedly. Each voxel represents a finite volume with a single intensity value based on the HU (Hounsfield Unit) scale, a measure of tissue density. A brief summary of some core tools of the biomedical imaging software package is covered first. The application of these tools is then described in some detail to produce specific voxel domains, more commonly referred to as masks, representative of desired anatomical structures through a process known as segmentation.

Thresholding refers to setting an upper and lower bound based on voxel intensity values, in this case representative of tissue density, and separating voxels within the bounds from voxels

outside the bounds to binarize a subset of the data. Essentially a range is identified on the tissue density histogram associated with the sum of all the voxels, of which many preset ranges exist, to develop a mask. *Cropping* is a standard operation for any type of image processing in which new borders are defined within an image and segments of the image outside these bounds are removed. In this biomedical imaging application it works no differently, save for the operation is performed in 3-D to voxels instead of 2-D to pixels. *Region Growing* is a unique operation which can greatly increase overall processing speed by examining the 2-D or 3-D connectivity of voxels. A single voxel is selected as a source and only voxels connected by the specified dimension of connectivity which are already within the mask remain within the mask while all others are removed. This can serve to eliminate disconnected voxels from a mask acting as background noise as well as more advanced applications. *Morphologic Operations* define a set of advanced tools that utilize generated masks created through other means. An existing mask can be dilated, eroded, opened, or closed in three dimensions automatically by a set voxel value. For example, a voxel cube with dimensions $3 \times 4 \times 5$ dilated by 1 voxel would become a voxel cube with dimensions $5 \times 6 \times 7$. Additionally this tool can limit operations to only occur within a specified mask, effectively applying user-specified bounding constraints.

The first step to 2-D mask generation of the arterial lumen & vertebrae is the proper selection of a HU intensity value range, better known as thresholding. When selecting the threshold limits it is important to consider the fact that any range could be tightened following any future operations if deemed necessary later, but there is no way to widen the range after other operations. The arterial lumen contains a contrast agent which renders it easily identifiable for a select threshold for each scan, usually > 226 HU. Applying a threshold selects every pixel

matching the criteria and assigned them to a mask. The threshold range for the vertebrae, on the other hand, is not always straightforward to assign. It is well known that bone density differences exist between individuals for a variety of reasons such as age, sex, nutritional intake, and lifestyle. The threshold for the vertebral region of interest therefore has to be adjusted from a base range of > 226 HU on a scan-by-scan basis. There is additionally a fill holes option for thresholding that is used to fill empty voxels within the region of interest. The goal of processing the data within Mimics was to export surface information, which would have been erroneous with internal surfaces caused by holes within regions of interest.

Upon completion of thresholding a number of tools are used. First and foremost the region of interest is specified by a virtual bounding box and cropped. Connective pixels are then identified *between* regions of interest and virtually severed; for example, the intercostal arteries of the aorta are virtually severed from the spine. This process is done with manual editing tools in both 2-D and 3-D, which are time-intensive user-based subjective operations. Upon successfully severing connective pixels the region growing tool can be used on the region of interest to remove background artifacts. Employing this process for the vertebral and luminal regions results in two masks which represent the internal anatomical structures. An example of a segmented mask of lumen in a coronal and transverse slice is shown by Figure 9.

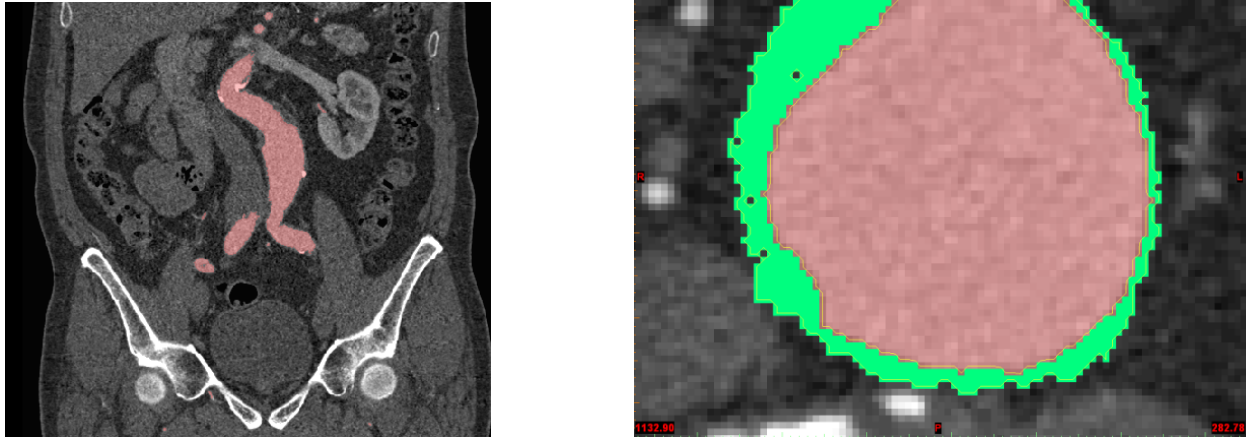


Figure 9. A segmented mask for the arterial lumen (red) and arterial tissue (green) of scan B2 shown for a coronal slice (left) and transverse slice (right). The transverse slice (right) highlights the rectangular nature of voxels which occupy a segmented mask. The arterial tissue is seen to contain a wide region on the upper-left, or left anterior, side indicating the presence of an ILT.

The mask generation for the tissue domain is much different than for the luminal and vertebral domains, and also somewhat depends on the prior generation of each. The vertebral and luminal domains each occupy a distinct region of the tissue density spectrum of the entire image. The arterial tissue, on the other hand, shares a widely populated region of the tissue density spectrum with other soft and/or muscular tissues. Intuitively, however, it is known that the tissue domain exists immediately adjacent to the luminal domain. Thus a working domain can be defined based on the tissue density and the tissue thickness at its thickest point through morphology operations. These operations are based on the existing luminal model and discussion with Mimics® representatives reinforced the advantages of this method as it is repeatable and reliable.

The preset thresholding range for the arterial tissue was > -25 HU. The region of interest was then further defined by a cropping operation. The current tissue mask thus contains

vertebral and luminal voxels. The vertebral mask was subtracted from the tissue mask via a Boolean operation to quickly and efficiently remove voxels pre-defined as vertebral voxels. The tissue mask now contains luminal voxels as well as other voxels > -25 HU. A new mask containing the resulting voxels from dilating the luminal mask by a user-defined number of voxels is created. This user-defined number represents the maximum thickness between the luminal domain and the tissue domain bounds. This new mask will serve to automatically limit the resulting voxels to those already existent within the arterial tissue mask. The arterial tissue mask was thus discarded as the controlled dilation mask replaced it. This process was attempted repeatedly to find an ideal dilation value which minimized the inclusion of excess voxels. Connective pixels were then identified between regions of interest and virtually severed. This process was done with manual editing tools in both 2-D and 3-D, which are time-intensive user-based subjective operations. For the arterial tissue this process was much more prone to operator bias. CT scans do not offer excellent soft tissue differentiation, and often boundaries were approximated as best as possible. A final region growing operation successfully removed any remaining disconnected voxels.

2.2.3 3-D Modeling

Completed 2-D masks represent voxel domains, where every voxel is a 3-D rectangle. The direct 3-D interpretation of a mask would therefore appear as the sum of many connected rectangular volumes, which would feature a very rough and noisy surface. The masks are modeled in 3-D through pre-defined and/or custom methods to produce surfaces in Standard Tessellation Language (STL) format instead, which describes an unstructured surface by the unit normal and vertices of triangles in 3-D Cartesian coordinates. The STL quality is still dependent

upon the voxel resolution, however, which differs between every scan. A generated STL model highlighting the surface structure is shown by Figure 10.

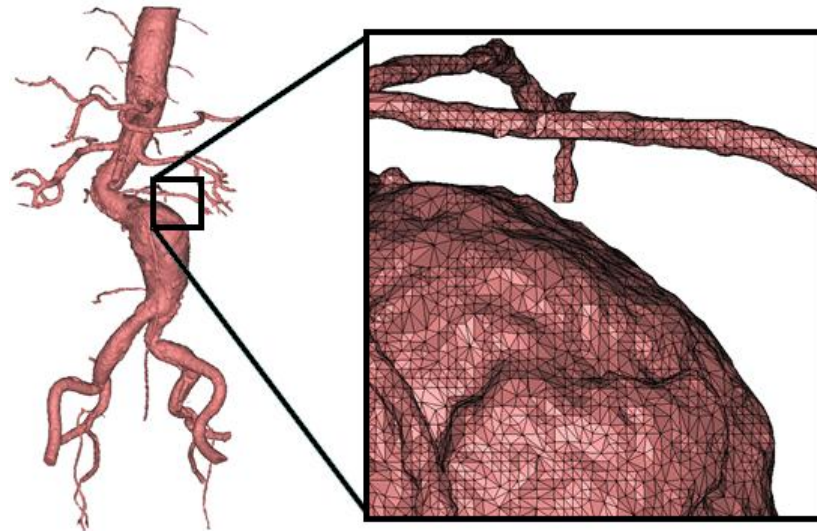


Figure 10. A 3-D AAA lumen STL reconstructed from scan B2. STL format describes a triangularly meshed surface, as can be clearly seen. The data exported from the 3-D models for Chapters 3 & 4 uses point cloud format. This format will only contain the vertex information from STL models.

A wide variety of options exist for generating and refining an STL model from a mask, thus STL generation from masks was standardized according to the a set of parameters (Table 3). Given that the voxel resolution and therefore the STL resolution is not standardized no standardized smoothing or wrapping criteria could be clearly established past the initial STL model generation. Laplacian smoothing was applied via a subjective number of iterations from 0 - 10 to each STL at a constant smoothing factor of 0.7 (Table 4). The goal of smoothing is to reduce surface irregularities, spikes, and noise with qualitative visual inspection as the means to gage the reduction.

Table 3. Optimal STL model generation parameters used for every STL model generated in the study. Contour interpolation results in a smoother model with less gaps and is recommended for medical CT applications [59]. Matrix Reduction is set to 1, equivalent to no matrix reduction, which inherently nullifies the need to select a matrix reduction algorithm as well (not shown).

Interpolation	Contour instead of Gray Value
Smoothing	Iterations: 2
	Smooth factor: 0.3
Triangle Reduction	Reducing mode: Advanced Edge
	Tolerance: Automatic (mm)
	Edge angle: 10 degrees
	Iterations: 3

Table 4. The number of employed smoothing iterations at a constant smoothing factor of 0.7 on each STL model after optimal model generation. The smoothing was limited to a maximum of 10 iterations to avoid significant loss of detail.

Smooth Iterations			Smooth Iterations			Smooth Iterations		
Scan	Tissue	Lumen	Scan	Tissue	Lumen	Scan	Tissue	Lumen
A1	10	6	G1		3	I1		4
A2	8	5	G2		3	I2		4
B1	10	8	G3		3	I3		4
B2	10	6	G4		3	I4		5
B3	10	5	G5		8	I5		5
C1	8	4	G6		3	I6		5
C2	9	5	H1	6	4	J1	8	3
D1		3	H2		4	J2	8	4
D2		7	H3		8	J3	10	4
D3		10	H4		6	J4	10	4
F2		4	H5		6	J5	10	4
F3		7	H6		8	K1	10	4
F4		7	H7		6	K2		4
F5		9				K3		5
F6		10				K4		5
F7		10				K5		4

For each scan surface models for the arterial lumen, arterial tissue, and adjacent vertebrae are generated, then smoothed as judged necessary. The 3-D STL models can then be registered. Registration refers to translating, rotating, and scaling a data set to a common position with a reference data set. Within the software three relevant modes of registration exist. *Image Registration* requires landmark point pairs to be identified in a reference image and secondary image. The landmark points can be identified in the sagittal plane, coronal plane, and transverse plane. The 4×4 transformation matrix that best relates the sets of landmark points is then automatically calculated and applied to the secondary image. *Point Registration* requires landmark point pairs to be identified in a reference position and desired position. The landmark points can be identified in the sagittal plane, coronal plane, transverse plane, and in 3-D. The 4×4 transformation matrix that best fits the set of landmark points is then automatically calculated and applied to the selected STL. *Global Registration* simply requires the identification of a fixed reference STL and a moveable STL. The distance field between the STLs is then automatically minimized over the course of a user-defined number of iterations. Each iteration of global registration calculates a 4×4 transformation matrix that further reduces the distance field and automatically applies it. Global registration is chosen for its high accuracy, ease of use, repeatability, and objectivity.

Global registration is an iterative process based on minimizing the distance field between STLs. The sum of all of a patient's scans are first imported to a common Mimics workspace, for example scans A1 & A2 of patient A. The existing STLs for a given scan are then linked such that transformation of one model would affect the linked models identically, but minimization of the distance field is unaffected by the linked models. In essence this means the distance field is

minimized between two models, and the resulting transformation matrix is applied to any additional desired models. A fixed reference vertebral STL and a second moveable vertebral STL are chosen then the moveable vertebral STL is manually translated and rotated to be in as identical a position as possible to the reference vertebral STL by eye. The two vertebral models are selected and global registration is applied for 1000 iterations to register the moveable set of STLs according to the transformation matrix describing the minimum distance field. This process was very quick (<1 minute) and was repeated for all STLs from a patient on a common reference vertebral STL.

The resulting STLs of a patient include the vertebral STL from each scan aligned with vertebral STL of the first scan, and all associated lumen and tissue models positioned automatically based on this alignment. This registration method allows for the unique visualization of the true spatial differences of the AAA geometry and offers insight into the surface evolution of an AAA.

2.3 Results

Lumen models were generated for 45 scans, and tissue models were generated for 14 scans. Figures 11 and 12 represent lumen STL models from each patient from the front coronal plane and right sagittal plane views, respectively. These models include the renal arteries, iliac arteries, sometimes the mesenteric arteries, and occasionally the celiac trunk. The region of interest for Chapter 3 onwards is the infrarenal aorta, and only the infrarenal region is generated for all 45 scans as shown by Figure 13.

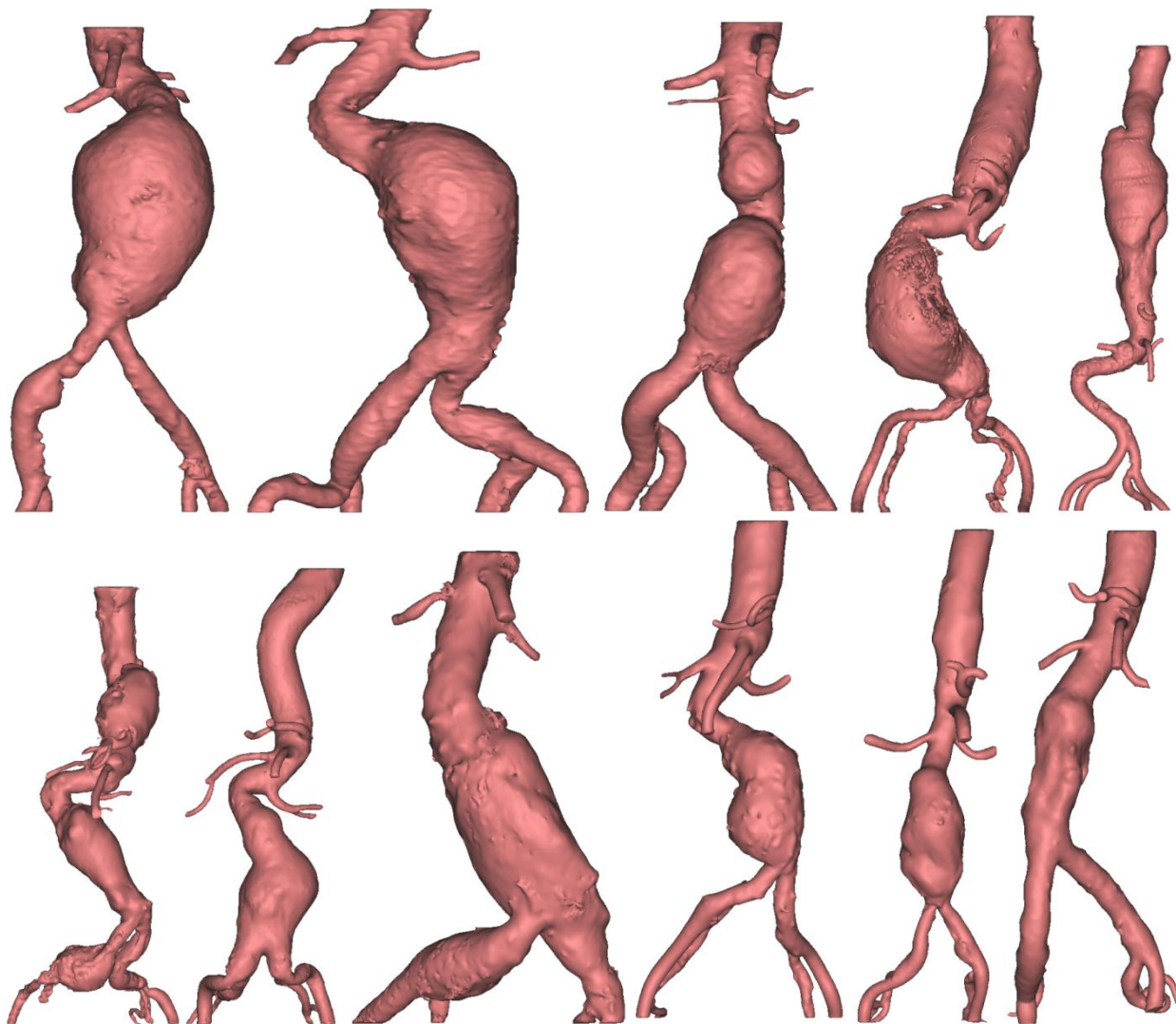


Figure 11. Front coronal plane view of 3-D luminal STL models generated for all 11 patients. From top-left to bottom-right in reading order the STLs originate from scans: A2, B3, C2, D3, E2, F7, G6, H7, I6, J6, K5.

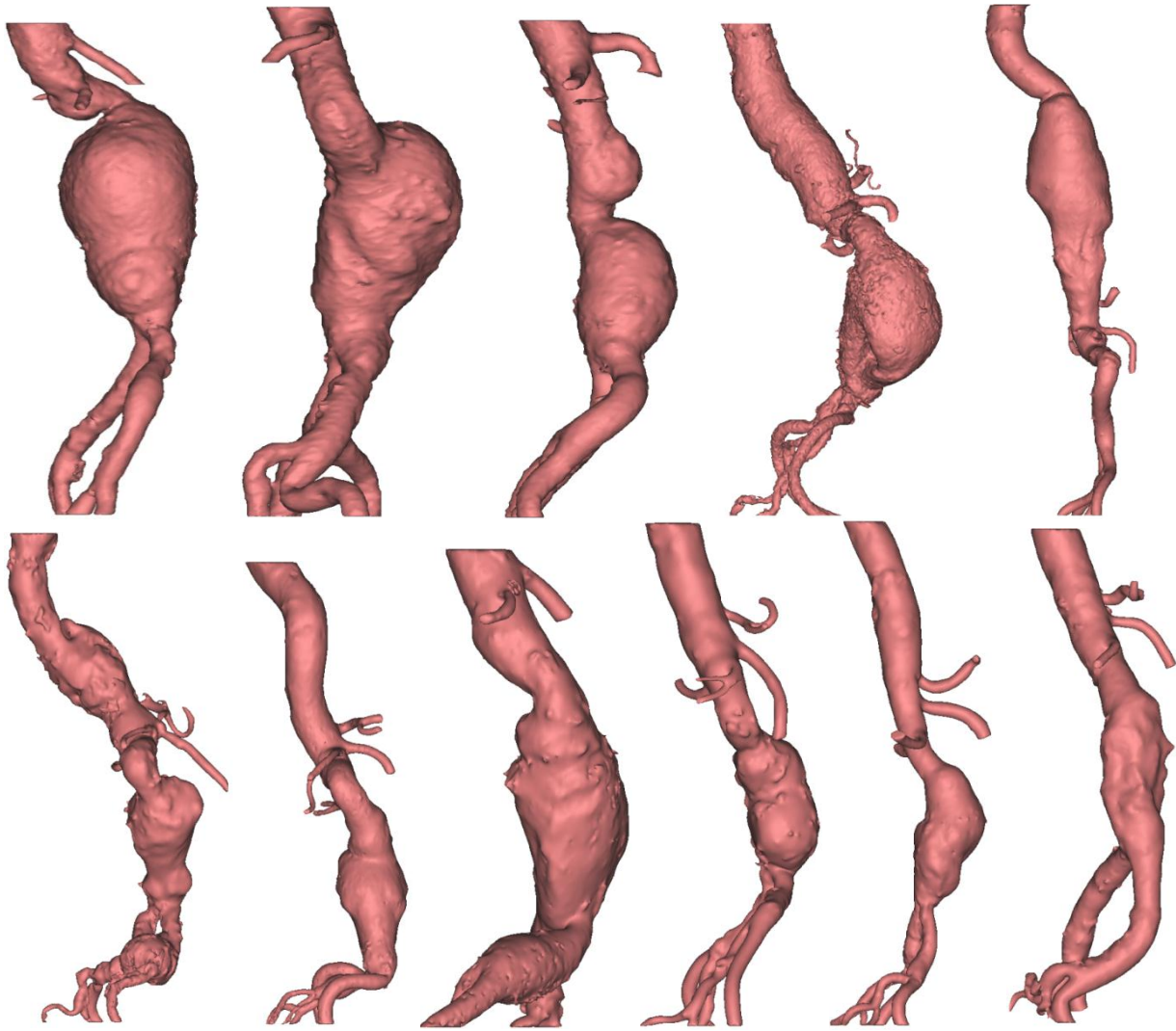


Figure 12. Right sagittal plane view of 3-D luminal STL models generated for all 11 patients. From top-left to bottom-right in reading order the STLs originate from scans: A2, B3, C2, D3, E2, F7, G6, H7, I6, J6, K5.

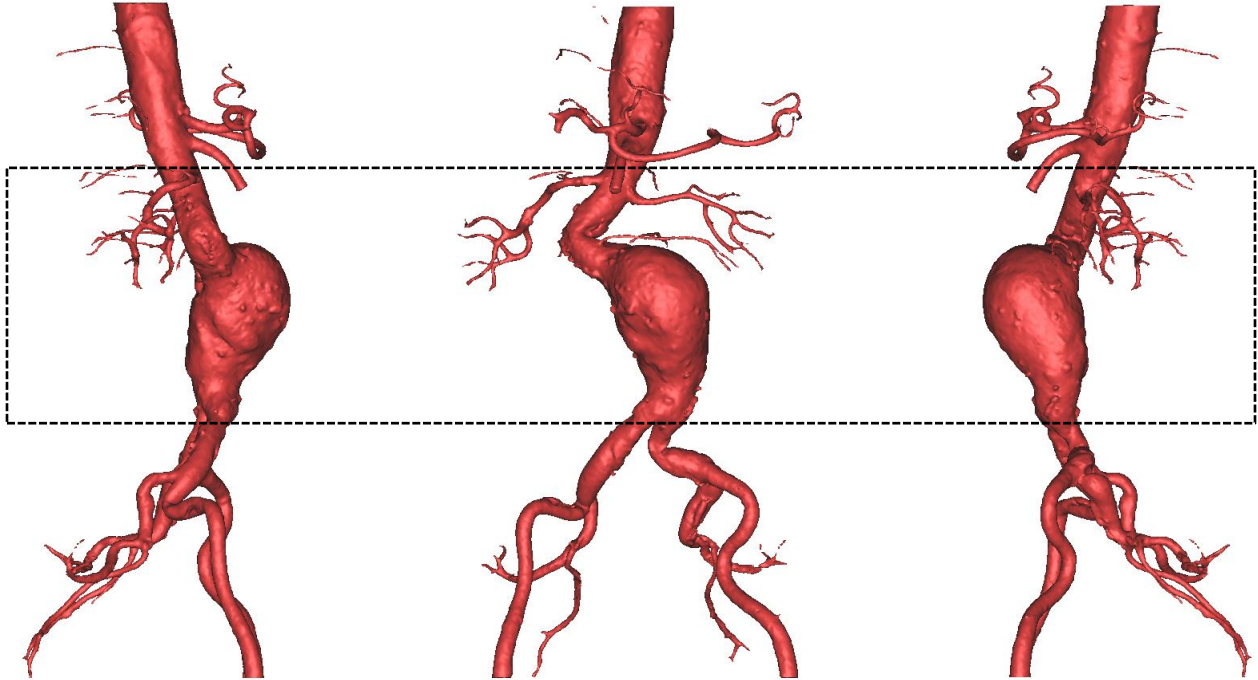


Figure 13. A 3-D STL model of a reconstructed infrarenal AAA luminal surface as seen from the left sagittal plane (left), front coronal plane (center), and right sagittal plane (right). A bounding box indicates the infrarenal region specifically to be exported to a technical computing software package.

An example of two registered vertebral models from scans I1 & I3 is shown (Figure 14).

It is clear that the models positions match extremely closely given that they are independently generated from different CT scans.

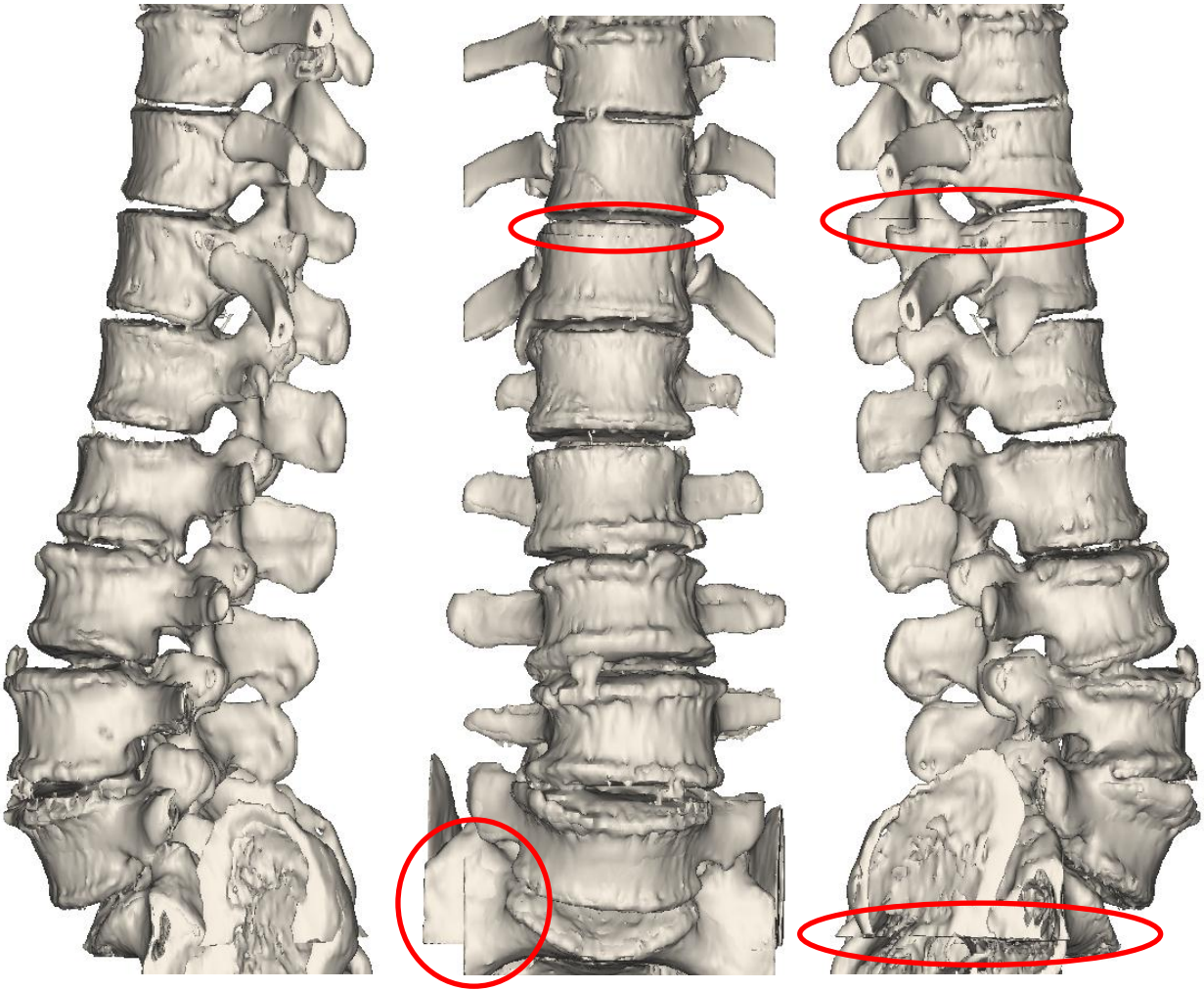


Figure 14. An example of two registered vertebral models from scans I1 & I3 as viewed from the left (left), front (center), and right (right). Each model is the same color, and has been registered to match the position of its pair. Near the top and bottom of the models clipping can sometimes be observed, which highlights the boundaries of a model (red). In general, however, it is clear that the models' positions match extremely closely given that they are independently generated from different CT scans. The associated lumen and tissue models are also automatically registered (not shown) according to the transformation matrix generated by minimizing the distance field between vertebral models.

Tissue models are very time consuming to produce, and as such they are only produced in the infrarenal aorta with the absence of any branches. Tissue models were generated for 14 of 45 scans based first on the order the data was received and second on the number of scans available per patient. Eventually all of the data will be processed. Tissue models underwent the same registration process concurrently as the lumen as shown by Figure 15. Additionally the arterial wall thickness can be visualized through the transparent overlay of a respective lumen and tissue model as shown by Figure 16.

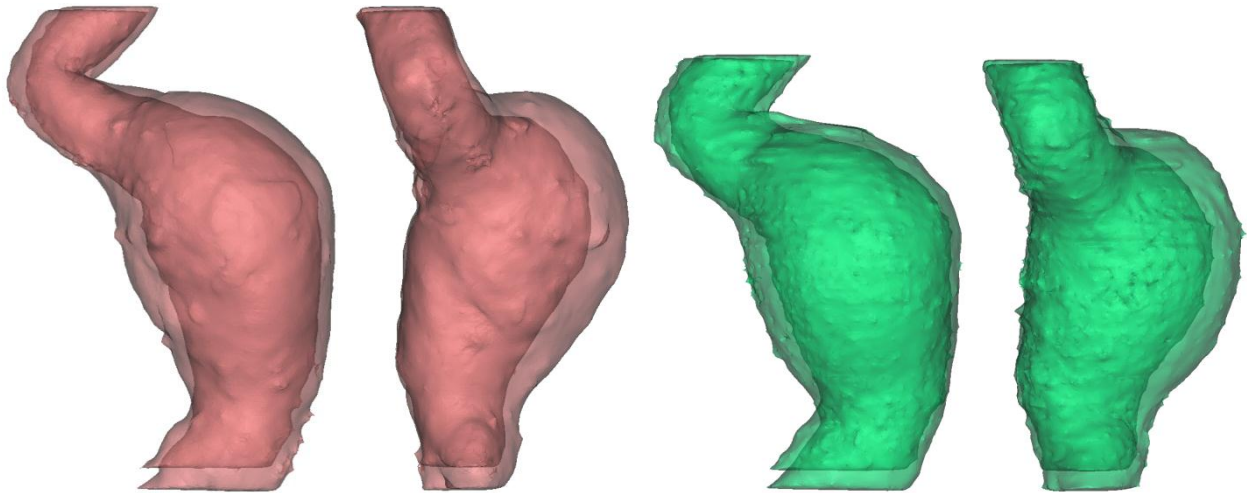


Figure 15. Transparent and registered front coronal plane view (left) and right sagittal plane view (second from left) of 3-D luminal STL models for B1 and B3. Transparent and registered front coronal plane view (second from right) and right sagittal plane view (right) of 3-D tissue STL models for B1 and B3. The lumen and tissue models presented are not to scale, as the lumen models are inherently always smaller than the tissue models.

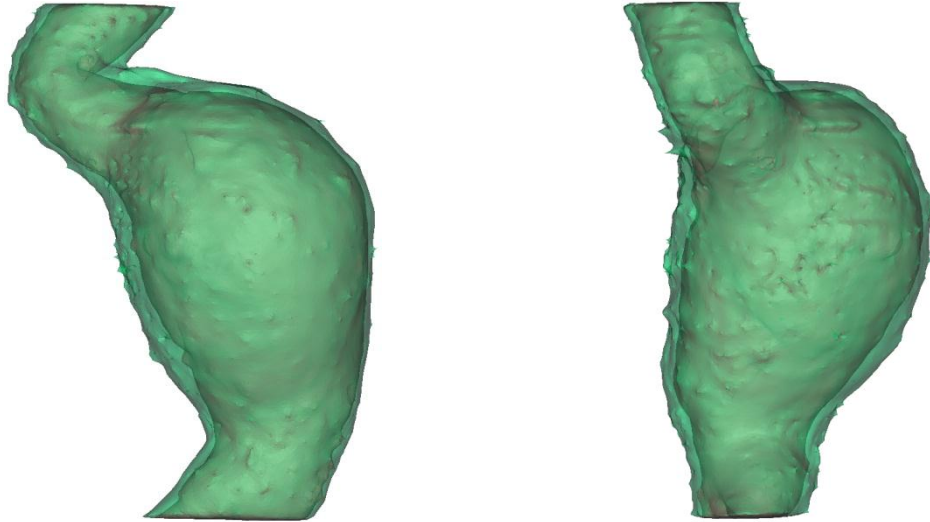


Figure 16. Transparent and registered front coronal plane view (left) and right sagittal plane view (right) of 3-D luminal and tissue STL models for B3.

Regions of significant vertebral interaction with the vessels were identified for some cases. The region with significant vertebral interaction displays flattening of vessel curvature in the cross-sectional view (Figures 17 and 18). The vertebral surface can feature ossifications originating and projecting from the spine known as osteophytes. The presence of osteophytes on the spine increases the complexity of the relationship between an AAA and the spine, but not the nature of the relationship; osteophytes serve as a growth barrier and have an influence on vessel flattening (Figures 17 and 18). The prevalence and variability of osteophyte growth on the spine is patient-specific and must be considered on a case-by-case basis.

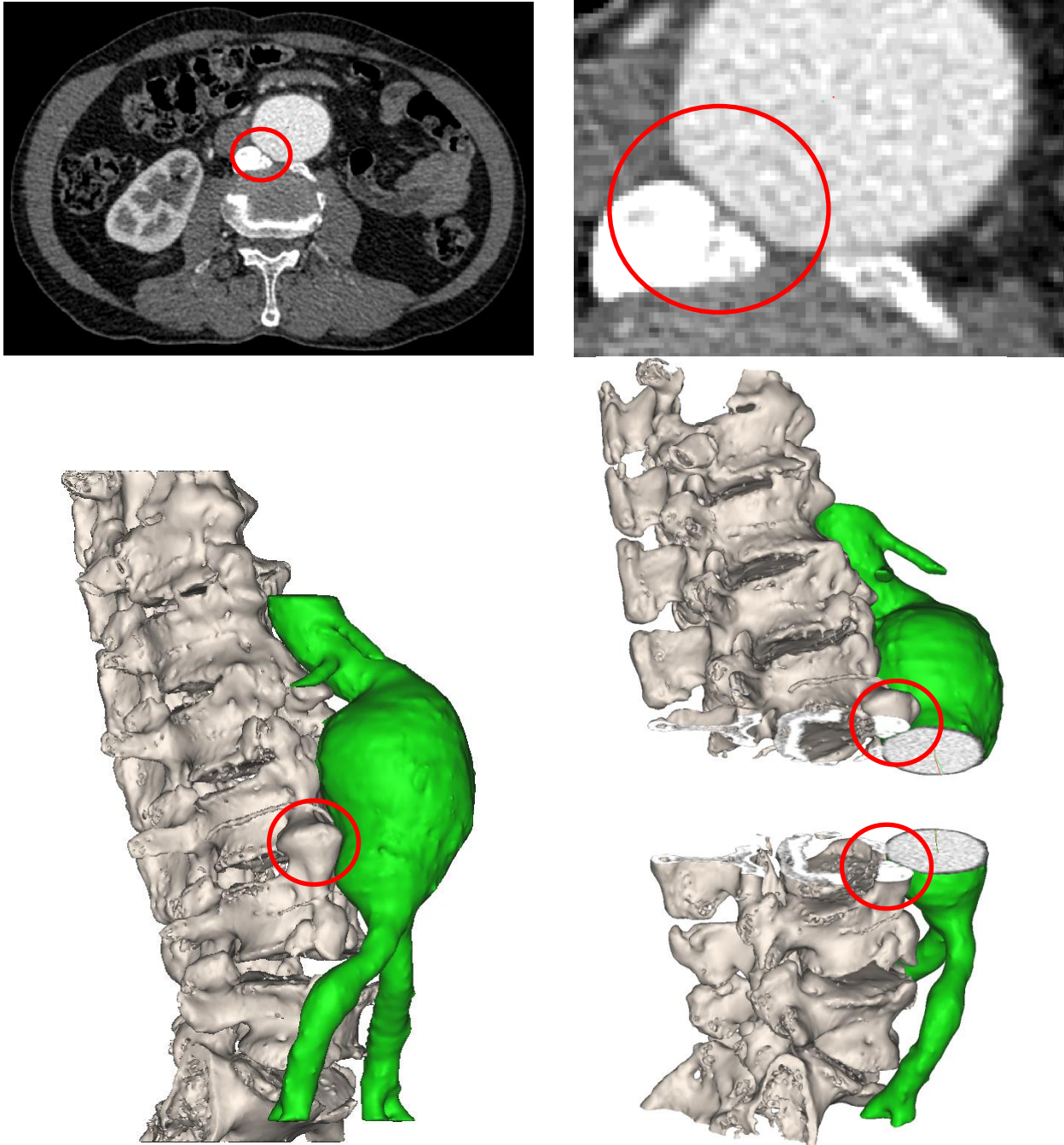


Figure 17. A transverse slice un-zoomed (upper-left) and zoomed (upper-right) from scan A2. A 3-D reconstruction of the AAA tissue geometry for scan A2 from the right (bottom-left) and an opened version of the AAA tissue geometry for scan A2 from the right (bottom-right). Red circles indicate linked areas between images. Within the red circles it is clear that the AAA tissue is interacting with the spine and that the local geometry of the tissue is affected.

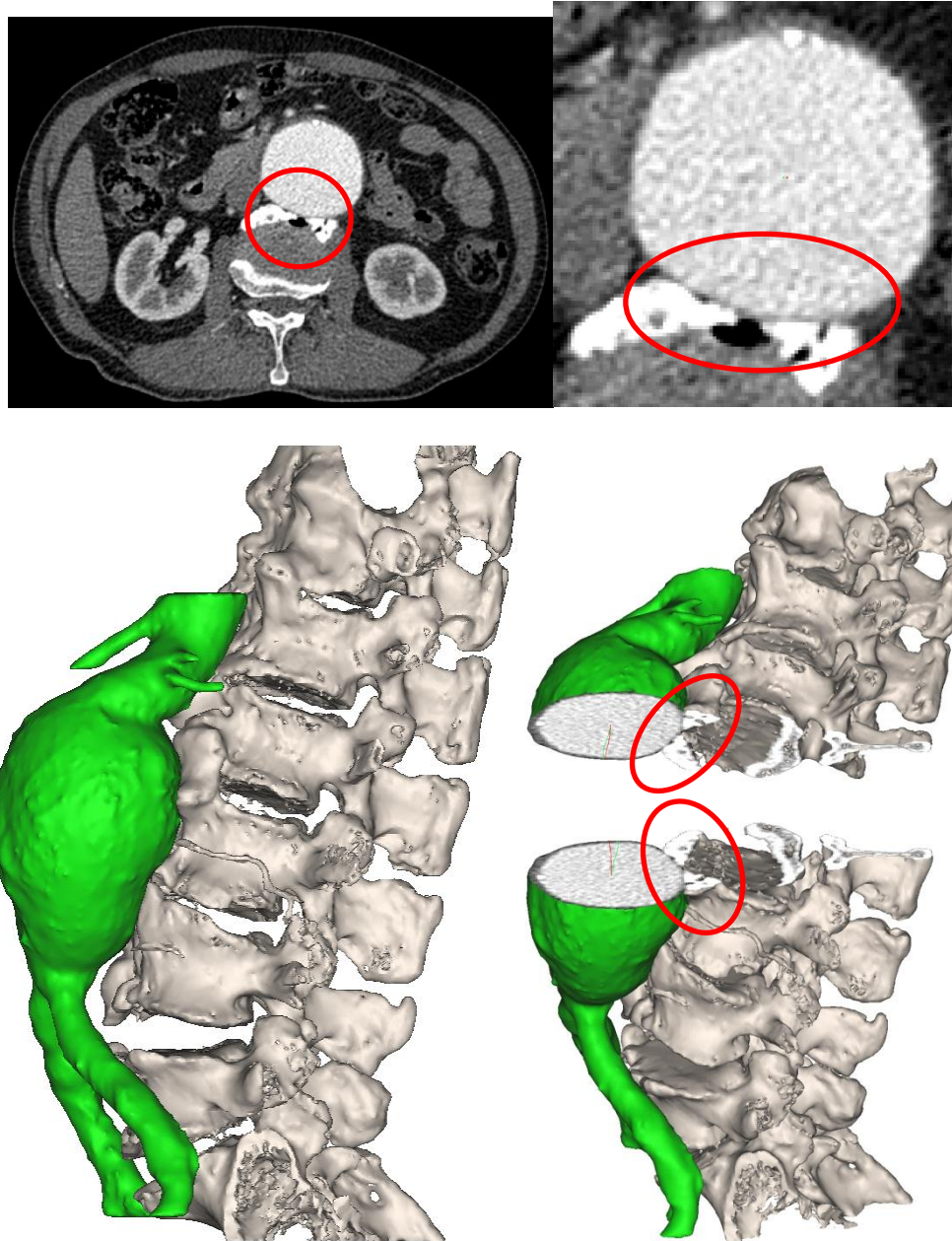


Figure 18. A transverse slice un-zoomed (upper-left) and zoomed (upper-right) from scan A2. A 3-D reconstruction of the AAA tissue geometry for scan A2 from the left (bottom-left) and an opened version of the AAA tissue geometry for scan A2 from the left (bottom-right). Red circles indicate linked areas between images. Within the red circles it is clear that the AAA tissue is interacting with the spine and that the local geometry of the tissue is affected.

The inferior vena cava was modeled for scan B2 to visualize its interactions with an AAA (Figure 19). The shape of the aorta deviated from standard anatomical positions below the left renal vein and we speculate that the left renal vein can serve as an anchor to the infrarenal during

the aneurysm progression. It may also be possible that the physical constraint of the left renal vein over the vessel and the tethering of the renal arteries provide a strong confinement, or an anchor at the region of the aorta, below which the aorta gradually bends as the lesion progresses.

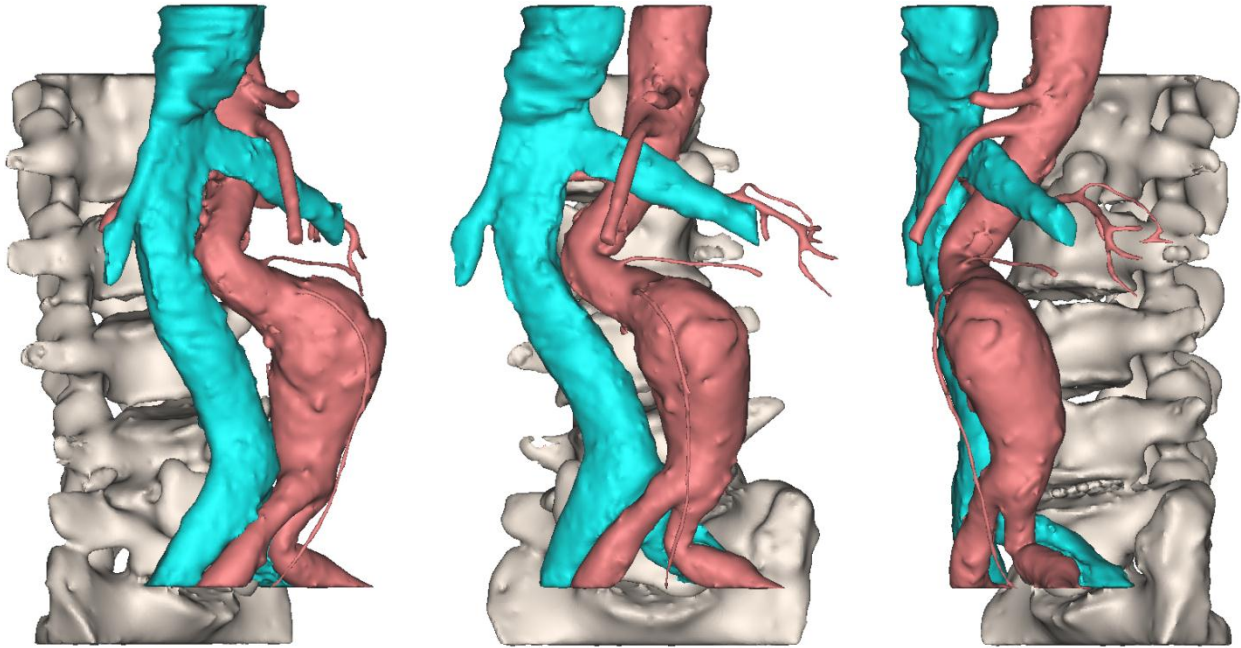


Figure 19. Reconstructed 3-D models for the vertebrae (white), AAA lumen (red), and inferior vena cava tissue/lumen (blue) as seen from the left (left), front (center), and right (right) for scan B2.

2.4 Discussion

The 3D models generated from the biomedical software are relatively good, but there is some degree of error inherent to segmentation and modeling. The resolution is approximately 0.7 mm per pixel, which is high for CT images, but some detail can still be lost in areas of thin tissue, such as arterial tissue compressed against the spine (Table A.1). CT scans are also not instantaneously obtained for the whole region. For this collection the entire torso was scanned, usually within 10 seconds. The resulting CT scan is therefore taken to be an average of the geometry *in vivo*, which is important to consider when observing the aorta given it is constantly undergoing cyclic deformation by means of the cardiac cycle.

It is shown from the results of Figures 11 and 12 that the reconstructed models represent AAA geometries accurately. Although smoothing was applied subjectively, the surface finish of each model appears to have similar quality. Showing all results for 45 lumen models, 45 vertebral models, and 14 tissue models is not practical and, hence, a subset of images was chosen per patient to be representative. As the infrarenal aorta begins at the renal branches it is clear for each case that the vessel is at some angle from the z-axis. Patients C and J do not support this trend as strongly, but upon examination it is clear that all vessels present some degree of tortuosity. This tortuosity is three-dimensional, as the same trend can be observed in the coronal and sagittal planes. A significant presence of an ILT is also likely to be a factor affecting the tortuosity.

The majority of AAAs contain an ILT layer, though the thickness and circumferential position of the ILT varies significantly between patients. For example patient J presents a relatively small predominantly anterior ILT while patient D presents a relatively large predominantly left lateral ILT. There is no uncontested cause and effect relationship between patient specific AAA geometries / hemodynamics and ILT formation sites. Regardless of the factors influencing ILT growth sites, the presence or absence of an ILT affects the biomechanical relationship between the AAA and surrounding tissues; the spine serves as a rigid growth barrier to AAA expansion, and if ILT is present in the circumferential region in contact with the spine then disease progression is affected [44–46]. Arterial tissue and ILT carry different mechanical properties, which directly leads to different interface mechanics when considering vertebral / vessel interaction. It is observed from Figures 17 and 18 that extended areas of contact between tissue and vertebrae present marked vessel flattening within the cross section. This vessel

flattening was observed both in the case of vessel contact with normal vertebral tissue and vessel contact with vertebral ossifications. The inferior vena cava is adjacent to the abdominal aorta and may interact with an AAA. For the lesion shown in Figure 19, however, no clear morphological features representing interaction between an AAA and the inferior vena cava are observed, although the idea of the left renal vein serving to anchor an AAA in place is clear when visualized.

From these observations it is hypothesized that the observed change of the centerline, eccentricity and asymmetry of the vessel, and the curvature of the vessel cross section polylines are morphological features representing the effects of surrounding tissue.

CHAPTER 3. Morphological Features Influenced by Surrounding Tissue

3.1 Introduction

The pathology of AAA is such that enlargement of the aorta is associated with disease progression. The simplest measure of aortic enlargement is maximum diameter. Aneurysms less than 5 cm to 5.5 cm in diameter are considered small and aneurysms over 5 cm to 5.5 cm are considered large. Surgical treatment is usually only recommended for large aneurysms unless patient-specific concerns warrant otherwise. As covered in Chapter 2, US is the usual imaging modality used for screening and monitoring of small AAAs, while CT is used when intervention is deemed necessary. Regardless of imaging modality, values of the maximum diameter can be extracted according to four criteria: plane of acquisition, axis of measurement, caliper placement, and diameter selection [51]. Critical reviews of the clinical obtainment of AAA maximum diameters are offered by Long et al., Ferket et al., and Powell et al. from which much of this review is derived [51–53]. The plane of acquisition, axis of measurement, and caliper placement variability between studies is described.

The plane of acquisition refers to whether the maximum diameter is obtained from the anatomical (absolute) reference planes or the aortic (relative) planes. The anatomical reference planes are the sagittal, coronal, and transverse planes. The aortic reference planes are normal to the arterial centerline, such that the (x, y, z) coordinate basis differs as the centerline is traversed, especially for tortuous vessels; a plane normal to the centerline is known as a longitudinal plane. US can be aligned with either reference by a skilled operator, while CT scanning is automatically

aligned to the transverse plane as the native plane. CT MPR usually generates the additional anatomical planes, the sagittal and coronal planes, but other MPR algorithms exist to generate planes for the aortic reference. Non-standard MPR algorithms for CT scans inherently suffer from a loss of resolution however, as the scanning algorithm cannot be adjusted from the anatomical standard planes to match unique MPR algorithms. MRI scanning has the unique advantage of being able to take measurements in any plane, and additional MPR algorithms exist to take advantage of this.

The axis of measurement refers to the chosen axis within to the cross-sectional plane of measurement for maximum AAA diameter. The anteroposterior and transverse axes refer to the sagittal and transverse axes respectively. The transverse cross-sectional view allows for simultaneous multi-axis measurement while the sagittal and coronal views only allow for a single axis of measurement. For US measurements are performed during scanning, while CT MPR offers delayed analysis where any axes can be used for measurement.

After identifying the acquisition plane and axis of measurement the caliper positioning must be defined. The caliper positioning refers to which surface of the AAA wall to bound the maximum diameter measurement to whether with calipers for an US or digital measurements for a CT reconstruction. The positioning can be internal, external, leading edge to leading edge, and outer anterior to inner posterior. A total of 56 studies were critically reviewed by Long et al., Ferket et al., and Powell et al. to identify the choices of plane of acquisition, axis of measurement, and positioning of the calipers defined by different clinical groups [51–53]. The results of their studies are summarized in Table 5.

Table 5. Summary of the definition of techniques employed over the survey of 56 studies by approximate percentage [51–53]. Some groups reported multiple methods of measurement to be in use rather than a single method, resulting in total percentages not equal to 100%.

Plane of Acquisition	
Not Specified	51%
Longitudinal	34%
Transverse	30%
Axis of Measurement	
Anteroposterior	63%
Not Specified	37%
Transverse	30%
Positioning of the Calipers	
Not Specified	61%
External	27%
Internal	4%
Leading edge to leading edge	2%
Outer anterior to inner posterior	4%

These results clearly show that no undisputed standard methodology can be extracted from the literature to determine maximum AAA diameter. An axis of measurement (anteroposterior) was the only variable that was more often specified than not.

3.2 Method

From reviewing the literature it is clear that no standardized method of diameter measurement exists. In general 4 steps are identified and followed, however. The plane of acquisition is specified, the measurement axis is specified, the caliper positioning is specified, and the final maximum diameter is obtained as either a maximum obtained value or a multi-trial average value. For obtaining maximum diameters from the CT standard MPR of anatomical planes the transverse plane was selected as the plane of acquisition, as 30% of reviewed studies suggest. The longitudinal plane which 34% of studies suggest is subjectively defined or requires

centerline generation to perform relative MPR and attain true longitudinal planes to the centerline. An example transverse measurement plane is shown by Figure 20.

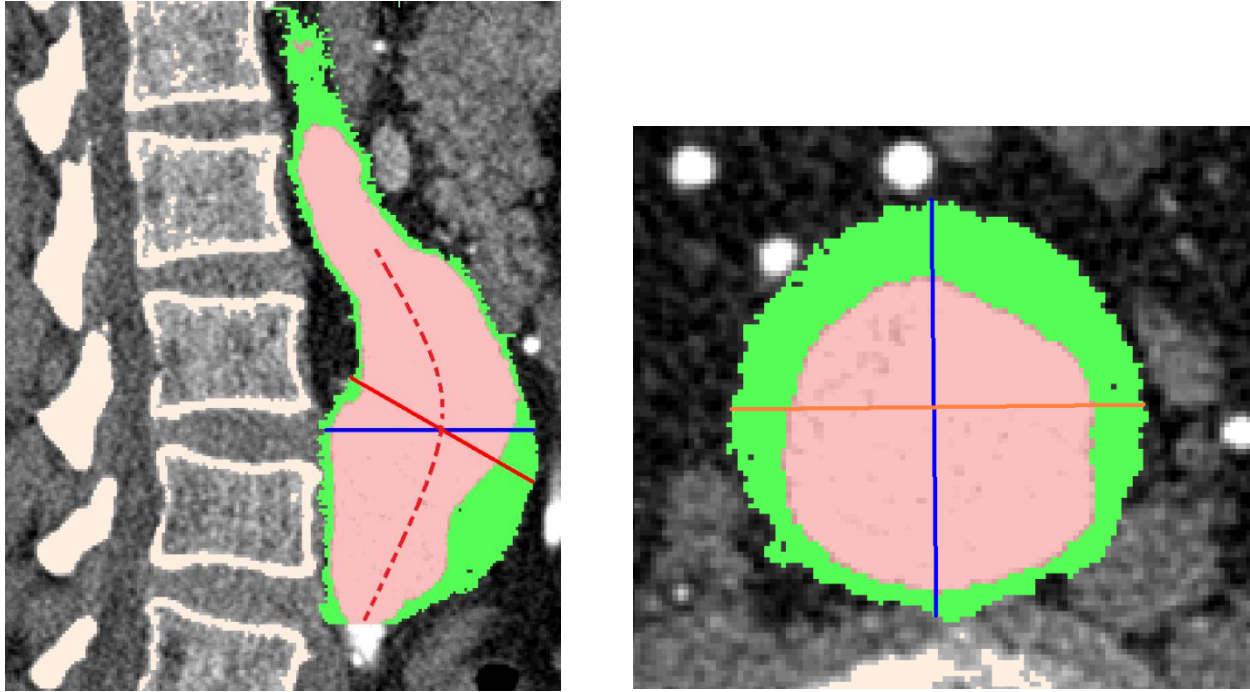


Figure 20. A sagittal slice (left) of scan J5 and a transverse slice (right) of scan J5 with the segmented lumen/tissue (red/green). The blue line indicates an anteroposterior maximum AAA tissue diameter measurement axis in the transverse plane (left, right), the solid red line indicates an anteroposterior maximum AAA tissue diameter measurement in the longitudinal plane (left), the dashed red line indicates a crude longitudinal axis approximation (left), and the orange line is simply the AAA tissue diameter measurement at 90° in the transverse plane to the anteroposterior measurement axis. The caliper positioning for this case was external/tissue.

The measurement axis specified is anteroposterior unless it is clear that the vessel is noticeably asymmetric in which case multiple axes were tested and the axis corresponding to the maximal measurement was chosen. The caliper positioning for obtaining tissue values was external while the caliper positioning for obtaining lumen values was internal. Specifying the axis of measurement for the lumen additionally considers the presence of ILT and its asymmetry. Measuring both the maximum diameter of the lumen/tissue and the diameter on the axis 90° to it within the plane of acquisition allows for a simplistic calculation of eccentricity based on the

diameter ratio. Asymmetric ILT can lead to very different axes of measurement for the maximum AAA lumen diameter as shown by Figure 21.

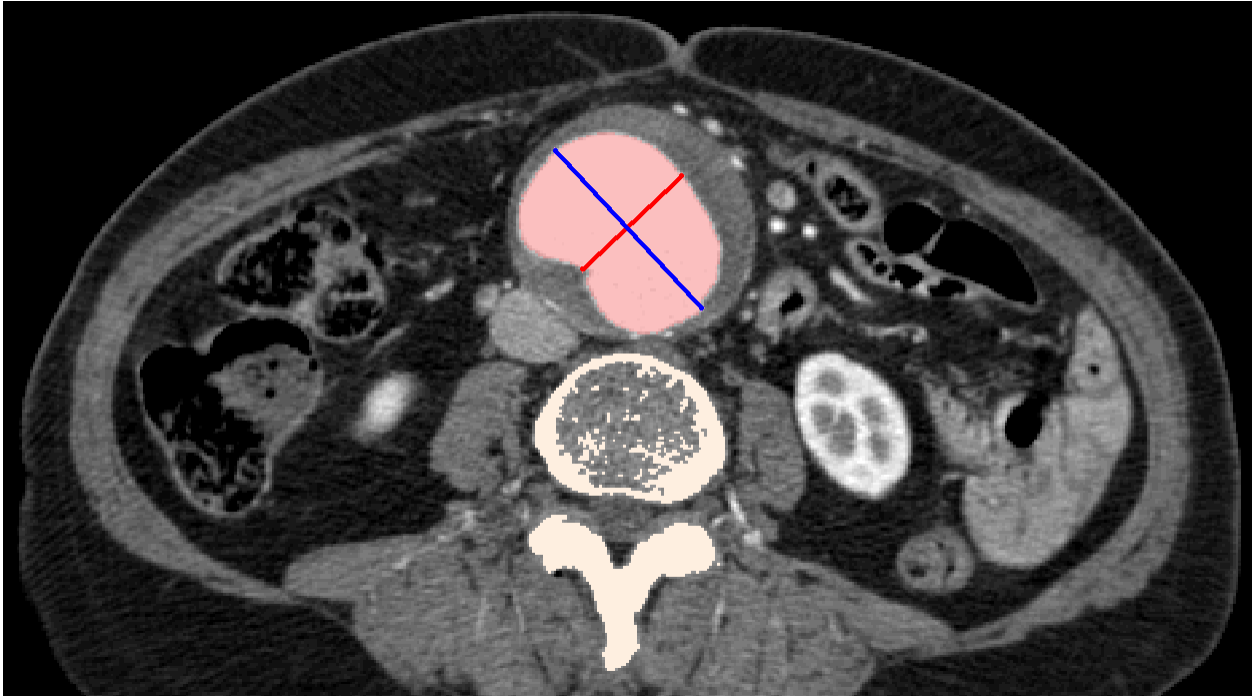


Figure 21. A transverse slice of scan D2 with the segmented lumen (red), maximum internal/lumen diameter axis (blue) and axis 90° to the maximum internal/lumen diameter (red). It is clear that anteroposterior measurements will not yield maximal results in the presence of an eccentric ILT. This is the reason that the maximum diameter axis was used and anteroposterior was not strictly used in all cases.

3.3 Results

Maximum diameter measurements for the lumen and tissue were recorded from anatomical plane CT MPRs for each patient. For patient C two aneurysmal sacs are recorded, the primary is referred to as Patient C, while the secondary is referred to as Patient C (sac) (Figure 22).

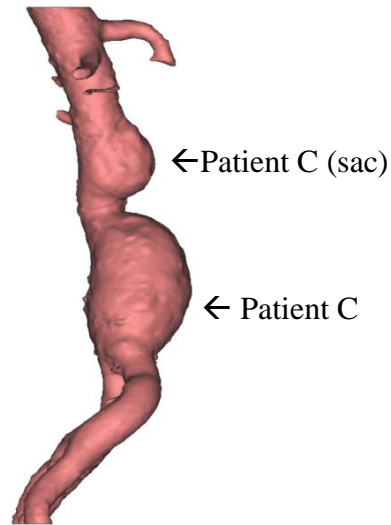


Figure 22. 3D CT reconstruction of patient C as viewed from the right. Two aneurysmal sacs are present and the primary is referred to as Patient C, while the secondary is referred to as Patient C (sac).

The values obtained from measuring the AAA maximum tissue diameter in the transverse plane preferring an anteroposterior measurement axis unless asymmetry is present, with external caliper positioning, and no value averaging are plotted by Figure 23 (Table A.3). The linear approximations of annual expansion rate are calculated by fitting the data linearly and the results are shown by Table 6.

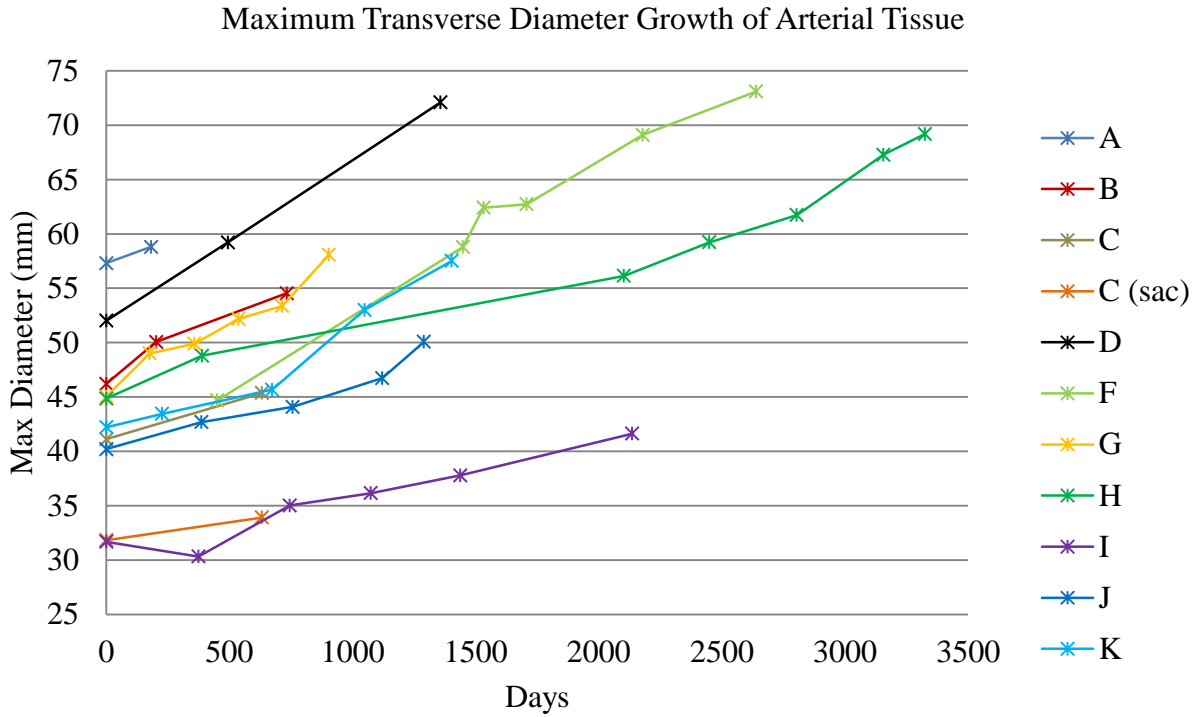


Figure 23. The maximum transverse diameter of the arterial tissue vs. scanning date for each patient.

Table 6. Linear approximation of annual transverse maximum AAA tissue diameter growth and R^2 fit value.

Patient	D_{max}	linear increase (cm / year)	R^2
A		0.3010	1.0000
B		0.3931	0.9569
C		0.2462	1.0000
C (sac)		0.1208	1.0000
D		0.5410	1.0000
F		0.4796	0.9804
G		0.4670	0.9542
H		0.2427	0.9536
I		0.1888	0.9253
J		0.2542	0.9381
K		0.4064	0.9406

The annual expansion rates of the tissue were additionally calculated for successive scans and plotted as shown by Figure 24. A measure of eccentricity of the tissue was taken as shown by Equation 1 and plotted for each scan as shown by Figure 25.

$$Eccentricity = \frac{D_{max}}{D @ 90^\circ \text{ to } D_{max}} \quad (1)$$

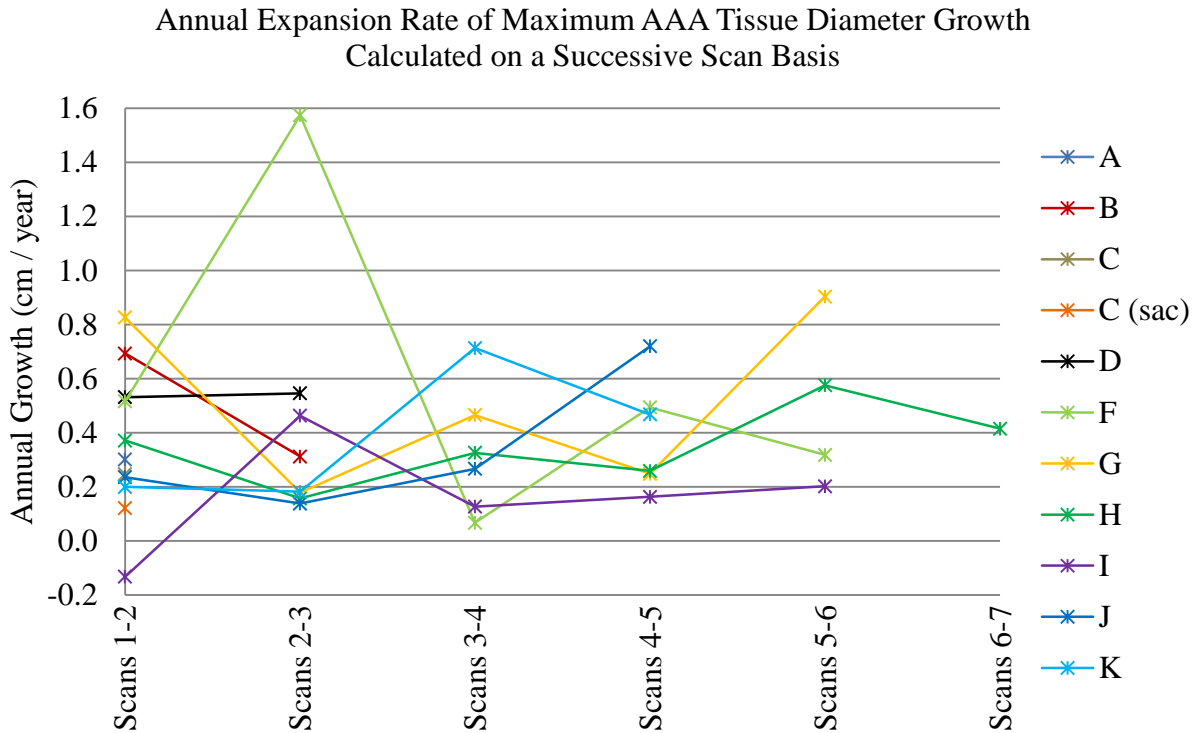


Figure 24. The annual expansion rate of maximum AAA tissue diameter growth calculated on a successive scan basis for each patient.

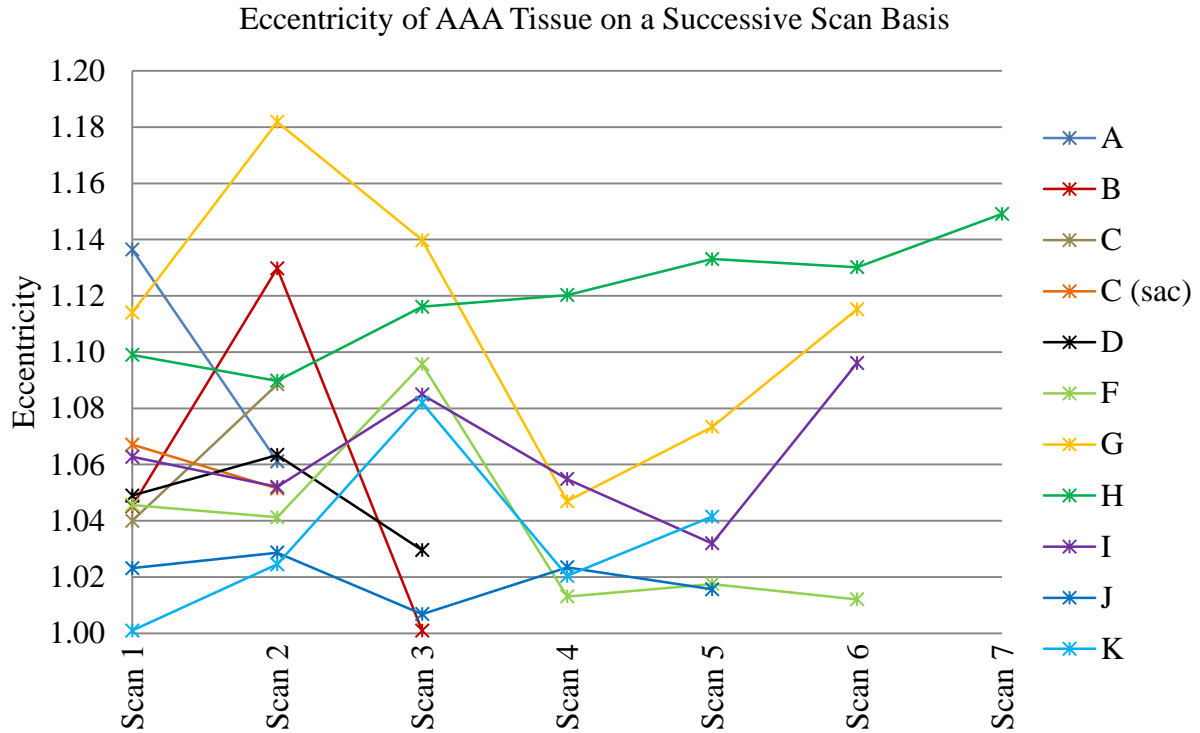


Figure 25. The tissue eccentricity based on $\text{eccentricity} = (D_{\text{max}}) / (D @ 90^\circ \text{ to } D_{\text{max}})$ for each patient scan.

The values obtained from measuring the AAA maximum lumen diameter in the transverse plane preferring an anteroposterior measurement axis unless asymmetry is present, with internal caliper positioning, and no value averaging are plotted by Figure 26 (Table A.4). The linear approximations of annual expansion rate are calculated by fitting the data linearly and the results are shown by Table 7.

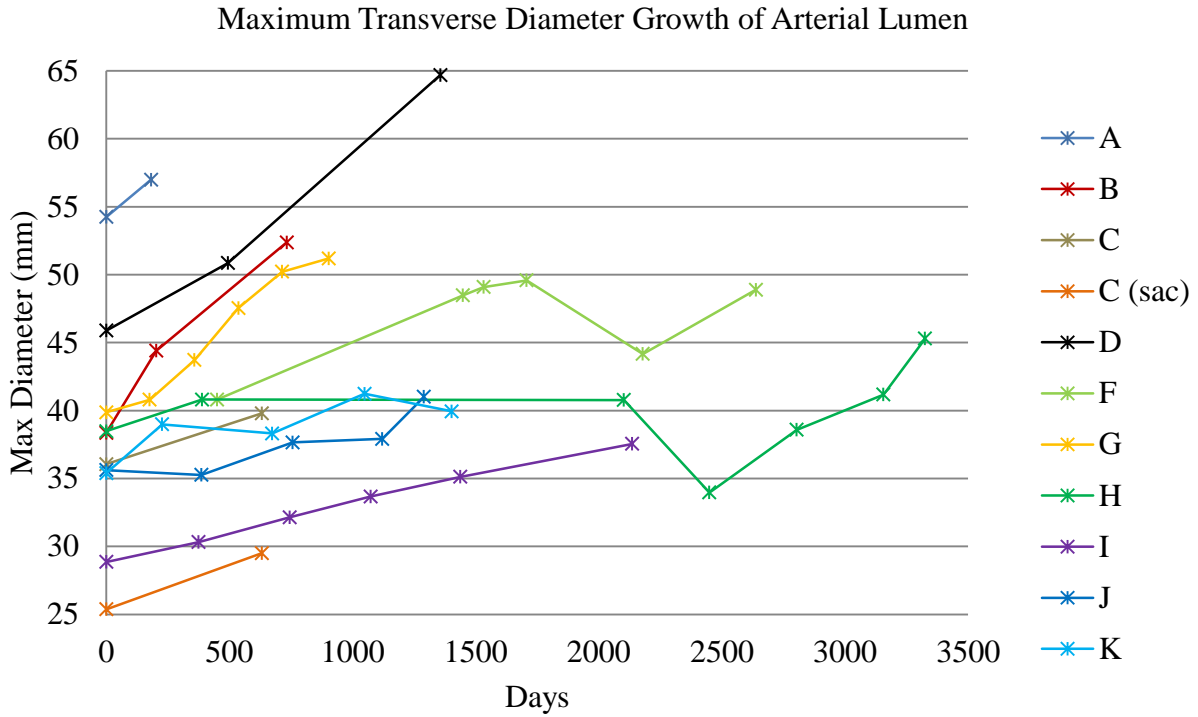


Figure 26. The maximum transverse diameter of the arterial lumen vs. scanning date for each patient.

Table 7. Linear approximation of annual transverse maximum AAA lumen diameter growth and R^2 fit value.

Patient	D_{max}	linear increase (cm / year)	R^2
A		0.0151	1.0000
B		0.0183	0.9705
C		0.0059	1.0000
C (sac)		0.0065	1.0000
D		0.0141	0.9879
F		0.0027	0.3166
G		0.0140	0.9694
H		0.0006	0.0542
I		0.0041	0.9954
J		0.0038	0.7776
K		0.0030	0.6189

The annual expansion rates of the lumen were additionally calculated for successive scans and plotted as shown by Figure 27. A measure of eccentricity of the lumen was taken as shown by Equation 1 and plotted for each scan as shown by Figure 28.

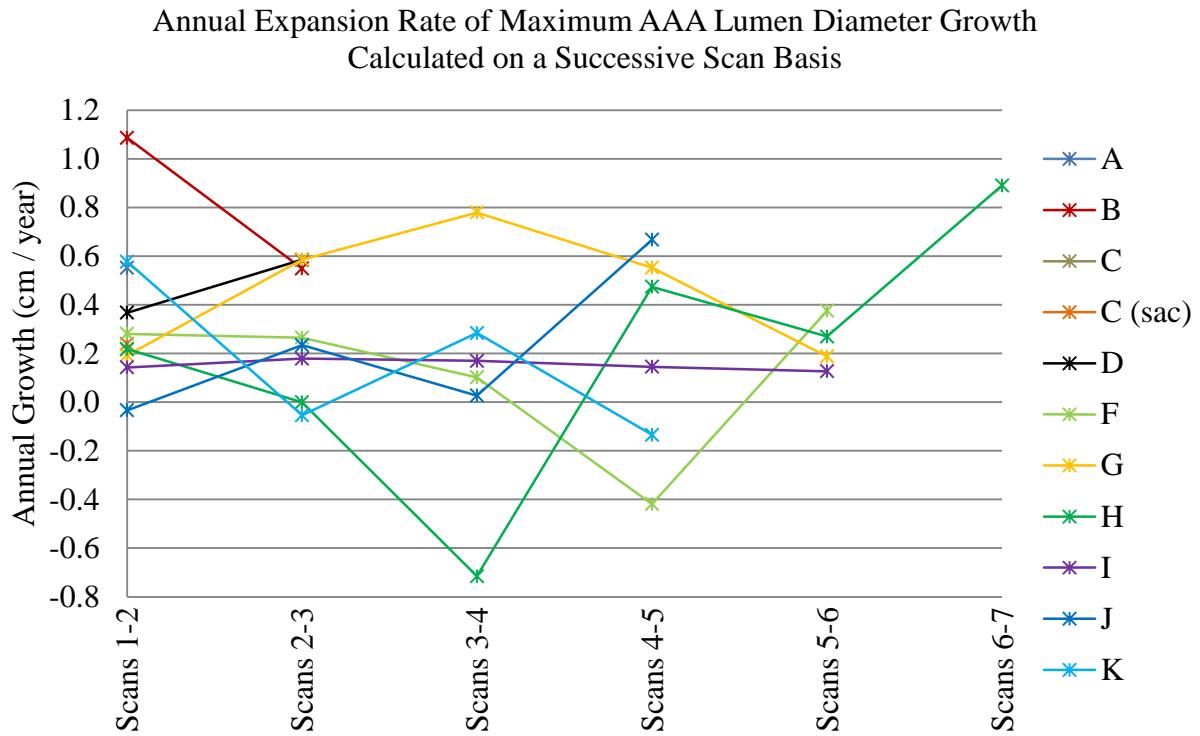


Figure 27. The annual expansion rate of maximum AAA lumen diameter growth calculated on a successive scan basis for each patient.

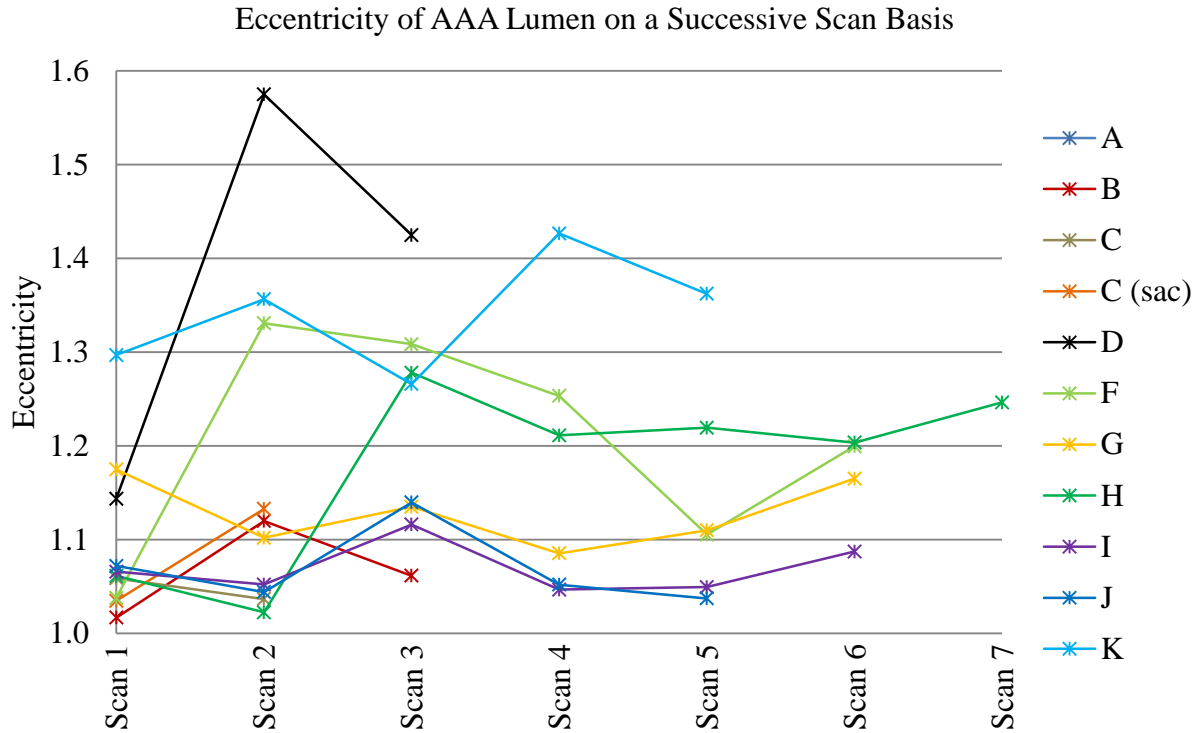


Figure 28. The lumen eccentricity based on eccentricity = $(D_{\max}) / (D @ 90^\circ \text{ to } D_{\max})$ for each patient scan.

3.4 Discussion

The results of the maximum tissue diameter study from Figure 23 are straightforward in that they all appear relatively linearly increasing. Other methods of fit were tested and found to have lower R^2 coefficients when compared to linear fits. Some positive trend was expected as AAA diameters continually increase during disease progression. A decrease in AAA maximum transverse diameter of the arterial tissue is only observed in the case from I1 – I2. The value appears to be approximately 3mm less than expected from the trend. Most likely the plane of acquisition was improperly judged and this value is not representative. The R^2 fitting values from Table 6 obtained by fitting linear trend lines to the tissue diameters are excellent at an average of 0.9681 ± 0.0287 . The actual rates of increase mostly all fall below 0.5 cm/year which

indicate relative stability of the AAAs. The estimated rate of increase for patient D, however, was over 0.54 cm / year. Some studies suggest less than 1 cm / year is stable, others suggest less than 0.5 cm / year is stable. Regardless, it is unclear why this patient's AAA, with a higher growth rate and the fact that monitoring began at a maximum tissue diameter over 5 cm, was allowed to progress as far as it did without treatment. On that same note, inspection of the maximum tissue diameter values clearly shows at least 21 / 49 measurements over 5 cm in maximum tissue diameter. Such measurements would suggest the dataset equally represents small and large AAAs, even though all are pre-EVAR. The successive scan calculated growth rate did not yield any interesting trends, aside from the possibility of some measurement error between scans F2 – F3 yielding an uncharacteristically high number. The scanning algorithms and resultant voxel resolutions are quite different between scans, leading to different standard deviations of measurement (Tables A.1 and A.2). For smaller vessel diameters the resolution of the voxels influences the results more significantly, such as between scans F2 – F3. By measuring the basic eccentricity for each scan it was hoped a clear trend would emerge reinforcing the idea of asymmetric growth, but no clear trends emerged across patients.

The results of the maximum lumen diameter from Figure 26 showed increasing diameters over time, as expected. For patients G & F it is interesting to note the large dip in diameter between 2000 – 2500 days. This dip is most likely due to growth of an ILT reducing the lumen volume at a rate faster than the entire vessel can expand. Fitting linear trend lines to the maximum diameter growth resulted in R^2 fitting parameters averaging 0.7901 ± 0.3276 (Table 7). Therefore the maximum lumen diameters did not fit linear trends as well as the maximum tissue diameters did. The successive scan calculated expansion rates offered both positive and

negative expansion rates. No doubt this is a combination of the chosen acquisition plane and relative growth of an ILT. Measuring maximum lumen diameter changes may be more beneficial if ILT measurements are made in the same plane concurrently. This would offer insight to the influence of ILT on maximum lumen diameter measurements. The eccentricity showed some favorable results and the range of eccentricity values recorded suggest significant variation amongst patients. Lumen eccentricity outweighed tissue eccentricity in that at least 13 lumen eccentricities were greater than the maximum tissue eccentricity. If the maximum tissue diameter and maximum lumen diameter were always measured in the same plane the ILT would represent the difference between the values after accounting for wall thickness. This would then no longer represent the maximum lumen diameter, however, as the maximum lumen diameter and maximum tissue diameter often occur in different planes and axes.

The methods followed suffer from subjectivity. Experienced screening personnel have an in-depth intuitive understanding of how to make these measurements according to their institution's guidelines to achieve reliable and repeatable results. No such personnel aided in the attainment of these measurements, and the overall accuracy was most likely decreased. No information could be found on established protocol for the analysis of longitudinal data. Perhaps there exist some unknown conventions to ensure a logical progression of recorded values that trained personnel are aware of. As longitudinal studies become more widespread proper protocols need to be established to standardize the interpretation of the results.

CHAPTER 4. Parameterization of Luminal and AAA Surfaces

4.1 Introduction

For an AAA *in vivo* there are multiple tissues contacting its boundary, none of which have been previously, fully considered for their effect throughout disease progression. Morphological features such as maximum diameter, asymmetry, cross-sectional polyline curvature flattening, tortuosity, and eccentricity are significantly influenced by both surrounding tissue and hemodynamic factors. In order to quantify either the combined or separate influence of such factors during disease progression a precise characterization of aneurysm's geometrical evolution is needed. Multiple methods for geometrical parameterization of abdominal aortic aneurysms (AAAs) have been previously developed using individual patient CT scan data but the focus has been mainly on the association of such geometrical parameters with the rupture risk and the efficacy of the parameterization is not fully investigated for a longitudinal study yet [60]. For this study a series of 3D models for AAAs in longitudinal studies, an arterial centerline generation algorithm (Appendices B.1 – B.6), and a geometric parameterization procedure for the arterial surfaces are developed.

An iterative algorithm was developed to generate a centerline for an arbitrary arterial surface model by collecting the center points of maximally inscribed spheres that fit within the surface boundaries at fixed travel intervals. The number of inscribed spheres is dependent on the choice of travel interval. Using the sphere center points and 4th order polynomial base functions, a smooth line approximation is made. The surface data is then parameterized to the centerline by defining an (s, θ) coordinate system where s is the travel length in mm along the centerline and 0

$\leq \theta \leq 2\pi$ radians. We then calculate r for each surface point where r is the minimum distance from the centerline to the point on the surface at a given (s, θ) . The parameterized surface $r(s, \theta)$ is then approximated by normal shape functions with fitting coefficients using a nonlinear least squares method. The change of the surface over time is calculated by the difference between these surface functions. The approximated surface can be regenerated in Cartesian coordinates. Alongside the parameterization technique a set of code was developed to characterize morphological features of the surface. The maximum diameter at each plane, the simplified eccentricity, and polyline curvature were then determined.

4.2 Methods

4.2.1 Importing the data

A 3-D point-cloud model is imported to Matlab. The point cloud model is essentially a subset of an STL model developed in Chapter 2 in that point cloud models are comprised of solely the vertices of STL models. The imported data is a matrix containing 3 columns for the x, y, and z coordinates across a number of rows representing the total number of coordinates. The model represents a closed surface with capped vessel ends. When defining the coordinate system inherited from the biomedical image processing methodology care must be taken. Depending on the scan, significantly different origin points were observed with respect to the STL positions. Registration serves to identify relative positions of one data set relative to another data set, but not across all sets. There is no single coordinate system to represent all scans, but a set of planes parallel to the x-y, y-z, and x-z planes for every scan can be identified (Figure 29). The unit of measure is millimeter.

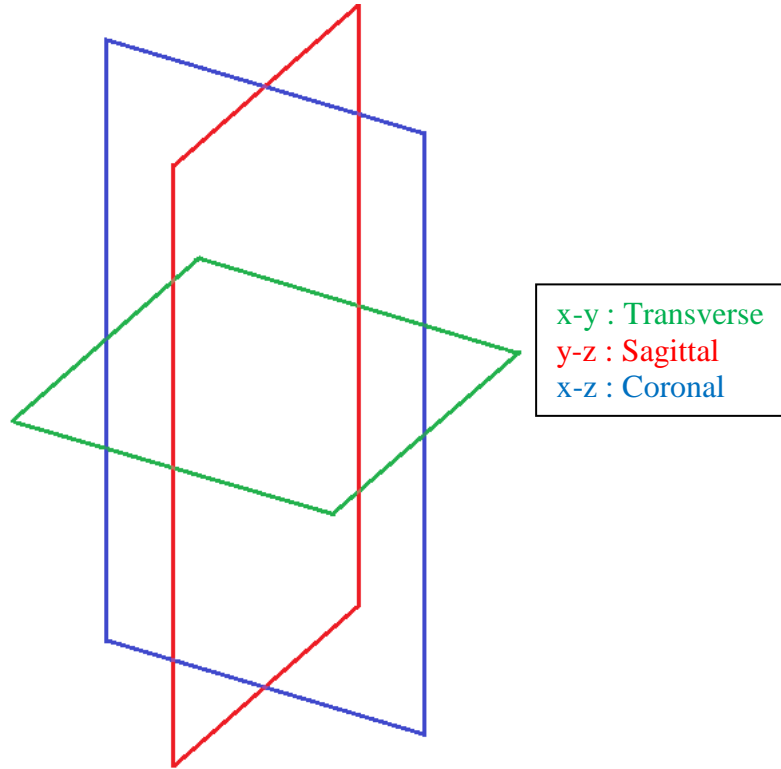


Figure 29. The coordinate planes inherited from the anatomical planes where the coordinate axis is such that the x-y plane is parallel to the transverse plane (green), the y-z is parallel to the sagittal plane (red), and the x-z plane is parallel to coronal plane (blue).

The coordinates of M unordered points in the model can be defined by Equation 2.

$$\mathbf{q}_N = (x_N, y_N, z_N) \text{ for } N = [1, \dots, M] \quad (2)$$

One requirement for the algorithm is that the vessel ends should be an open surface to accurately approximate centerline points at the model bounds. Therefore the volume of points is first truncated transversely immediately near the top and bottom to open the vessel ends with minimal removal of other points. Two truncation planes are identified from the top: $(\max(z_N) - 2.5)$ mm, and from the bottom: $(\min(z_N) + 2.5)$ mm, respectively. Only coordinates of \mathbf{q}_N within these bounds remain, and are processed through the rest of the calculations. Thus it is most

efficient to now consider that M be redefined as the total remaining points after truncation. The only variables carried forward are \mathbf{q}_N for $N = [1, \dots, M]$.

4.2.2 Centerline Generation Algorithm

The centerline generation algorithm serves to generate a centerline in the three-dimensional space. The previous method used most for centerline generation is the one that simply collects the centroids of transverse polylines [13], [23], [25], [29], [47–50]. The algorithm proposed in this work generates a centerline by fitting maximally inscribed spheres within the surface model constrained to planes approximately normal to the centerline at relatively evenly spaced intervals (Figure 30).

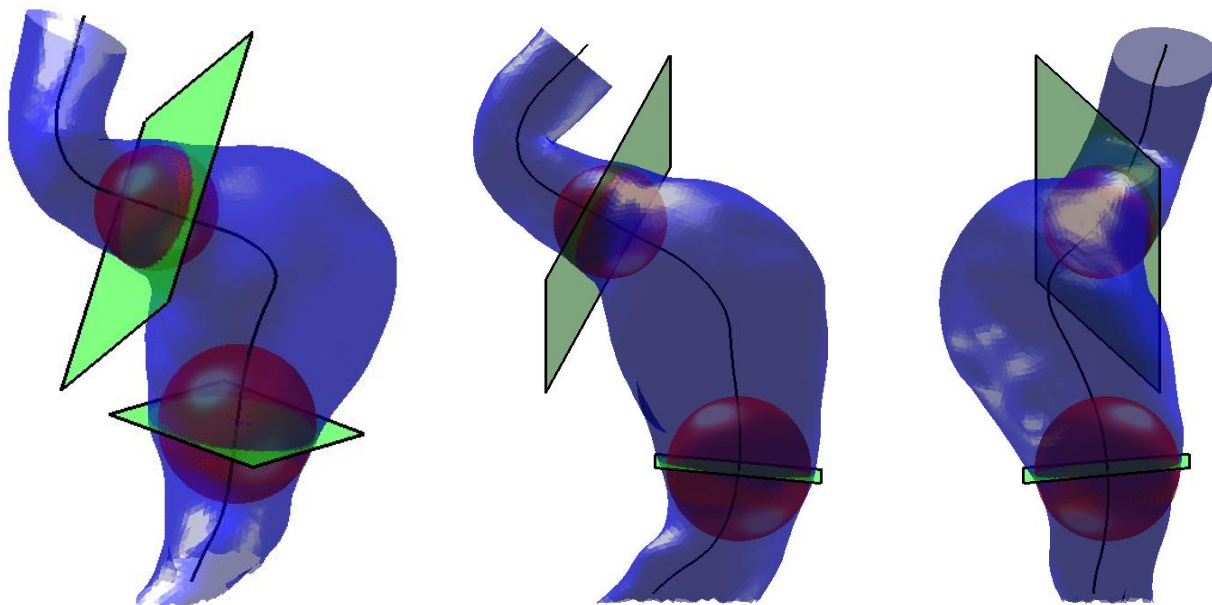


Figure 30. The arterial surface (blue) with two maximally inscribed spheres (red) and their respective constraint planes (green) shown. The centerline (black) is shown within the lumen model for scan B2 as seen from an isometric point of view (left), parallel to the x-z or coronal plane (center), and the y-z or sagittal plane (right).

The result is a set of n points $\mathbf{p}_i = (x_i, y_i, z_i)$ for $i = [1, \dots, n]$ that is constructing the centerline. The algorithm begins by selecting a set of points $(\mathbf{q}_1, \dots, \mathbf{q}_K)$ whose z values are bounded by $\min(\mathbf{q}_N(z))$ and $(\min(\mathbf{q}_N(Z))+g)$, where g is a constant variable defining a small gap. The first point \mathbf{p}_1 is then located to the middle of the set of points $(\mathbf{q}_1, \dots, \mathbf{q}_K)$ in the x - y plane and at the bottom in the z axis as shown by Equation 3.

$$\mathbf{p}_1 = \begin{bmatrix} \frac{\mathbf{q}_1(x) + \mathbf{q}_2(x) + \dots + \mathbf{q}_k(x)}{k} \\ \frac{\mathbf{q}_1(y) + \mathbf{q}_2(y) + \dots + \mathbf{q}_k(y)}{k} \\ \min(\mathbf{q}_N(z)) \end{bmatrix} \quad (3)$$

The distances d_N for $N = [1, \dots, M]$ to all points on the surface model \mathbf{q}_N for to the center point \mathbf{p}_1 are calculated by Equation 4.

$$d_N = \sqrt{(\mathbf{q}_N(x) - \mathbf{p}_1(x))^2 + (\mathbf{q}_N(y) - \mathbf{p}_1(y))^2 + (\mathbf{q}_N(z) - \mathbf{p}_1(z))^2} \quad (4)$$

The resulting vector \mathbf{A} corresponding to $\overrightarrow{\mathbf{p}_1 \mathbf{q}_N}$ at N for $\min(d_N)$ is then recorded. The center point \mathbf{p}_1 is then translated in the opposite direction of the projection of \mathbf{A} onto the x - y plane \mathbf{C} , simply the x and y components of \mathbf{A} in this case, a fixed distance t where t is a user-defined variable, usually 1 – 2 mm. If the absolute position of the center point has not changed by 1 mm over 15 iterations then the algorithm halves the translation amount and continues. This process of reducing the translation amount is repeated until a maximum number of iterations is met. When this process is completed the point \mathbf{p}_1 represents the approximate center point of a maximally inscribed sphere at the bottommost x - y plane of the volume. Essentially the z -

coordinate of a sphere is locked, and the sphere is allowed to grow and translate in the x-y plane until it reaches a maximum size and the center point p_1 is recorded. For the second center point p_2 the final (x,y) coordinates of p_1 are used, but vertical translation kv is applied where v is a user-input. Otherwise the estimation of p_2 continues the same as p_1 .

For each successive point referring to Figure 31 is extremely useful to visualize the terminology used. For each successive point for $n = 3$ onward the normal of the vector between the previous two center points $B = p_{n-1} - p_{n-2}$ is calculated and serves as the translation direction and v serves as the translation magnitude to determine the initial distance between the previous center point p_{n-1} and the current center point p_n . This serves to better place the initial guess to more quickly and accurately converge on the best value of p_n . Using B to place the initial guess of p_n is especially important for tortuous vessels. The point on the surface of q_N at a minimum distance to the center point p_n is calculated as well as the vector from p_n to q_N as A such that the minimum distance is equivalent to $\|A\|$. The center point p_n is then translated in the opposite direction of C , the projection of A onto the plane normal to B , by 1 mm where C is defined by Equation 5.

$$C = \frac{B \times \left(\frac{A \times B}{\|B\|} \right)}{\|B\|} \quad (5)$$

If the absolute position of the center point has not changed by 1 mm over 15 iterations then the algorithm halves the translation amount and continues. This process of reducing the translation amount is repeated until a maximum number of iterations is met.

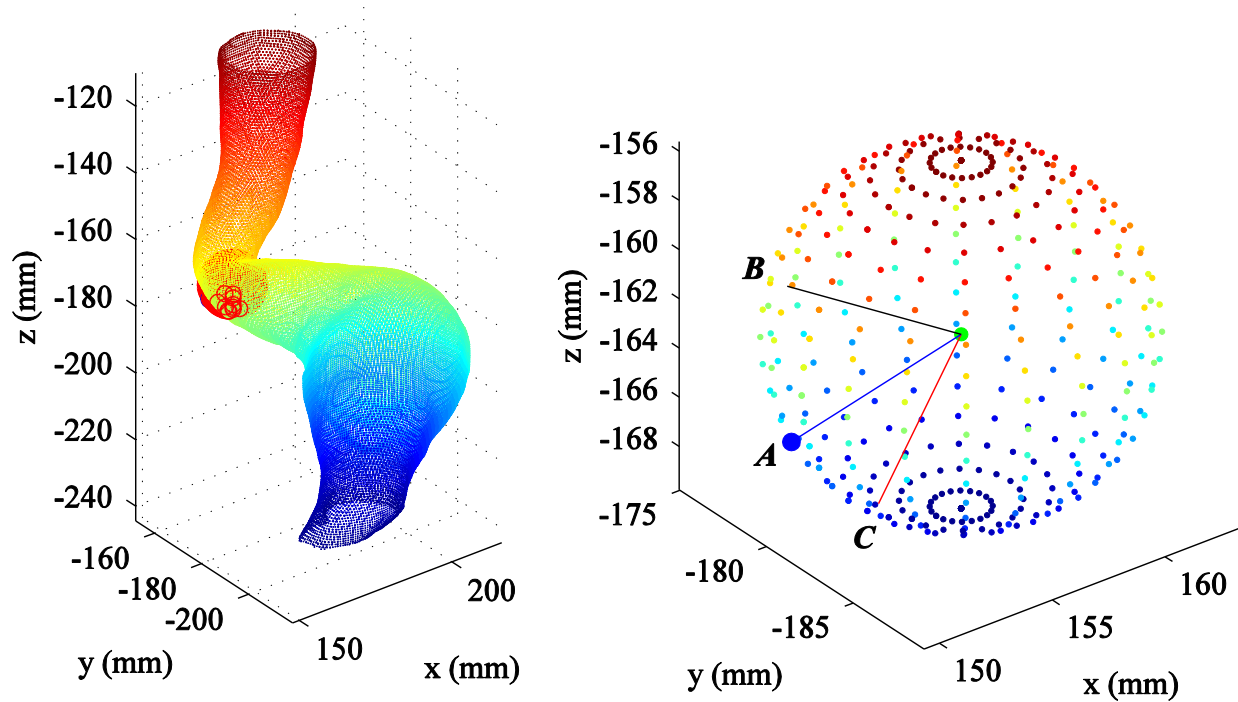


Figure 31. The lumen point cloud model for scan B2 colored by z-coordinate values with a red sphere at approximately (155, -180, -163) (left), and the sphere itself colored by z-coordinate values with vectors indicating the orientations of vectors **A** (blue), **B** (black), and **C** (red) for a sample center point (right).

This process is repeated until the z-value of an initial guess for p_n exceeds the maximum z-value of the model bounds, at which point the z-coordinate of p_n is reset to the maximum z-value and the final center point is recalculated using x-y plane projections in place of projections on the plane normal to **B**. The result is a collection of n points defined by $p_i = (x_i, y_i, z_i)$ for $i = [1, n]$ in Cartesian coordinates which approximate points on the centerline of the vessel, all other variables are discarded moving forward. The points attained from the centerline generation

algorithm represent approximations subject to surface roughness, approximation functions are now applied to attain a smooth centerline function and derive points on that line. The only variables carried forward to the next step are q_N for $N = [1, \dots, M]$ and p_i for $i = [1, \dots, n]$. An example of centerline approximation points is shown by Figure 32.

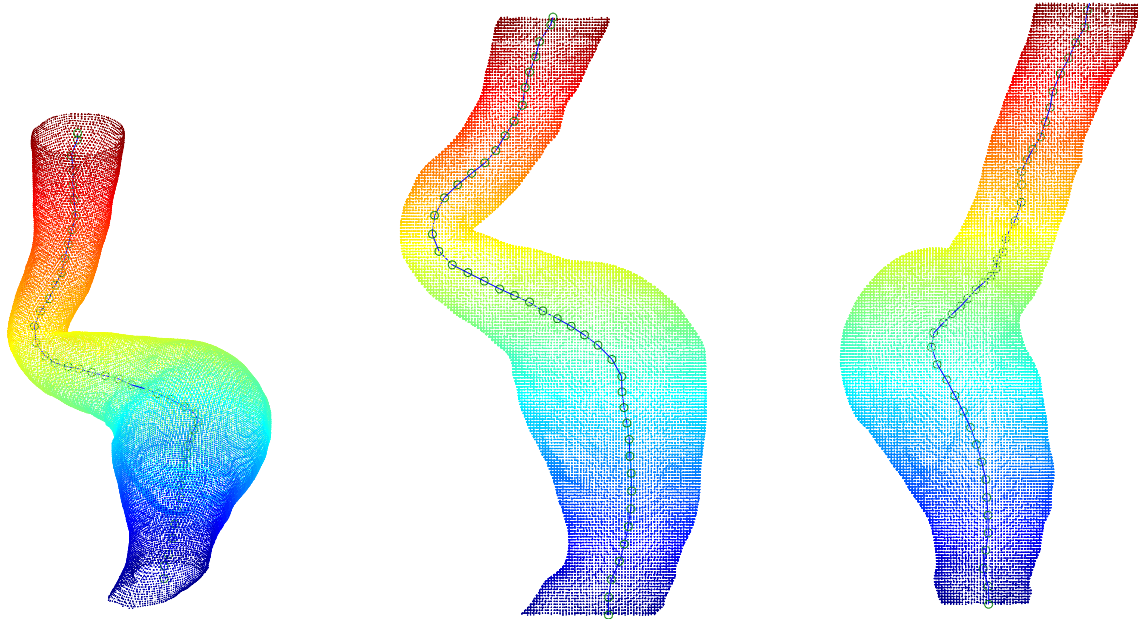


Figure 32. The final collection of centerline points plotted within the lumen point cloud model for scan B2 colored by z-coordinate value as seen from an isometric point of view (left), parallel to the x-z or coronal plane (center), and the y-z or sagittal plane (right).

4.2.3 Smooth Centerline Approximation

Based on the existing set of points from the centerline generation algorithm some new terms can be introduced. The successive distance between each of n points defined by $\mathbf{p}_i = (x_i, y_i, z_i)$ for $i = [1, \dots, n]$ is defined by resultant vectors as shown by Equation 6. The total distance traversed along the centerline from \mathbf{p}_1 to \mathbf{p}_i is defined as l_i by Equation 7.

$$d_j = \sqrt{(x_{j+1} - x_j)^2 + (y_{j+1} - y_j)^2 + (z_{j+1} - z_j)^2} \text{ for } j = [1, n - 1] \quad (6)$$

$$l_1 = 0 \text{ and } l_i = \sum_{j=1}^{i-1} d_j \text{ for } i = [2, n] \quad (7)$$

These quantities are shown for clarification in a diagram for $n = 7$ by Figure 33.

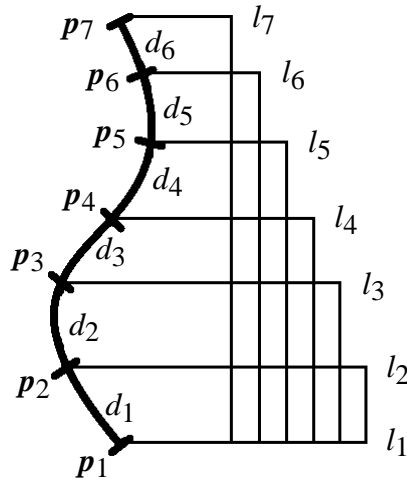


Figure 33. The meaning of \mathbf{p} , d , and l can be hard to ascertain from equations alone. The variable d represents the point to point distances between \mathbf{p} values. The variable l represents the sum of d values thus far at a given l .

The sum of the point to point distances l_n represents the length of the centerline. We define an integer set of m integers existing from $[0, l_n]$. Therefore if $l_n = 149.63$ for example, then $m = 149$ and 150 points will be defined on the smooth line approximation for s_k where $s \in \mathbb{R}_0^+$ and $k = [0, m]$. In this case a discrete set of s_k values is defined to produce and analyze a discrete set of longitudinal planes. From this definition of an s parameter a smooth approximation function can be generated based on the set of points \mathbf{p}_i . This method is adapted from a previous method employed in our lab by Zeinali-Davarani et al. [60]. Depending on a set of conditions outlined in Table 8 an appropriate interpolation function element $\phi^i(s)$ is constructed and its partial derivative $\partial\phi^i(s)/\partial s$ calculated for each s_k .

Table 8. Conditional table for shape function assignment of smooth line approximation.

	Condition	$\phi^i(s)$
<i>if i = 1</i>	$l_i \leq s \leq l_{i+2}$	$\frac{(s - l_{i+2})^2 (s + l_{i+2})^2}{(l_i - l_{i+2})^2 (l_i + l_{i+2})^2}$
	Else	0
<i>if i = 2</i>	$l_{i-1} \leq s \leq l_{i+2}$	$\frac{(s + l_i)^2 (s - l_{i+2})^2}{(l_i + l_i)^2 (l_i - l_{i+2})^2}$
	Else	0
<i>i ≠ 1 & i ≠ 2 & i ≠ n - 1 & i ≠ n</i>	$l_{i-2} \leq s \leq l_{i+2}$	$\frac{(s - l_{i-2})^2 (s - l_{i+2})^2}{(l_i - l_{i-2})^2 (l_i + l_{i+2})^2}$
	Else	0
<i>if i = n - 1</i>	$l_{i-2} \leq s \leq l_{i+1}$	$\frac{(s - l_{i-2})^2 (s - 2l_{i+1} + l_i)^2}{(l_i - l_{i-2})^2 (l_i - l_{i+1})^2}$
	Else	0
<i>if i = n</i>	$l_{i-2} \leq s \leq l_i$	$\frac{(s - l_{i-2})^2 (s - 2l_i + l_{i-2})^2}{(l_i - l_{i-2})^2 (l_i - l_{i-2})^2}$
	Else	0

After the interpolation function elements $\phi^i(s)$ are constructed and their partial derivatives $\partial\phi^i(s)/\partial s$ are calculated for each s the approximation function elements $\phi^i(s)$ and derivatives $\partial\phi^i(s)/\partial s$ are then normalized as $\varphi^i(s)$ and $\partial\varphi^i(s)/\partial s$ by Equations 8 and 9.

$$\varphi^i(s) = \frac{\phi^i(s)}{\sum_{i=1}^n \phi^i(s)} \quad (8)$$

$$\frac{\partial\varphi^i(s)}{\partial s} = \frac{\left((\partial\phi^i(s)/\partial s) (\sum_{i=1}^n \phi^i(s)) \right) - \left((\phi^i(s)) (\sum_{i=1}^n \partial\phi^i(s)/\partial s) \right)}{\left(\sum_{i=1}^n \phi^i(s) \right)^2} \quad (9)$$

The interpolation function $\varphi^i(s)$ is multiplied by \mathbf{p}_i and the sum of these multiplications at each s results in a point $\mathbf{X}_k = (x_k, y_k, z_k)$ such that the total collection of points represent points that lie on the smooth line approximation of the centerline as shown by Figure 34 by Equation 10.

$$\mathbf{X}_k(s) = \sum_i \varphi^i(s) \mathbf{p}_i \quad (10)$$

The derivative approximation function $\partial\varphi^i(s)/\partial s$ is also multiplied at each s by \mathbf{p}_i . The normalized sum of these multiplications for a given s results in a vector \mathbf{N}_1 by Equation 11.

$$\mathbf{N}_1 = \frac{\frac{\partial \mathbf{X}_k}{\partial s}}{\left\| \frac{\partial \mathbf{X}_k}{\partial s} \right\|} \quad \text{given} \quad \frac{\partial \mathbf{X}_k}{\partial s} = \sum_i \frac{\partial \varphi^i(s)}{\partial s} \mathbf{p}_i \quad (11)$$

A unique vector \mathbf{N}_1 exists for each s and represents a centerline tangent vector at $\mathbf{X}_k = (x_k, y_k, z_k)$. From \mathbf{N}_1 at each s additional vectors \mathbf{N}_2 and \mathbf{N}_3 can be calculated to form unique longitudinal coordinate bases at each point $\mathbf{X}_k = (x_k, y_k, z_k)$. The only variables carried forward to the next step are \mathbf{q}_N , \mathbf{X}_k , s , and \mathbf{N}_1 .

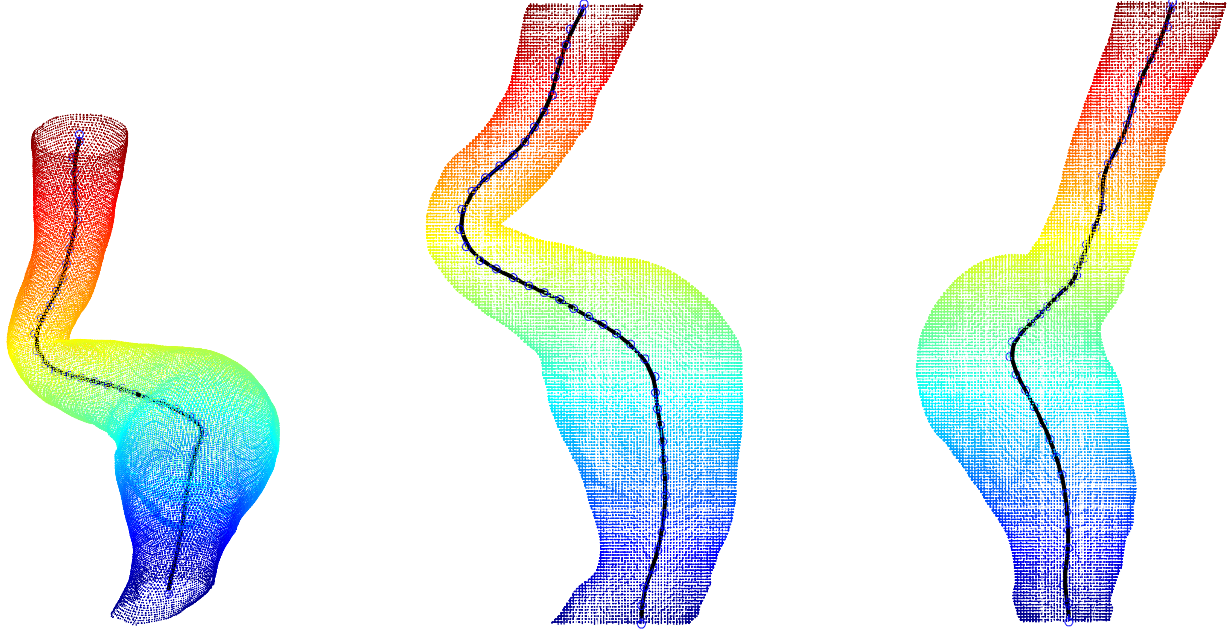


Figure 34. The final collection of centerline points plotted within the point-cloud lumen model of scan B2 colored by z-coordinate value and the fitted centerline (black) as seen from an isometric point of view (left), parallel to the x-z or coronal plane (center), and the y-z or sagittal plane (right).

4.2.4 Longitudinal Acquisition Plane Generation

As described in the previous section, tangent vectors N_1 exist for each s originating from the point X_k for $k = [1, m]$. In order to fully define a longitudinal acquisition plane two additional coordinate basis vectors N_2 and N_3 must be calculated (Figure 35). The transverse plane, on the other hand, uses the known Cartesian standard basis $\{i, j, k\}$. The longitudinal plane at each s is defined by projection of the x-axis onto the plane perpendicular to N_2 , and therefore $N_3 = N_1 \times N_2$ by Equation 12.

$$N_2 = \frac{i - N_1(i \cdot N_1)}{\|i - N_1(i \cdot N_1)\|} \quad (12)$$

Approximated Centerline with N_1 , N_2 , and N_3 Vectors at each point s

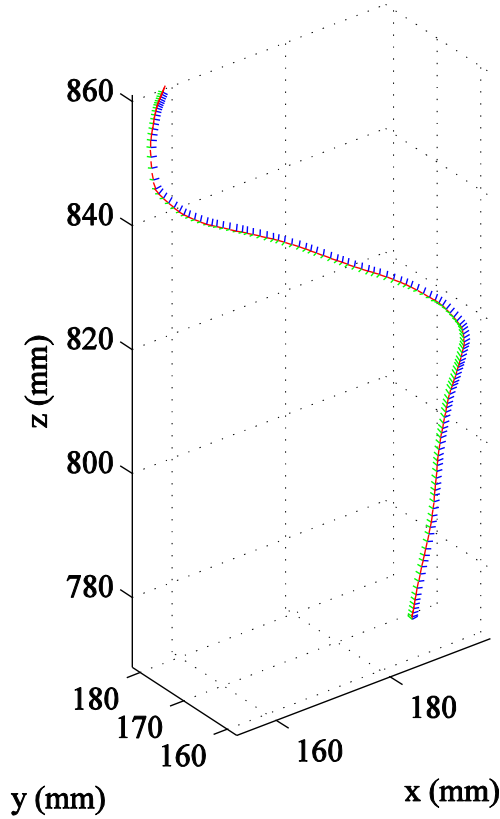


Figure 35. The vectors N_1 (red), N_2 (blue) and N_3 (green) are plotted for each s originating from the points X_k for $k = [1, m]$ for the lumen model of scan B2.

Points lying on the longitudinal planes defined by (N_1, N_2, N_3) can then be determined through use of the dot product. For each s the vectors from X_k to all points on the surface model q_N , or $\overrightarrow{X_k q_N}$, are calculated for all combinations for $k = [1, m]$ and $N = [1, M]$. A dot product inequality is evaluated and the vector results are stored for valid pairs of k & N as r_h by Equations 13 and 14.

$$-0.01 < N_1 \cdot \overrightarrow{X_k q_N} < 0.01 \quad (13)$$

$$r_h = \langle \overrightarrow{X_k q_N}(x) \mathbf{i}, \overrightarrow{X_k q_N}(y) \mathbf{j}, \overrightarrow{X_k q_N}(z) \mathbf{k} \rangle \quad (14)$$

h is the number of points X_k which lie in longitudinal planes. As r_h is additionally populated the associated surface points q_N are stored in a new point-cloud volume v_h representing only points that lie on the longitudinal planes defined by (N_1, N_2, N_3) . An example clarifying these variables is shown by Figure 36.

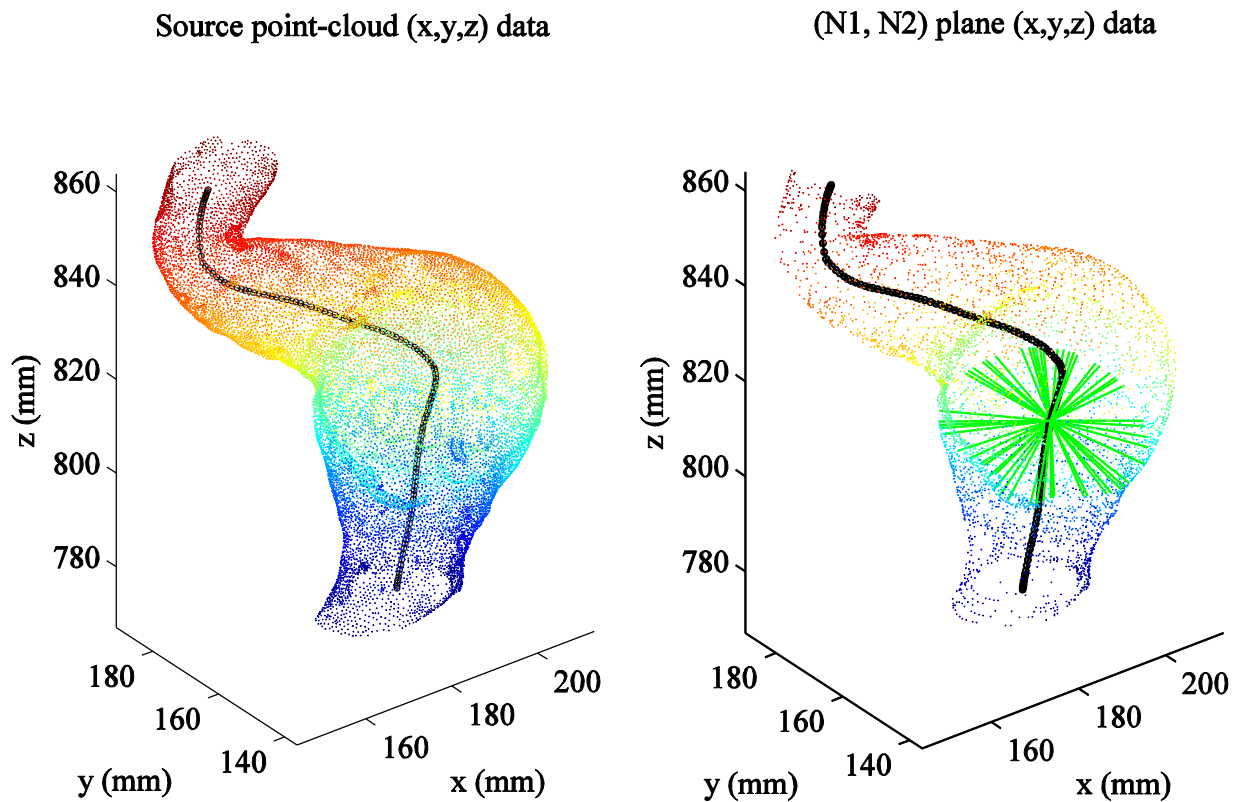


Figure 36. The imported point-cloud lumen model composed of points q_N for scan B2 colored by z-coordinate value with points on the smooth approximated centerline shown (black, left), and the subset of points v_h colored by z-coordinate value from the point-cloud lumen model for scan B2 which lie on longitudinal planes defined by (N_1, N_2, N_3) (right). For example, the vectors in r_h from X_k to the associated points on the surface v_h at the plane defined by (N_1, N_2, N_3) for $k = 40$ are shown in green (right).

The determination of points lying on the longitudinal planes at s only using dot product thresholding reports extra erroneous values when planes intersect the surface at more than one boundary. To compensate for this phenomenon the magnitude of each vector from r_h for a longitudinal plane at s is calculated and analyzed. If a vector's magnitude is greater than the minimum vector magnitude in that plane by some threshold, say 5 mm, the vector is removed from r_h . A more statistically justified approach was originally implemented, but was found unreliable across geometries. The method described requires a small degree of user-guided iteration to ensure accurate results in place of full statistical automation, but was deemed an appropriate trade-off with regards to development time (Appendices B.1 – B.6). The magnitudes of vectors within r_h represent the radius from the centerline points X_k to the surface points v_h . The mean and maximum radius at each longitudinal plane can be found as a useful measure of growth (Figure 37).

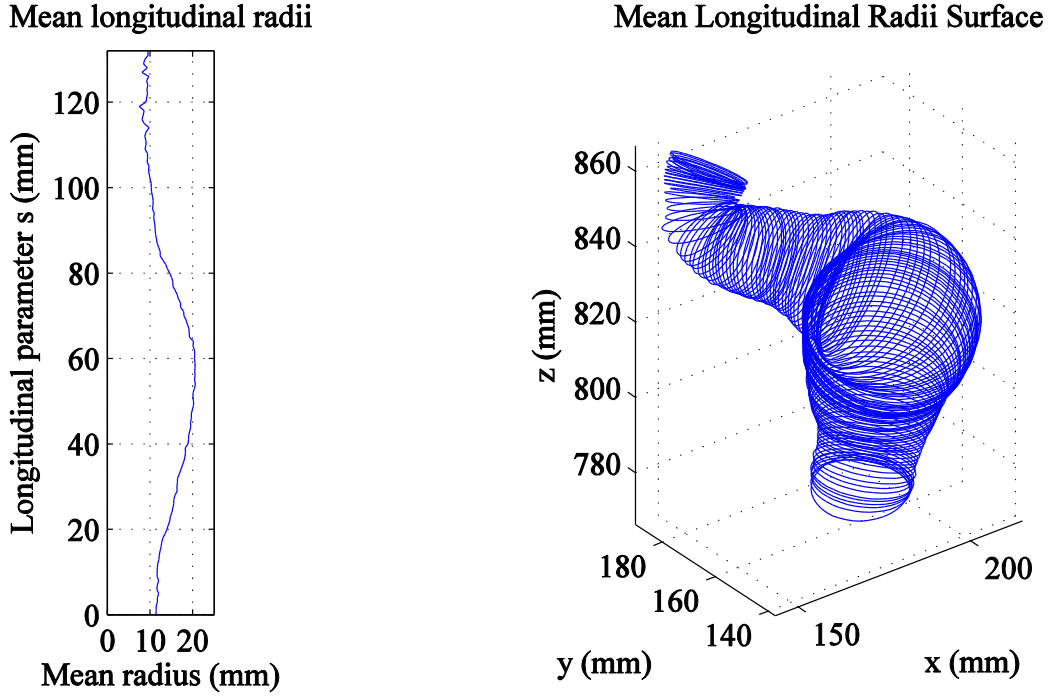


Figure 37. The radii values are calculated for all h by $\|r_h\|$. The mean is then calculated at each longitudinal plane for the lumen of scan B2 (left), and the circles of mean longitudinal radii at each longitudinal plane can be visualized for the lumen of scan B2 (right).

4.2.5 Parameterization of Cross Sections into $r(s, \theta)$

At each longitudinal plane defined by (N_1, N_2, N_3) a collection of vectors r_h exists in Cartesian coordinates that describe the distance from the centerline point X_k to surface points q_N . To more efficiently analyze the data on a longitudinal plane basis a transformation to polar coordinates takes place. In polar coordinates the magnitudes of r_h vectors represent r . By considering a suite of dot products between each r_h vector, N_1 , and N_2 within each longitudinal plane at a given s the angular values θ within that plane associated with each r_h can be obtained. First a set of 4 calculations determines if the value of θ is $0, \pi/2, \pi,$ or $3\pi/2$. If the dot product

does not correspond to one of those exact values then the region θ lies in can be determined and θ subsequently calculated. This process is clarified by Table 9 and Figure 38.

Table 9. Conditional table for calculation of θ from a given \mathbf{r}_h vector. First it is determined whether θ lies on the N_2 , N_3 , $-N_2$, or $-N_3$ axis. If it does not lie on an axis than the region it lies in is determined and θ is calculated appropriately.

1 st	$\mathbf{r}_h \cdot \mathbf{N}_2 = 1$	$\theta = 0$
	$\mathbf{r}_h \cdot \mathbf{N}_3 = 1$	$\theta = \pi/2$
	$-\mathbf{r}_h \cdot \mathbf{N}_2 = 1$	$\theta = \pi$
	$-\mathbf{r}_h \cdot \mathbf{N}_3 = 1$	$\theta = 3\pi/2$
2 nd	$(\mathbf{r}_h \cdot \mathbf{N}_2 > 0 \ \& \ \mathbf{r}_h \cdot \mathbf{N}_3 > 0)$ or $(\mathbf{r}_h \cdot \mathbf{N}_3 > 0 \ \& \ \mathbf{r}_h \cdot \mathbf{N}_2 < 0)$	$\theta = \cos^{-1}(\mathbf{p}_2 \cdot \mathbf{N}_2)$
	$(\mathbf{r}_h \cdot \mathbf{N}_2 > 0 \ \& \ \mathbf{r}_h \cdot \mathbf{N}_3 < 0)$ or $(\mathbf{r}_h \cdot \mathbf{N}_2 < 0 \ \& \ \mathbf{r}_h \cdot \mathbf{N}_3 < 0)$	$\theta = -\cos^{-1}(\mathbf{p}_2 \cdot \mathbf{N}_2) + 2\pi$

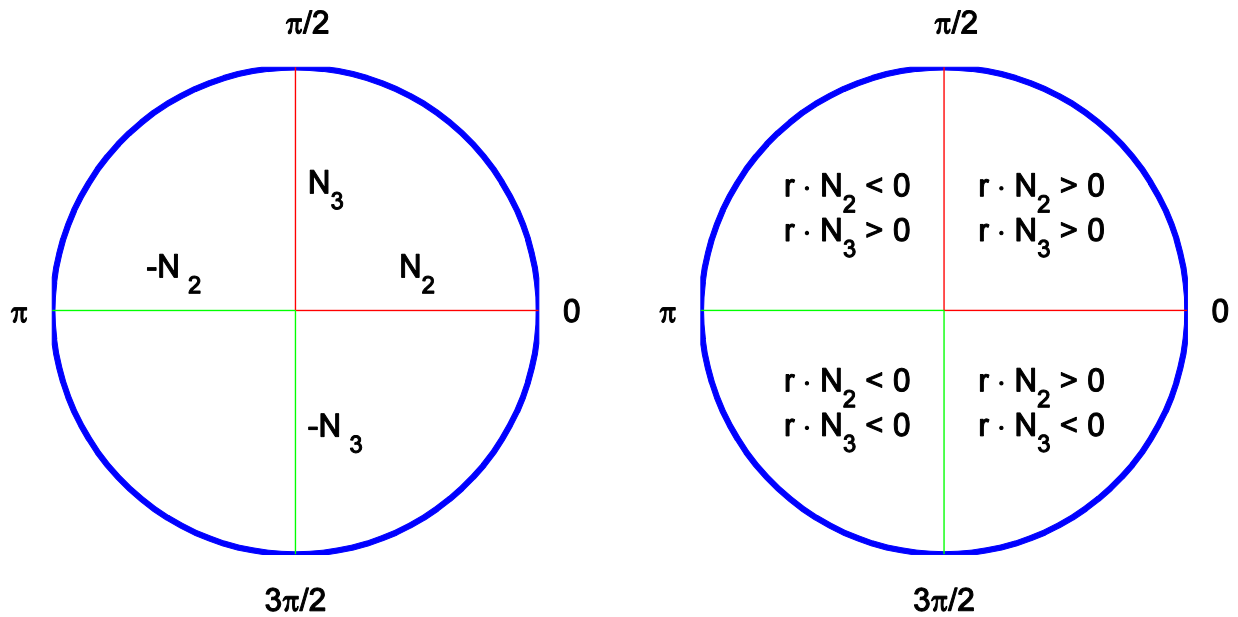


Figure 38. Schematic representation for the calculation of θ from a given r_h vector. First it is determined whether θ lies on the N_2 , N_3 , $-N_2$, or $-N_3$ axis (left), and if it does not lie on an axis then the region it lies in is determined and θ is calculated appropriately (right).

4.2.6 Coordinate transformation from $r(s, \theta)$ to (x, y, z)

Successfully parameterizing the data from (x, y, z) space to $r(s, \theta)$ space allows for unique surface visualization of the cross-sectional radii along the vessel circumference relative to the vessel centerline parameter s (Figure 39).

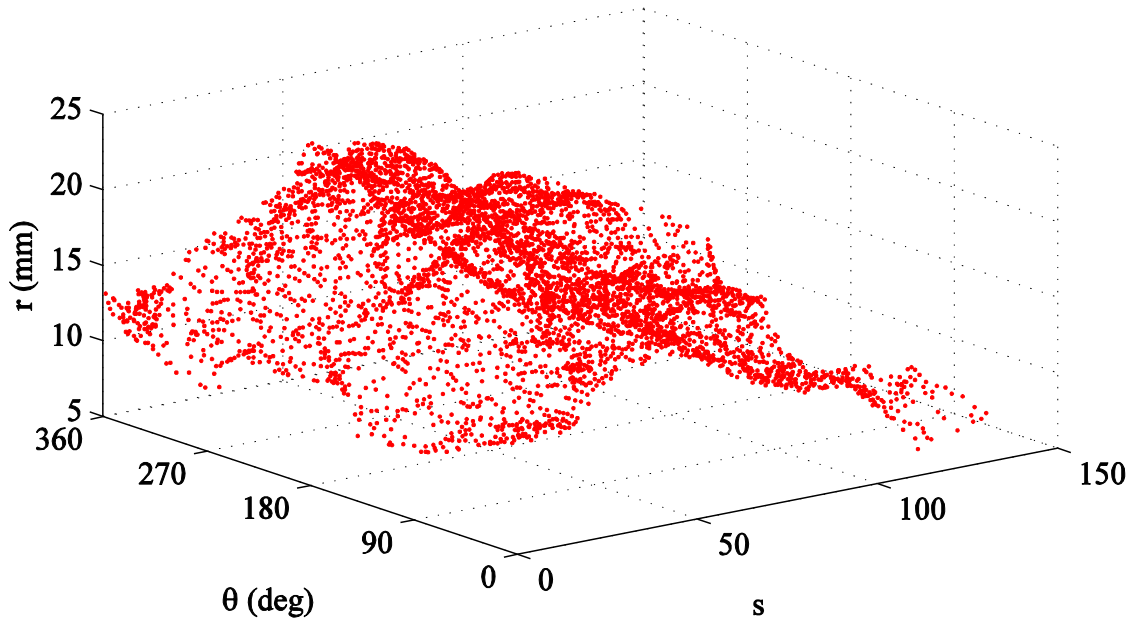


Figure 39. Parameterized surface data (red) from scan B2 shown as $r(s, \theta)$ surface.

From the parameterized coordinate system any point can be reconstructed within the Cartesian coordinate system through coordinate transformations. Each longitudinal plane is first assumed to share an origin with the Cartesian origin to determine the relative rotation of the plane. Given that $\langle N_2, N_3, N_1 \rangle$ represents the unit vector basis at each s , and that $\langle e_i, e_j, e_k \rangle$ represents the unit vector basis in Cartesian coordinates a rotation transformation tensor between each basis is attainable. In reality there exist translation transformation vectors at each longitudinal plane defining translation from the origin. These vectors are derived from the centerline point X_k for each s . This two-step transformation allows for the reconstruction of the surface from $r(s, \theta)$ coordinates to Cartesian coordinates at each s first by rotation and then by translation. The transformation of any given $r(s, \theta)$ point at a given s to any given (x, y, z) point is thus given by Equation 15.

$$\begin{bmatrix} x \\ y \\ z \end{bmatrix} = \begin{bmatrix} N_2 \cdot e_i & N_3 \cdot e_i & N_1 \cdot e_i \\ N_2 \cdot e_j & N_3 \cdot e_j & N_1 \cdot e_j \\ N_2 \cdot e_k & N_3 \cdot e_k & N_1 \cdot e_k \end{bmatrix} \begin{bmatrix} r \cos \theta \\ r \sin \theta \\ 0 \end{bmatrix} + \begin{bmatrix} X(x) \\ X(y) \\ X(z) \end{bmatrix} \quad (15)$$

It is apparent that reconstruction of the points into Cartesian coordinates is straightforward and directly applicable to any set of data in longitudinal planes. Therefore any fit or approximation of the parameterized surface is directly transformable back to Cartesian coordinates (Figure 40).

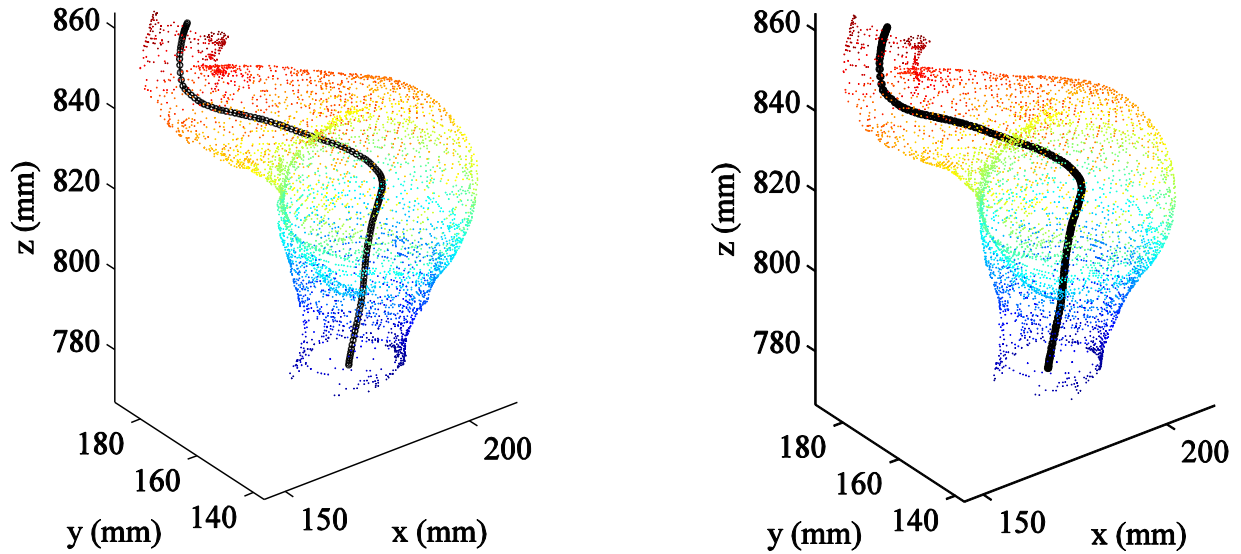


Figure 40. Subset of the original point cloud data which lie on longitudinal planes (left) and the data reconstructed from the $r(s, \theta)$ data (right).

4.2.7 Surface Approximation

After using the parameterization presented in the previous section, the distance of each point on the surface from the centerline, r , is plotted with respect to two variables $\{s, \theta\}$ as seen in Figure 39. In this section, we present a smooth numerical approximation of the surface with a function $r(s, \theta)$. The numerical code for the approximation in MatLab can be found at

Appendices B.7 and B.8. Figure 41 shows the schematic diagram for the parameterization and the functional approximation.

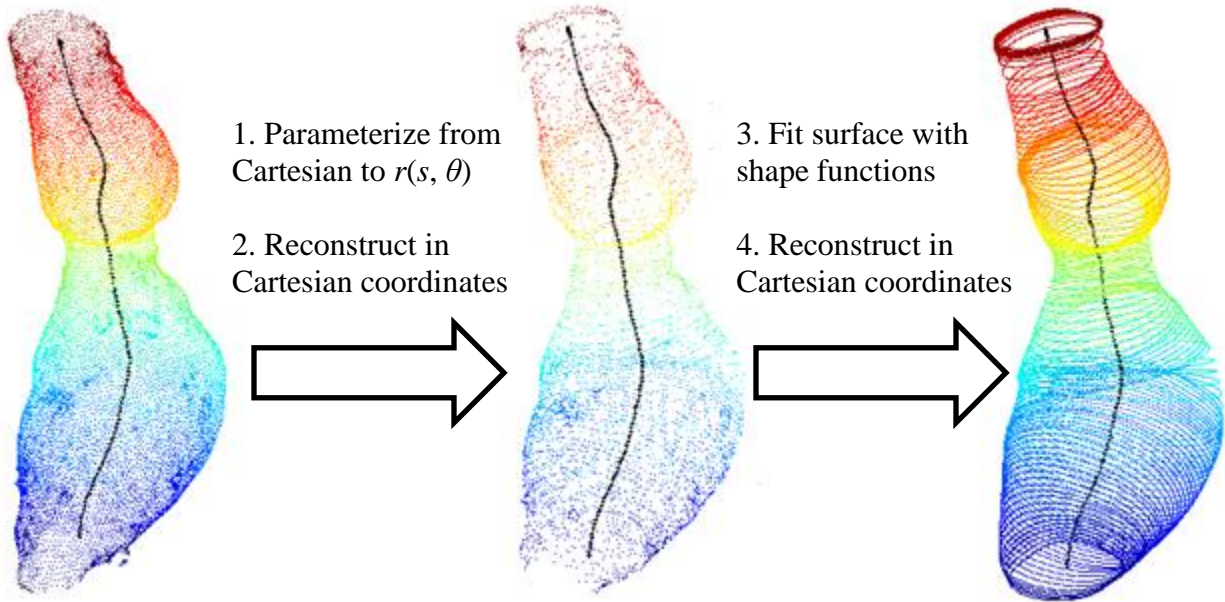


Figure 41. A sample arterial lumen surface from scan C2 (left) is shown to undergo the steps of parameterization (center) followed by surface approximation (right) with the optional reconstruction to Cartesian coordinates shown for clarity in both cases.

The surface is approximated by a linear combination of fitting parameters and shape functions, i.e., $r(s, \theta) = \sum \alpha_k \phi_k(s, \theta)$, where the shape functions are defined at $N_s \times (N_\theta - 1)$ nodal points. N_θ and N_s are the number of grids in the domain along the θ and s axes. The parameterized data is special in the sense that θ spans from 0 to 2π radians, but the continuity between $\theta = 0$ radians and $\theta = 2\pi$ radians should be ensured. For this reason, the shape functions at $\theta = 2\pi$ become not independent and the shape functions are defined from 1 to $(N_\theta - 1)$ in the circumferential axis. Given the variable θ is connected at 0 and 2π , the shape function must

reflect this. For this, let us define new variables $d\theta_i$ and ds_j by Equation 16. The shape function at k^{th} node is then defined by Equation 17.

$$d\theta_i = \min\{|\theta - \theta_i|, 2\pi - |\theta - \theta_i|\} \quad \text{and} \quad ds_j = |s - s_j| \quad (16)$$

$$\varphi_k = \exp\left(-\beta_1 ds_j^2 - \beta_2 d\theta_i^2\right) \quad (17)$$

β_1 and β_2 are two fitting parameters, which requires optimization for the given number of shape functions. Finally the resulting approximations α can be obtained by using the least squares method. To optimize β_1 and β_2 an iterative solver, `fminsearch` [61], in MatLab is employed to minimize the squared sum of the residual error to a convergence tolerance of 0.0001 based on initial guesses of $\beta_1 = 0.009$ and $\beta_2 = 1.5$. This allows for the determination of points approximated by shape functions from each $r(s, \theta)$ value based on the residual error between the data and the approximation value (Figures 42 and 43). From this optimization any point of the parameterized surface can then be defined by the resulting shape functions (Figure 44).

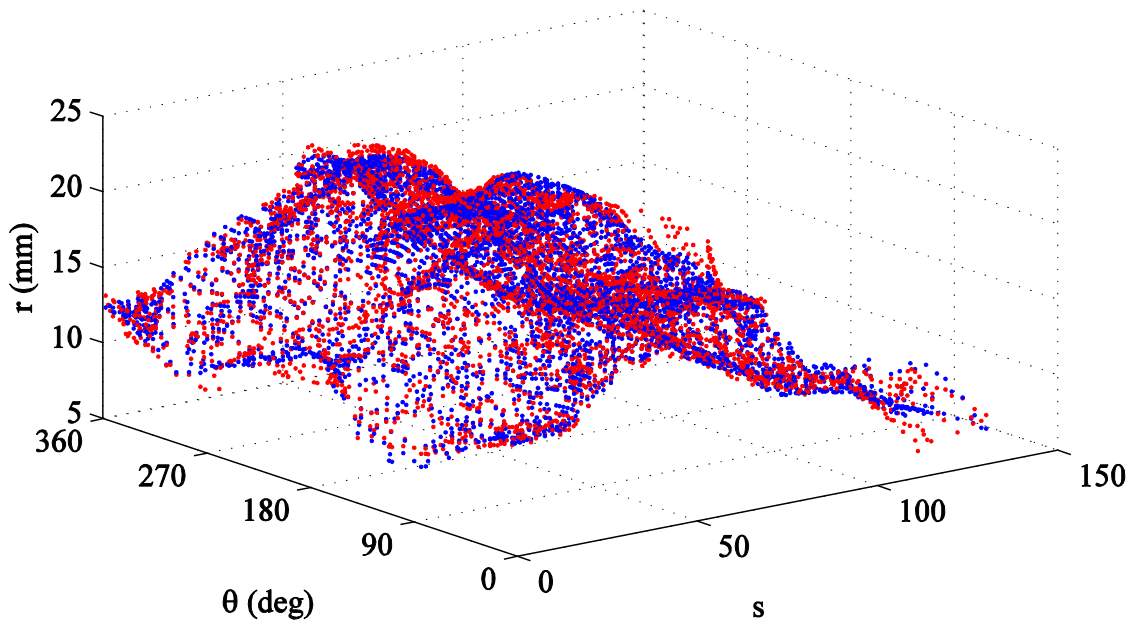


Figure 42. Parameterized surface data (red) and the respective points from the best fit surface (blue) from scan B2 shown as $r(s, \theta)$ surfaces.

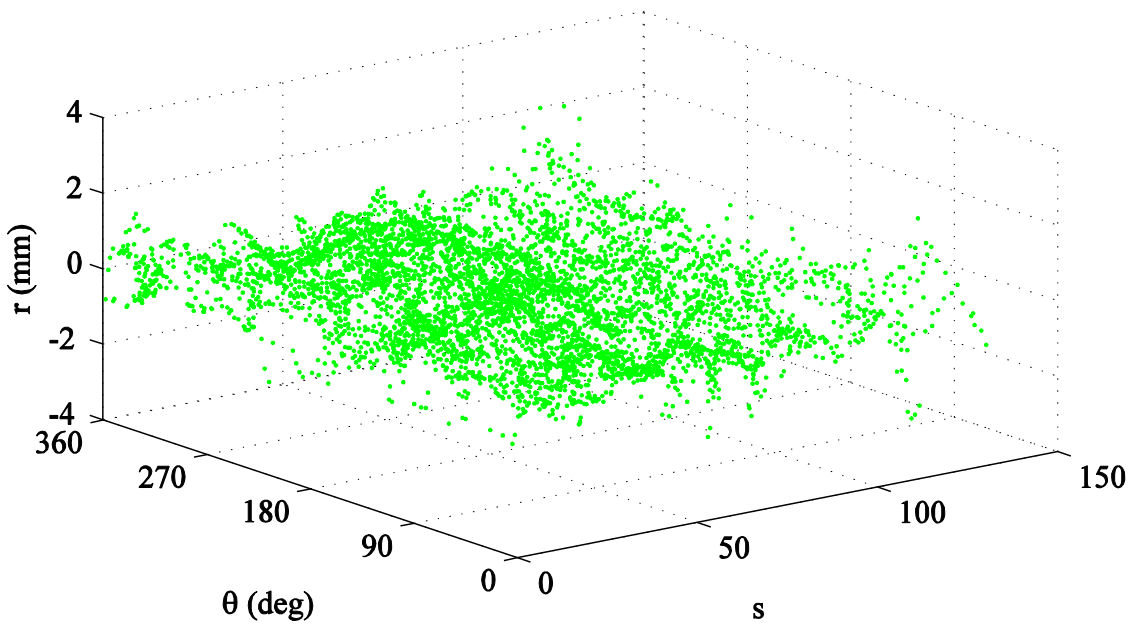


Figure 43. Plot of the residual error between the parameterized surface data and the respective points from the best fit surface from scan B2 shown as an $r(s, \theta)$ surface.

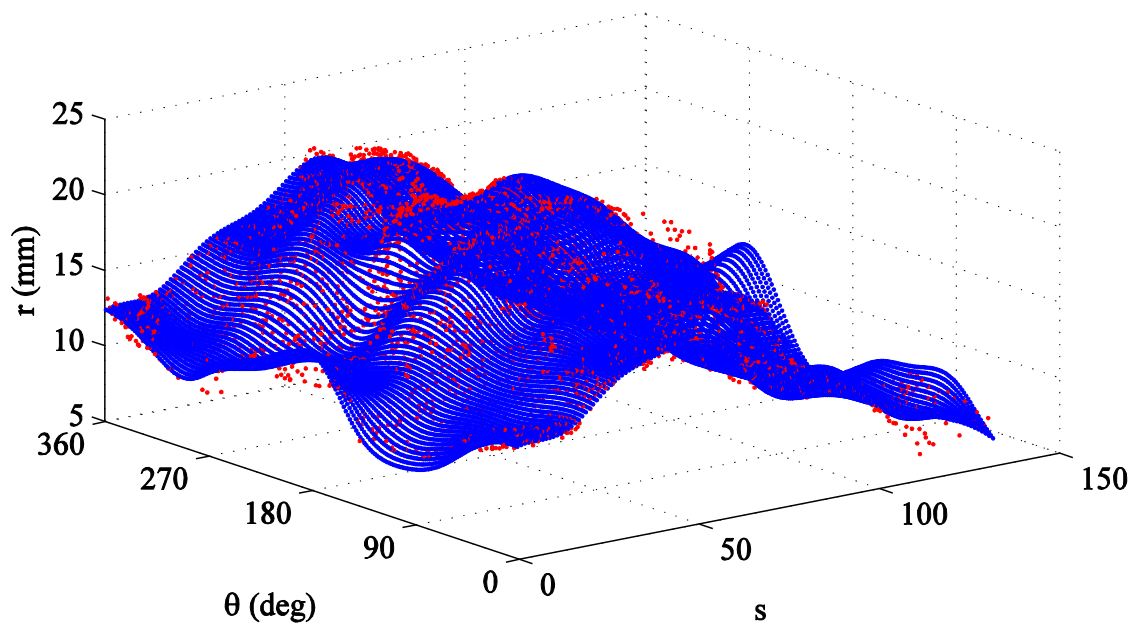


Figure 44. Parameterized surface data (red) and the respective cross-sectional lines from the best fit surface (blue) from scan B2 shown as $r(s, \theta)$ surfaces.

4.2.8 Eccentricity and Polyline Curvature

Eccentricity and polyline curvature are two morphological features which can be examined on the cross-sectional level. Mathematically the eccentricity of a conic-section is based on the ratio between the semimajor axis and the distance along the semimajor axis at which the focus lies. Some alternatives exist which are simplified and carry slightly different formulations, though all represent the tendency of a conic-section towards or away from circularity. A clear measure of eccentricity intrinsically understood by medical professionals is simply the ratio between the diameter of a cross-section's major and minor axes. This can be automated by finding the largest distance between two points of a cross-section iteratively as the major axis, and then identifying the axis joining the point pair closest to 90° to the major axis as the minor axis (Figure 45).

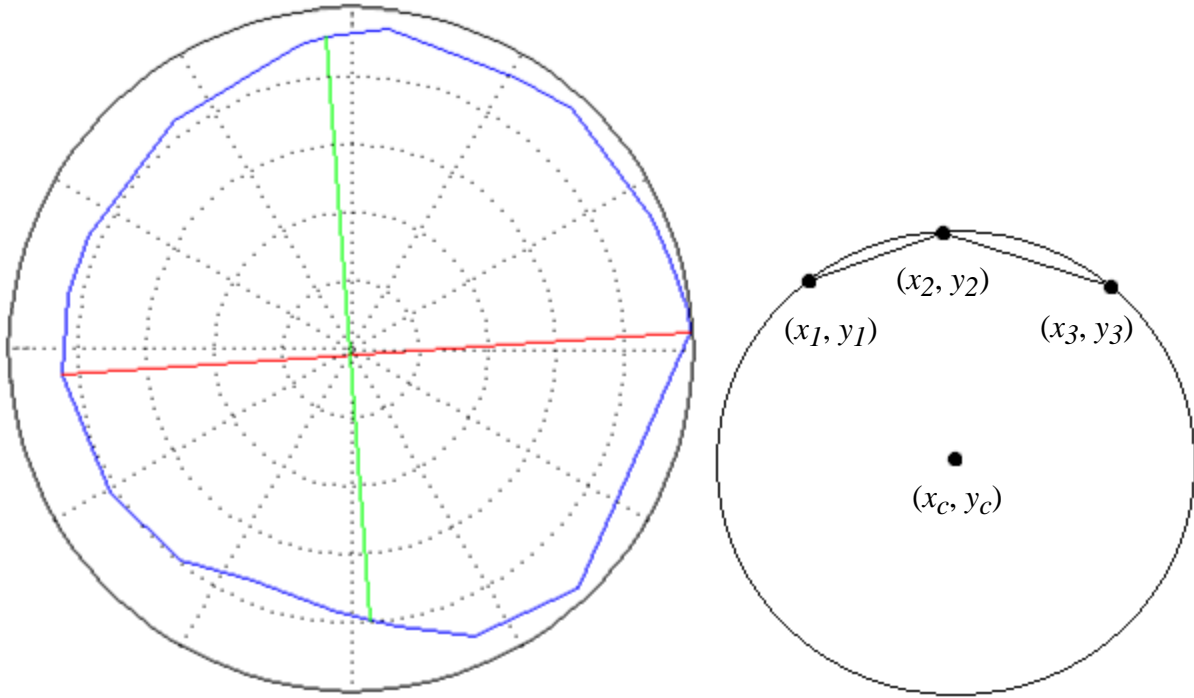


Figure 45. Major axis (left, red) and minor axis (left, green) of a cross-section (blue) used for eccentricity determination. Terminology of the 3-point polyline curvature method is detailed (right).

To define polyline curvature, a two dimensionally derived value, many methods were available. The chosen method was by defining the curvature at a given point (x_2, y_2) to be the inverse of the radius of a circle fit to that point and two neighboring points (x_1, y_1) and (x_3, y_3) by first finding the center of the circle (x_c, y_c) by Equations 18 and 19.

$$x_c = \frac{m_1 m_2 (y_1 - y_3) + m_2 (x_1 + x_2) - m_1 (x_2 + x_3)}{2(m_2 - m_1)} \quad (18)$$

$$y_c = \frac{1}{m_1} \left(x_c - \frac{x_1 + x_2}{2} \right) + \frac{y_1 + y_2}{2} \quad (19)$$

After identifying the center of the circle based on 3 points the radius, and therefore the inverse of the radius, can be calculated by considering the center of the circle (x_c, y_c) and any of the points (x_1, y_1) , (x_2, y_2) , or (x_3, y_3) by Equations 20 and 21.

$$Radius = \sqrt{(x_2 - x_1)^2 + (y_2 - y_1)^2} \quad (20)$$

$$Curvature = \frac{1}{Radius} \quad (21)$$

The processes for eccentricity and polyline curvature were both automated (Appendices B.9 and B.10)

4.3 Results

4.3.1 Centerline generation

The centerline generation algorithm was ran for 59 cases and it was able to successfully generate centerline points for 55 / 59 cases, or $\approx 93\%$ of cases with the default input parameters. The failed models were lumen models from scans D3, F5, H3, and K3 with their error detailed in Appendix C (Figures C.1 – C.4). By tweaking the input parameters to generate fewer points at a higher number of iterations per point models were then successfully generated for scans F5, H3, and K3. Scan D3 featured a highly irregular anomaly that was outside the scope of the algorithm completely. The centerlines of patient H are highlighted below (Figures 46 and 47).

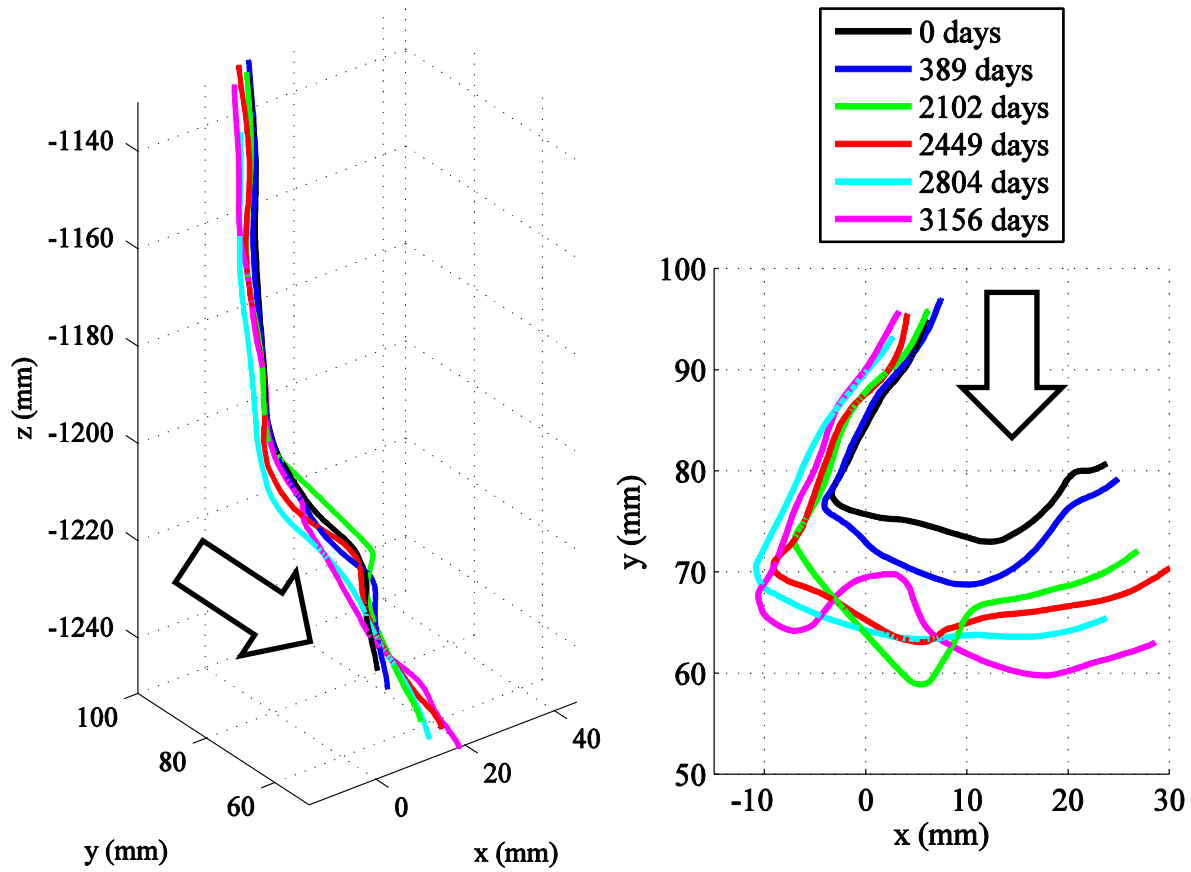


Figure 46. Isometric view of the centerlines (left) and a transverse view (right) for scans H1 – H5 where black, blue, green, red, cyan, magenta represent H1, H2, H3, H4, H5, H6 respectively. In this case the general region of the spine is the x-z plane at $y = 100$ such that the arrow indicates migration away from the spine.

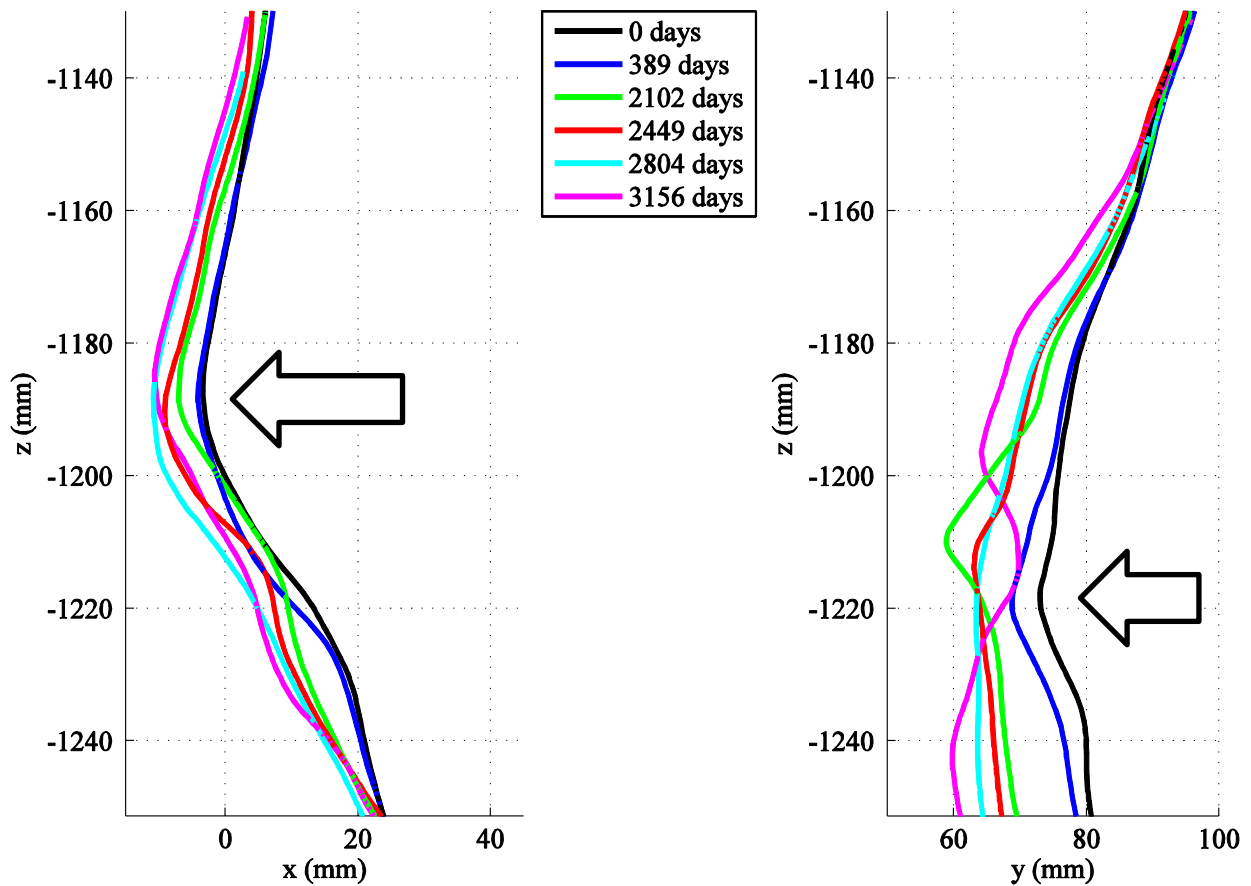


Figure 47. x-z/frontal/coronal view of the centerlines (left), and y-z/sagittal view of the centerlines (right) for scans H1 – H5 where black, blue, green, red, cyan, magenta represent H1, H2, H3, H4, H5, H6 respectively. In the x-z plane (left) migration of the vessel centerline is taking place towards the left, and in the y-z plane (right) migration is also taking place towards the left. In this case the general region of the spine is the x-z plane at $y = 100$ such that the arrow indicates migration away from the spine.

4.3.2 Eccentricity and Curvature

The results of the eccentricity ratio and 3-point polyline curvature parameter measurements for the arterial lumen surface of B2 are shown (Figures 48 and 49). It is clear that eccentricity of cross-sections differ along s in an easily understood manner such that more elliptical cross-sections have higher eccentricities. The polyline surface curvature is a bit less

intuitive. Lower values represent flatter surfaces, and were expected at regions of contact with the spine. This appears to be present at two points in the proximal posterior and left lateral sides. There are 4 visible stripes of extreme curvature representing $\theta = 0, \pi/2, \pi,$ and $3\pi/2$. Due to a lack of foresight the method used did not account for sinusoidal behavior at these values, though it very easily could.

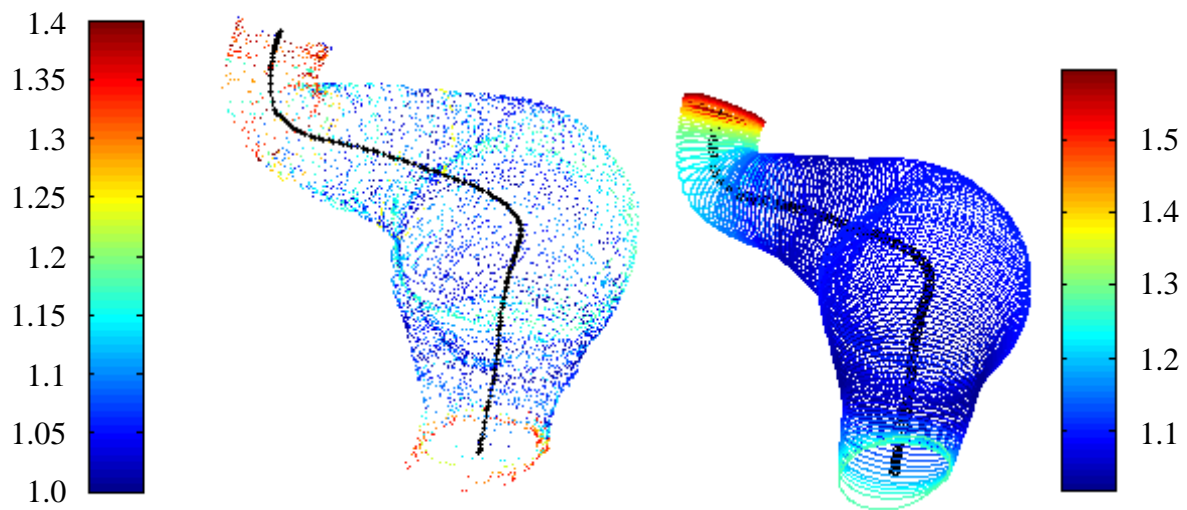


Figure 48. Eccentricity parameter values displayed for B2 lumen before surface approximation with a cutoff of 1.4 (left) and after surface approximation (right).

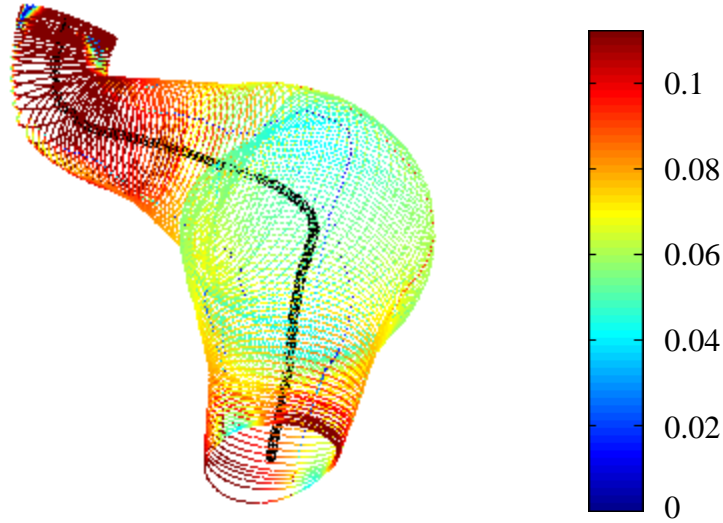


Figure 49. Curvature parameter values displayed for B2 lumen after surface approximation with a cutoff of mean + 1 standard deviation.

4.4 Discussion

4.4.1 Centerline Generation Algorithm

The centerline generation method yielded results comparable to those found using a trial of the MedCAD module within Mimics®, a commercial grade centerline generation code. Those results cannot be shown because access to them was lost when module access expired. The developed algorithm can handle complex paths, and the number of center points is easily adjustable. Estimation of an individual maximally inscribed sphere usually showed excellent convergence within 200 iterations. The centerline generation technique is automated, repeatable, and relatively insensitive to outward saccular growth. If a different file format than STL was used, preferably a meshed surface, the top and bottom vessel ends could be more easily excluded from the algorithm providing a small increase in data near each vessel end as well as rendering the method insensitive to vessel end surface orientations. It is important to smoothly approximate the centerline for the longitudinal plane acquisition method presented. Longitudinal

planes are defined normal the centerline, and even a slightly noisy centerline would yield inaccurate results.

It should be noted that other centerline generation algorithms have been developed for use with the carotid bifurcation which are based on maximally inscribed spheres, but the proposed method was developed independently [62–64]. The definition of a centerline is straightforward and unarguable for ideal geometries such as tubes, but as geometries become more complex the definition and method of acquiring the centerline becomes more obscure. For example, a maximally inscribed sphere method is insensitive to extreme saccular growth, whereas a transverse polyline centroid method would reflect every change in such a growth; protrusions of the surface inward cause a direct decrease of the size of a maximally inscribed sphere near that boundary, whereas protrusions outward have no effect. There is no answer as to which of these methods is *correct*, and instead the focus should be on which one yields more meaningful and justifiable results for the purpose of a given study. For example, in the proposed method the radius is more conservatively defined as the distance from the centerline; the distance from the centerline can be affected and interpreted in a number of unique ways. If the anterior side of the vessel expands and the posterior side remains stable, the distance from the centerline on each side would also increase, which is an important concept to be aware of. As a result the distance to the centerline can be a misleading parameter unless properly understood.

The initial guess for iteratively fitting a maximally inscribed sphere for a given cross-section also limits the final result. By enforcing a dependency on the previously generated points of the centerline for the generation of the next point, the overall path of the centerline can be

predicted and maintained in an intuitive way. However, this can lead to scenarios where slightly different inputs yield vastly different results. In order to fully automate centerline generation and render reliable and repeatable results more advanced measures must be developed. Such measures might involve multiple quick passes of centerline generations to accurately predict the most likely general course of the final centerline to generate using the detailed algorithm. An additional important consideration is how to accurately compare intra-patient results; each surface from a longitudinal study has a unique centerline, and therefore each parameterized surface is parameterized to a different centerline, so the difference in the surfaces are not directly related with the local change. Nevertheless, this geometric characterization may allow, to some degree, the separation of local expansion from global shifting (i.e., movement of the centerline) of the aneurysm shape. A shortcoming of the method presented here then stems from the fact that individual surface points cannot be individually tracked from one CT surface to the next except a few identifiable markers.

If two centerlines are generated from two scans for the same patient at different times they may have different degrees of tortuosity, not to mention aneurysm expansion. Both of these changes can lead to centerlines with longer total arc lengths, which makes translation of geometric changes through parameterization difficult. For instance, one surface may have 125 longitudinal planes, while the next may have 140 for the same region. The changes observed are also regionally based; the proximal or distal end of an aneurysm may see large changes while another may not, resulting in an uneven change of the spatial distribution of the interpreted longitudinal planes. Understanding these changes in such a way that their interpretation can be automated is vital to advancing the utility of longitudinal parameter estimation.

4.4.2 Parameterization and Surface Approximation

Another utility of surface parameterization is that various quantities at the aneurismal wall or on the surface, such as wall thickness, surface curvature, or wall stresses from biomechanical analyses, can be given as functions of two spatial parameters (s , θ) and time t . FEA, FSI, or computational fluid simulations could be done with a parameterized arterial surface mesh and the resulting data would represent both geometrical and mechanical values across the surface. This will allow future work to utilize techniques such as linear regression or Gaussian process learning to analyze the effect of various factors on aneurysm expansion and stress and to predict the time evolution. Many computational biosolid studies use idealized geometries, but when coupled with this automated surface parameterization, new possibilities emerge to analyze stress distribution or rupture risk over different geometries.

A major drawback of the proposed method is the reduction of the number of surface points. For example, the lumen surface of scan B2 before parameterization contains 17,247 points, while after parameterization it contains only 5,106 points. This reduction is due to the condition that a point must pass a particular inequality to be considered as a point lying on a given longitudinal plane. Alternatively the s parameter of a given surface point could be approximated by the minimum distance from the point to the centerline as done by Zeinali-Davarani et al. [60]. This method results in an s value for every point on the surface, but as the surface strays from an ideal cylinder complications arise to render this method imperfect as well.

There are significant drawbacks associated with the degree of reduction seen by the proposed method. If an FEA, FSI, or fluid simulation was performed and mechanical values are recorded for each point of the utilized surface mesh, then the reduction of points on the surface results in a direct loss of data. Less data renders statistical methods less powerful, especially with respect to surface approximation and correlation analyses. An advanced parameterization method which preserves every point on the surface and has the speed of the minimum-distance method as well as the robustness of the longitudinal plane method would be ideal. In order to accomplish this surface meshes would have to replace surface STLs as the input of choice. The information a connectivity matrix provides is invaluable for ensuring a reliable algorithm can be developed.

The surface approximation algorithm itself is quite robust, although some optimization is required for it to reach its full potential. A test case was run for every combination of the number of shape functions in each dimension to find an optimum pair. The quality of the result was based on minimizing the sum of the squared error of the residuals (SSE). The resulting values are first sorted by N_η and then N_θ for 100 cases to show the general trend of the resulting SSE values (Figure 50, Table C.1). The resulting values are then sorted by the SSE values themselves (Figure 51, Table C.2). The important conclusion is that the number shape functions in each dimension do not evenly contribute to improved accuracy, and that unique optimum combinations exist on a case by case basis between accuracy and computational time. One goal of surface approximation is to translate the surface data into a form suitable for rigorous statistical computations absent from biomechanical rationale to push the limits of what statistics alone can accomplish before reinforcing it with biomechanical rationale.

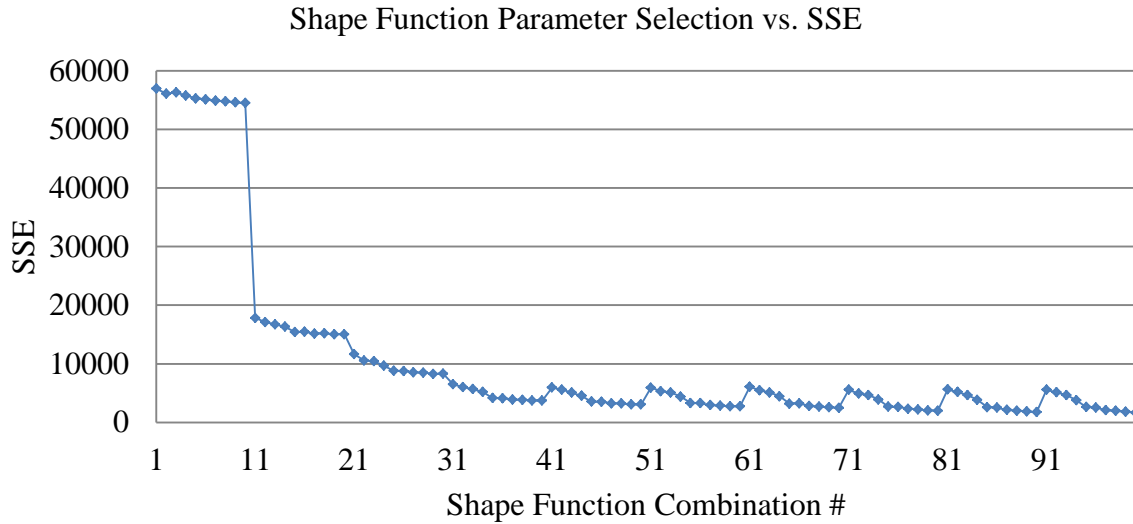


Figure 50. SSE values curve sorted by N_η and N_θ for 100 cases of shape function surface fitting.

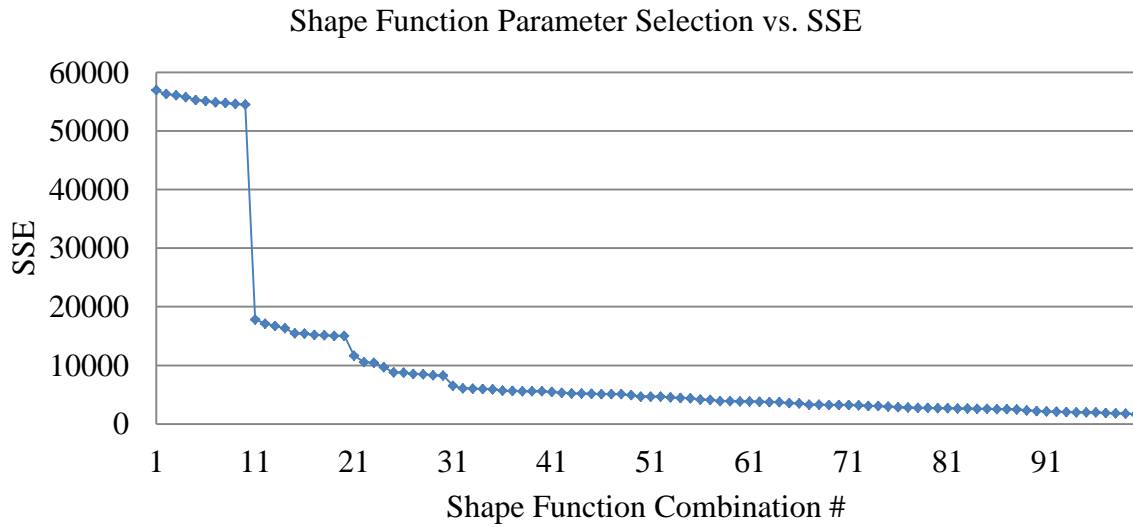


Figure 51. SSE values curved sorted by SSE value for 100 case of shape function surface fitting.

4.4.3 Morphological Parameters

The proposed methods for determining parameter values of eccentricity and polyline curvature are inadequate. The measure of eccentricity suffers from major drawbacks: there is no constraint that the major and minor axes intersect at the given cross-sections origin, the axes are

only approximately 90° from one another, the direction of the major axis is subject to surface irregularities, and there is no continuity of axes from one cross-section to the next. All of these problems stem from the fact that point-cloud data was used instead of surface data; by constraining the eccentricity/asymmetry axes to pre-defined unstructured points along the polyline of a cross-section there is no way to remedy the drawbacks listed. In order to properly define the eccentricity axes a more structured distribution of data for a given cross-section is required. If the pre-fit and post-fit values are compared numerically it is clear how the results are drastically improved with clear continuity of eccentricity trends across cross-sections for the ideally structured post-fit surface (Figure 52). The following conditions are able to be enforced for the post-fit surface that cannot be enforced for the pre-fit surface: the major and minor axes intersect at a given cross-section's origin, the axes are exactly 90° from one another, the surface is smooth rendering the direction of the major axis less influenced by surface irregularities, and there is a natural continuity and progression of eccentricity across cross-sections as a virtue of utilizing normal shape functions. The proposed method of eccentricity calculation is therefore only really meaningful when paired with the post-fit surface of a given AAA.

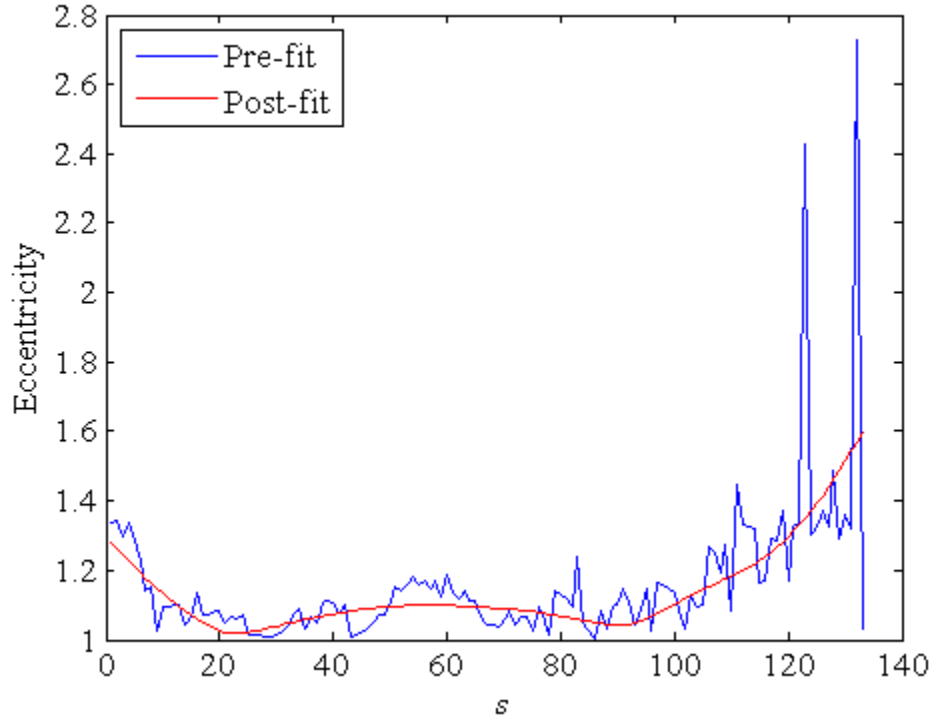


Figure 52. Eccentricity of the arterial lumen surface of B2 pre-fit (blue) and post-fit (red).

The second analyzed morphological parameter, the polyline curvature, is also limited in its interpretation. First and foremost a small revision to the method would eliminate the high-value stripes seen at $\theta = 0, \pi/2, \pi,$ and $3\pi/2$. After such a fix it must also be critically analyzed as to the best set of 3 points to use to determine the curvature of a given point. For the results shown a set of a given point and the points immediately neighboring it on either side are used for the curvature calculation. The selection of the additional points for the calculation affects results and should be considered very carefully. The results shown are for a post-fit approximated surface, which is mathematically smooth. The polyline curvature method yields nonsensical results for the pre-fit surface due to surface spikes and irregularities and no discernable trends

could be identified. The selection of curvature calculation points for the pre-fit data is extremely difficult to determine to yield meaningful results.

It is clear that both of the morphological parameters described are not easily obtained for pre-fit surfaces. Whether this highlights the importance of a proper approximation algorithm or the shortcomings of the methods themselves is hard to distinguish, but it is clear the results show more intuitively understood trends for post-fit surfaces. The post-fit surfaces are still approximations, however, so the results have to be presented with that caveat. It is believed that the surface approximation presented is worthwhile and actually enhances the readability and reliability of results for the methods proposed.

4.4.4 Future Work

The algorithms presented are not finalized and this study has many possibilities for expansion to serve as a useful tool for clinical management of AAAs or computational biomechanical studies. There exist many places to further automate and optimize the existing methods, but some methods presented may benefit from a total redesign. For example, it must be clarified that eccentricity and asymmetry are intertwined but distinctly different. Eccentricity is simply a measure of the skewedness of a given cross-section, but the asymmetry can be best analyzed by considering the directions of the major and minor axes utilized to calculate eccentricity. The currently proposed method is highly influenced by surface irregularities. Alternatives exist such as the principal axes method and calculating the second moment of inertia of a cross-section. These methods are not as heavily influenced by surface irregularities and carry a more two-dimensionally robust justification than simply identifying the maximum

diameter pair of points constrained to the origin of a cross-section. Likewise the polyline curvature method presented is simplistic and an increase in dimensionality would be ideal. Considering the 3-D curvature of the surface instead of polyline curvature constrained to individual planes would offer a more intuitive global understanding of the curvature across the aneurysm and provide a more robust solution for unique AAA surfaces.

Aside from the various improvements that could be done to the existing parameterization method proposed, a lot still must be done to fully bridge the gap between AAA pathology and biomechanics. The consideration of the interactions with surrounding tissues of AAAs will serve to enrich the biomechanical understanding of AAA pathology. Other biomechanical factors still exist of course; for example, it is not understood why different demographics such as women vs. men exhibit much different risk for AAA development. Ongoing studies have been examining the unique blood flow due to anatomical differences between men and women in the abdomen and suggest that hemodynamics may play a role in AAA development. Other studies have suggested that hormones in the body and bloodstream may contribute to AAA risk as well. At this point it is clear that not only do the engineering and medical communities need to cooperate but biochemistry, statistics, and biology experts should become involved to further the understanding of AAAs. The mechanical understanding and simulation of AAAs has reached a critical point that must be overcome. The logical next step for the research community is the widespread adoption of longitudinal datasets to understand the mechanical and geometrical evolution of AAAs over time considering mechanical, statistical, biological, and biochemical factors between AAAs and surrounding tissues.

APPENDICES

APPENDIX A

Detailed information and measurements of CT scan data

Table A.1. Detailed scan resolution information for the CT data set studied.

Scan	Pixel Size (mm)	# Slices	Slice increment (mm)	Slice thickness (mm)
A1	0.656	1003	var.	1.000
A2	0.645	618	var.	1.000
B1	0.680	931	var.	1.000
B2	0.678	951	0.699	1.000
B3	0.777	1073	var.	1.000
C1	0.688	961	var.	1.000
C2	0.684	684	1.000	1.000
D1	0.605	375	1.499	2.000
D2	0.635	596	1.000	1.250
D3	0.578	621	0.699	1.000
E1	0.617	863	0.699	1.000
E2	0.572	899	0.699	1.000
F1	0.477	124	2.000	3.000
F2	0.375	133	2.000	3.000
F3	0.510	441	1.249	1.250
F4	0.531	381	var.	3.200
F5	0.545	411	1.500	2.000
F6	0.539	730	0.699	1.000
F7	0.656	588	1.000	1.000
G1	0.783	2096	var.	1.000
G2	0.670	1020	0.699	1.000
G3	0.730	805	0.699	1.000
G4	0.639	510	1.000	1.000
G5	0.684	642	1.000	1.000
G6	0.633	463	var.	1.000
H1	0.494	249	var.	3.200
H2	0.547	409	var.	3.200
H3	0.723	693	var.	1.000
H4	0.678	666	0.699	1.000
H5	0.688	653	0.699	1.000
H6	0.652	640	0.699	1.000
H7	0.625	504	1.000	1.000
H8	0.703	505	1.000	1.000
H9	0.684	453	var.	1.000
I1	0.547	468	1.250	1.250
I2	0.625	653	1.000	1.250
I3	0.645	287	var.	3.200
I4	0.676	659	0.699	1.000
I5	0.549	443	1.000	1.000

Table A.1 (cont'd)

I6	0.582	608	0.699	1.000
J1	0.684	732	var.	1.000
J2	0.621	673	0.699	1.000
J3	0.658	650	var.	1.000
J4	0.650	456	1.000	1.000
J5	0.652	654	0.699	1.000
K1	0.742	926	0.699	1.000
K2	0.793	701	1.000	1.250
K3	0.637	717	var.	1.000
K4	0.660	995	0.699	1.000
K5	0.758	1086	0.699	1.000
K6	0.750	787	0.699	1.000

Table A.2. Detailed scanner manufacturers and models, date of scans, and total time elapsed from initial scanning.

Scan	Manufacturer	Model	Date	Elapsed
A1	SIEMENS	Definition	9/11/2009	0
A2	Philips	Brilliance 64	3/12/2010	0 y, 6 m, 1 d
B1	SIEMENS	Definition	10/30/2008	0
B2	SIEMENS	Definition	5/21/2009	0 y, 6 m, 21 d
B3	SIEMENS	SOMATOM Definition	11/2/2010	2 y, 0 m, 3 d
C1	SIEMENS	Definition	3/9/2009	0
C2	Philips	Brilliance 64	12/1/2010	1 y, 6 m, 22 d
D1	SIEMENS	Sensation 16	7/31/2004	0
D2	GE_MEDICAL_SYSTEMS	LightSpeed Ultra	12/7/2005	1 y, 4 m, 7 d
D3	SIEMENS	Definition	4/18/2008	3 y, 8 m, 18 d
E1	SIEMENS	Definition	4/4/2008	0
E2	SIEMENS	Definition	10/13/2008	0 y, 6 m, 9 d
F1	SIEMENS	SOMATOM PLUS 4	12/15/1999	0
F2	SIEMENS	SOMATOM PLUS 4	3/9/2001	1 y, 2 m, 22 d
F3	GE_MEDICAL_SYSTEMS	LightSpeed Ultra	12/2/2003	3 y, 11 m, 17 d
F4	Philips	Mx8000	2/24/2004	4 y, 2 m, 9 d
F5	SIEMENS	Sensation 16	8/17/2004	4 y, 8 m, 2 d
F6	SIEMENS	Sensation 16	12/2/2005	5 y, 11 m, 17 d
F7	Philips	Brilliance 64	3/6/2007	7 y, 2 m, 19 d
G1	SIEMENS	Sensation 16	4/20/2005	0
G2	SIEMENS	Sensation 16	10/13/2005	0 y, 5 m, 23 d
G3	SIEMENS	Sensation 16	4/13/2006	0 y, 11 m, 24 d
G4	Philips	Brilliance 64	10/9/2006	1 y, 5 m, 19 d
G5	Philips	Brilliance 64	4/4/2007	1 y, 11 m, 15 d
G6	Philips	Brilliance 64	10/11/2007	2 y, 5 m, 21 d
H1	Marcon	Mx8000	10/25/2001	0
H2	Philips	Mx8000	11/18/2002	1 y, 0 m, 24 d

Table A.2 (cont'd)

H3		SIEMENS	Sensation 16	7/28/2007	5 y, 9 m, 3 d
H4		SIEMENS	Definition	7/9/2008	6 y, 8 m, 14 d
H5		SIEMENS	Definition	6/29/2009	7 y, 8 m, 4 d
H6		SIEMENS	Sensation 16	6/16/2010	8 y, 7 m, 22 d
H7		Philips	Brilliance 64	12/2/2010	9 y, 1 m, 7 d
H8		Philips	Brilliance 64	3/9/2011	9 y, 4 m, 12 d
H9		Philips	Brilliance 64	3/19/2011	9 y, 4 m, 22 d
I1	GE_MEDICAL_SYSTEMS		LightSpeed Ultra	8/26/2003	0
I2	GE_MEDICAL_SYSTEMS		LightSpeed Ultra	9/3/2004	1 y, 0 m, 8 d
I3		Philips	Mx8000	9/9/2005	2 y, 0 m, 14 d
I4		SIEMENS	Sensation 16	8/4/2006	2 y, 11 m, 9 d
I5		Philips	Brilliance 64	8/3/2007	3 y, 11 m, 8 d
I6		SIEMENS	Definition	7/1/2009	5 y, 10 m, 5 d
J1		SIEMENS	Sensation 16	11/2/2006	0
J2		SIEMENS	Sensation 16	11/23/2007	1 y, 0 m, 21 d
J3		SIEMENS	Definition	11/28/2008	2 y, 0 m, 26 d
J4		Philips	Brilliance 64	11/27/2009	3 y, 0 m, 25 d
J5		SIEMENS	SOMATOM Definition	5/15/2010	3 y, 6 m, 13 d
K1		SIEMENS	Sensation 16	10/5/2005	0
K2	GE_MEDICAL_SYSTEMS		LightSpeed Ultra	5/20/2006	0 y, 7 m, 15 d
K3		N/A	N/A	8/10/2007	1 y, 10 m, 5 d
K4		N/A	N/A	8/19/2008	2 y, 10 m, 14 d
K5		N/A	N/A	8/8/2009	3 y, 10 m, 3 d
K6		N/A	N/A	12/1/2009	4 y, 1 m, 26 d

Table A.3. Tissue Measurements from individual patient CT scans.

		A	B	C	C (sac)	D	F	G	H	I	J	K
Scan 1	Time t	0	0	0	0	0	0	0	0	0	0	0
	D _{max}	57.31	46.21	41.11	31.82	52.02		45.03	44.85	31.68	40.20	42.22
	90° to D _{max}	50.43	44.21	39.53	29.82	49.59		40.42	40.81	29.81	39.29	42.18
Scan 2	Time t	182	203	632	632	494	450	176	389	374	386	227
	D _{max}	58.81	50.06	45.37	33.91	59.21	44.69	49.01	48.80	30.32	42.69	43.46
	90° to D _{max}	55.42	44.31	41.68	32.25	55.68	42.74	41.47	44.78	28.82	41.50	42.42
Scan 3	Time t		733			1357	1448	358	2102	745	757	674
	D _{max}		54.53			72.10	58.79	49.90	56.14	35.02	44.09	45.68
	90° to D _{max}		54.58			70.03	56.46	43.78	50.30	32.28	43.79	42.22
Scan 4	Time t						1532	537	2449	1074	1121	1049
	D _{max}						62.41	52.18	59.23	36.16	46.74	53.00
	90° to D _{max}						56.96	49.84	52.87	34.28	45.67	51.94
Scan 5	Time t						1707	714	2804	1438	1290	1403
	D _{max}						62.73	53.38	61.74	37.78	50.07	57.53
	90° to D _{max}						61.92	49.73	54.49	36.61	49.30	55.24
Scan 6	Time t						2179	904	3156	2136		
	D _{max}						69.11	58.08	67.28	41.63		
	90° to D _{max}						67.92	52.08	59.53	37.98		
Scan 7	Time t						2638		3325			
	D _{max}						73.10		69.20			
	90° to D _{max}						72.23		60.22			

Table A.4. Lumen Measurements from individual patient CT scans.

		A	B	C	C (sac)	D	F	G	H	I	J	K
Scan 1	Time t	0	0	0	0	0	0	0	0	0	0	0
	D _{max}	54.24	38.36	36.05	25.38	45.88		39.87	38.48	28.86	35.62	35.39
	90° to D _{max}	47.91	37.73	34.05	24.53	40.12		33.94	36.26	27.08	33.23	27.29
Scan 2	Time t	182	203	632	632	494	450	176	389	374	386	227
	D _{max}	56.99	44.40	39.80	29.51	50.85	40.81	40.80	40.81	30.32	35.27	38.98
	90° to D _{max}	52.46	39.65	38.40	26.05	32.29	39.33	37.03	39.92	28.82	33.78	28.74
Scan 3	Time t		733			1357	1448	358	2102	745	757	674
	D _{max}		52.37			64.69	48.48	43.72	40.77	32.14	37.65	38.32
	90° to D _{max}		49.34			45.40	36.43	38.52	31.90	28.80	33.04	30.27
Scan 4	Time t						1532	537	2449	1074	1121	1049
	D _{max}						49.09	47.54	33.97	33.67	37.92	41.24
	90° to D _{max}						37.52	43.80	28.05	32.17	36.05	28.91
Scan 5	Time t						1707	714	2804	1438	1290	1403
	D _{max}						49.58	50.22	38.58	35.12	41.01	39.94
	90° to D _{max}						39.56	45.25	31.64	33.47	39.54	29.32
Scan 6	Time t						2179	904	3156	2136		
	D _{max}						44.17	51.20	41.18	37.55		
	90° to D _{max}						39.96	43.95	34.22	34.54		
Scan 7	Time t						2638		3325			
	D _{max}						48.89		45.30			
	90° to D _{max}						40.76		36.35			

APPENDIX B

MatLab code developed for automatic parameterization of AAAs

Appendix B.1. step_0.m, part of the Matlab code written to generate the centerlines

```
clear all; close all; clc;
```

```
a = dir('*.*txt');
```

```
global A B i Xs Xstan s N1 N2 N3 perp2 meanR radius circ theta C D num_data
```

```
for i = 1:length(a)
```

```
    A{i,1} = load(a(i).name); A{i,2} = a(i).name(1:2); A{i,3} = a(i).name(4);  
    B{i,2} = A{i,2}; B{i,3} = A{i,3};
```

```
end
```

```
for i = 1:length(a)
```

```
    step_1;  
%    step_2;  
    %    step_3;  
    %    step_4;  
    %    step_5;  
    %    step_6;
```

```
end
```

Appendix B.2. step_1, the core functionality of the centerline generation algorithm

```
%% script for the centerline generation
```

```
min_z = min(A{i,1}(:,3));
```

```
max_z = max(A{i,1}(:,3));
```

```
k = 0;
```

```
for j = 1:length(A{i,1})
```

```
    if A{i,1}(j,3) > (min_z + 2.5) && A{i,1}(j,3) < (max_z - 2.5)
```

```
        k = k + 1;
```

```
        A_temp(k,1) = A{i,1}(j,1); A_temp(k,2) = A{i,1}(j,2); A_temp(k,3) = A{i,1}(j,3);
```

```
    end
```

```
end
```

```
A{i,1} = A_temp;
```

```
itenum = 250;
```

```
S_n = 2;
```

```
min_z = min(A{i,1}(:,3)); max_z = max(A{i,1}(:,3));
```

```
S = 0;
```

```
S_chk = max_z - 1;
```

```
while S_chk < max_z
```

```
    S = S + 1;
```

```
    htext = sprintf(['Calculating Center Point for s = ', num2str(S), ' ...']);
```

```
    clear A2 d CoT k; k = 0;
```

```
    if S == 1
```

```
        for l = 1:length(A{i,1});
```

```
            if A{i,1}(l,3) >= min_z && A{i,1}(l,3) <= min_z + 1
```

```
                k = k+1;
```

```
                A2(k,:) = A{i,1}(l,:);
```

```
            end
```

```
        end
```

Appendix B.2 (cont'd)

```
B{i,1}(S,1) = sum(A2(:,1))/length(A2); B{i,1}(S,2) = sum(A2(:,2))/length(A2); B{i,1}(S,3)
= min_z;
```

```
elseif S == 2
```

```
B{i,1}(S,1) = B{i,1}(S-1,1); B{i,1}(S,2) = B{i,1}(S-1,2); B{i,1}(S,3) = B{i,1}(S-1,3) +
S_n;
```

```
else
```

```
PQ_S1 = [B{i,1}(S-1,1)-B{i,1}(S-2,1), B{i,1}(S-1,2)-B{i,1}(S-2,2), B{i,1}(S-1,3)-
B{i,1}(S-2,3)];
```

```
PQ_S2 = sqrt((B{i,1}(S-1,1)-B{i,1}(S-2,1))^2 + (B{i,1}(S-1,2)-B{i,1}(S-2,2))^2 +
(B{i,1}(S-1,3)-B{i,1}(S-2,3))^2);
```

```
PQ_S = PQ_S1 / PQ_S2;
```

```
B{i,1}(S,1) = B{i,1}(S-1,1) + S_n*PQ_S(1); B{i,1}(S,2) = B{i,1}(S-1,2) + S_n*PQ_S(2);
B{i,1}(S,3) = B{i,1}(S-1,3) + S_n*PQ_S(3);
```

```
end
```

```
itesize(S) = 1;
```

```
h = waitbar(0,htext);
```

```
for j = 1:itenum
```

```
for k = 1:length(A{i,1})
```

```
d(k) = sqrt((A{i,1}(k,1)-B{i,1}(S,1))^2 + (A{i,1}(k,2)-B{i,1}(S,2))^2 + (A{i,1}(k,3)-
B{i,1}(S,3))^2);
```

```
end
```

```
[d_X,d_Y] = min(d);
```

```
[X,Y,Z] = sphere(20); %Makes a dummy unit sphere
```

```
X = d_X*X; Y = d_X*Y; Z = d_X*Z; %Makes the unit sphere have radius = minimum
distance above
```

```
X = X + B{i,1}(S,1); %Moves the sphere's center to the centroid
```

```
Y = Y + B{i,1}(S,2);
```

```
Z = Z + B{i,1}(S,3);
```

```
PQ_1 = [A{i,1}(d_Y,1)-B{i,1}(S,1), A{i,1}(d_Y,2)-B{i,1}(S,2), A{i,1}(d_Y,3)-B{i,1}(S,3)];
```

Appendix B.2 (cont'd)

```
PQ_2 = sqrt((A{i,1}(d_Y,1)-B{i,1}(S,1))^2 + (A{i,1}(d_Y,2)-B{i,1}(S,2))^2 +
(A{i,1}(d_Y,3)-B{i,1}(S,3))^2);
```

```
PQ = PQ_1 / PQ_2;
```

```
if S==1
    B{i,1}(S,1) = B{i,1}(S,1) - PQ(1)*itesize(S); B{i,1}(S,2) = B{i,1}(S,2) -
PQ(2)*itesize(S);
elseif S==2
    B{i,1}(S,1) = B{i,1}(S,1) - PQ(1)*itesize(S); B{i,1}(S,2) = B{i,1}(S,2) -
PQ(2)*itesize(S);
else
    proj_PQ = cross(PQ_S,(cross(PQ,PQ_S)/norm(PQ_S)))/norm(PQ_S);
    proj_PQ = proj_PQ /norm(proj_PQ);
    B{i,1}(S,:) = B{i,1}(S,:) - proj_PQ*itesize(S);
end

x_c2(j,S) = B{i,1}(S,1); y_c2(j,S) = B{i,1}(S,2); z_c2(j,S) = B{i,1}(S,3);
d2(j,S) = d_X;

if j >= 15
    CoT(j-14,S) = sqrt((x_c2(j,S)-x_c2(j-14,S))^2 + ((y_c2(j,S)-y_c2(j-14,S))^2));

    if CoT(j-14,S) < itesize(S)
        itesize(S) = itesize(S) / 2;
    end

end

%           if j==1
%
figure;scatter3(A{i,1}(:,1),A{i,1}(:,2),A{i,1}(:,3),1,'CData',A{i,1}(:,3),'marker','.'); hold on
%Plots the AAA colorfully
%           plot3(B{i,1}(S,1),B{i,1}(S,2),B{i,1}(S,3),'g.','Markersize',15); %Plots the
centroid as a green dot
%           title(A(i,2));xlabel('x direction (mm)');ylabel('y direction (mm)');zlabel('z
direction (mm)');axis image %labels the graph
%           hold
on;plot3(A{i,1}(d_Y,1),A{i,1}(d_Y,2),A{i,1}(d_Y,3),'b.','Markersize',20) %Marks the
minimum distance point with a blue dot
%           plot3(X,Y,Z,'ro');axis image %Shows the sphere before any iterations
    if S~=1 && S ~= 2 && j==itenum
        figure;scatter3(A{i,1}(:,1),A{i,1}(:,2),A{i,1}(:,3),1,'CData',A{i,1}(:,3),'marker','.');
hold on %Plots the AAA colorfully
```

Appendix B.2 (cont'd)

```

        plot3(B{i,1}(S,1),B{i,1}(S,2),B{i,1}(S,3),'g.','Markersize',15); %Plots the centroid
as a green dot

        title(A(i,2));xlabel('x direction (mm)');ylabel('y direction (mm)');zlabel('z direction
(mm)');axis image %labels the graph
        hold on;plot3(A{i,1}(d_Y,1),A{i,1}(d_Y,2),A{i,1}(d_Y,3),'b.','Markersize',20)
%Marks the minimum distance point with a blue dot
        plot3(X,Y,Z,'ro');axis image %Shows the sphere after all iterations
figure;
        plot3(B{i,1}(S,1),B{i,1}(S,2),B{i,1}(S,3),'g.','Markersize',15); %Plots the centroid
as a green dot
        title(A(i,2));xlabel('x direction (mm)');ylabel('y direction (mm)');zlabel('z direction
(mm)');axis image %labels the graph
        hold on;plot3(A{i,1}(d_Y,1),A{i,1}(d_Y,2),A{i,1}(d_Y,3),'b.','Markersize',20)
%Marks the minimum distance point with a blue dot
        scatter3(X(:),Y(:),Z(:),'Cdata',Z(:),'marker','.');axis image %Shows the sphere after
all iterations

plot3([B{i,1}(S,1),B{i,1}(S,1)+proj_PQ(1)*d_X],[B{i,1}(S,2),B{i,1}(S,2)+proj_PQ(2)*d_X],[B
{i,1}(S,3),B{i,1}(S,3)+proj_PQ(3)*d_X],'r','Markersize',15); %graphs projection vector

plot3([B{i,1}(S,1),B{i,1}(S,1)+PQ(1)*d_X],[B{i,1}(S,2),B{i,1}(S,2)+PQ(2)*d_X],[B{i,1}(S,3),
B{i,1}(S,3)+PQ(3)*d_X],'b','Markersize',15); %graphs min_dist vector

plot3([B{i,1}(S,1),B{i,1}(S,1)+PQ_S(1)*d_X],[B{i,1}(S,2),B{i,1}(S,2)+PQ_S(2)*d_X],[B{i,1}
(S,3),B{i,1}(S,3)+PQ_S(3)*d_X],'k','Markersize',15); %graphs normal vector
    end

        waitbar(j / itenum,h,htext)

        S_chk = B{i,1}(S,3);

    end
    delete(h)
end

disp(['Refining Final S value: ',num2str(S),' ...'])

clear d d_X d_Y CoT h htext

B{i,1}(S,1) = B{i,1}(S-1,1) + S_n*PQ_S(1);
B{i,1}(S,2) = B{i,1}(S-1,2) + S_n*PQ_S(2);
B{i,1}(S,3) = max_z;

```

Appendix B.2 (cont'd)

```
itesize(S) = 1;
```

```
for j = 1:itenum
```

```
Appendix 6 (cont'd)
```

```
for k = 1:length(A{i,1})
```

```
    d(k) = sqrt((A{i,1}(k,1)-B{i,1}(S,1))^2 + (A{i,1}(k,2)-B{i,1}(S,2))^2 + (A{i,1}(k,3)-  
B{i,1}(S,3))^2);
```

```
end
```

```
[d_X,d_Y] = min(d);
```

```
PQ_1 = [A{i,1}(d_Y,1)-B{i,1}(S,1), A{i,1}(d_Y,2)-B{i,1}(S,2), A{i,1}(d_Y,3)-B{i,1}(S,3)];
```

```
PQ_2 = sqrt((A{i,1}(d_Y,1)-B{i,1}(S,1))^2 + (A{i,1}(d_Y,2)-B{i,1}(S,2))^2 +  
(A{i,1}(d_Y,3)-B{i,1}(S,3))^2);
```

```
PQ = PQ_1 / PQ_2;
```

```
B{i,1}(S,1) = B{i,1}(S,1) - PQ(1)*itesize(S); B{i,1}(S,2) = B{i,1}(S,2) - PQ(2)*itesize(S);
```

```
x_c2(j,S) = B{i,1}(S,1); y_c2(j,S) = B{i,1}(S,2); z_c2(j,S) = B{i,1}(S,3);
```

```
d2(j,S) = d_X;
```

```
if j >= 15
```

```
    CoT(j-14,S) = sqrt((x_c2(j,S)-x_c2(j-14,S))^2 + ((y_c2(j,S)-y_c2(j-14,S))^2));
```

```
    if CoT(j-14,S) < itesize(S)
```

```
        itesize(S) = itesize(S) / 2;
```

```
    end
```

```
end
```

```
disp(['S value: ',num2str(S),' ... '])
```

```
disp(['Iteration #: ',num2str(j),' / ',num2str(itenum)])
```

```
end
```

```
figure;scatter3(A{i,1}(:,1),A{i,1}(:,2),A{i,1}(:,3),1,'CDData',A{i,1}(:,3),'marker','.');
```

```
hold on; axis image;
```

```
scatter3(B{i,1}(:,1),B{i,1}(:,2),B{i,1}(:,3));
```

```
plot3(B{i,1}(:,1),B{i,1}(:,2),B{i,1}(:,3));
```

```
clear A_temp CoT PQ proj_PQ PQ_1 PQ_2 PQ_S PQ_S1 PQ_S2 S S_chk _n X Y Z d d2 d_X  
d_Y itenum itesize j k l max_z min_z x_c2 y_c2 z_c2
```

Appendix B.3. step_2.m of the centerline generation algorithm This step generates smooth points along the centerline by an approximation function

```
X = B{i,1}';
```

```
Lbp=zeros(1,length(X)-1); %Length between points: calculates distance between each point.
Lbp(1)=distance between X(1) and X(2), etc.
```

```
for j=1:(length(X)-1)
    Lbp(j)=(((X(1,(j+1))-X(1,j))^2)+((X(2,(j+1))-X(2,j))^2)+((X(3,(j+1))-X(3,j))^2))^(1/2);
end
```

```
B{i,4} = sum(Lbp); % Length of the centerline X or B{i,1 }
```

```
l=zeros(1,length(X)); %the distance along the centerline at each point. l(1) is the distance from
X(:,1) to X(:,1). l(2) is the distance from X(:,1) to X(:,2), etc.
```

```
for j=1:length(Lbp)
    l(j+1)=sum(Lbp(1:j));
end
```

```
phi=zeros(1,(length(l)));%a group of base functions that depend on s. Use phis functions to fit a
centerline.
```

```
dphi_ds=zeros(1,length(l)); %derivative of phis with respect to s. Used to find tangent vectors at
each s for use as a reference vector later.
```

```
Xsarray=zeros(1,length(X),3); %contains the x,y,z elements that need to be summed to create
Xs. It is the result of X.*nphis (nphis is a normalization of the phis variable).
```

```
Xstanarray=zeros(1,length(X),3); %contains the x,y,z elements of X.*dnphidss.
```

```
s=l(1):1:l(end); %longitudinal distance along the centerline
```

```
Xs=zeros(1,length(s),3); %function of s that defines the coordiantes of the centerline at any s. It
is a smooth 4th order approximation function of the centerline.
```

```
Xstan=zeros(1,length(s),3); %contains the x,y,z coordinates that, at each s, will create a vector
from the origin to the aforementioned coordinates parrallel to the tangent vector at that s.
```

```
j = length(l);
```

```
for k=1:length(s)
```

```
    for m=1:j
```

```
        if m == 1
```

```
            if ( s(k) >= l(1) ) && ( s(k) <= l(3) )
```

```
                phi(m) = (s(k)-l(3))^2*(s(k)+l(3))^2/((l(1)-l(3))^2*(l(1)+l(3))^2);
```

```
                dphi_ds(m) = (2*(s(k)-l(3))*(s(k)+l(3))^2+2*(s(k)-l(3))^2*(s(k)+l(3)))/((l(1)-
l(3))^2*(l(1)+l(3))^2);
```

```
            else
```

```
                phi(m) = 0.0;
```

```
                dphi_ds(m)=0.0;
```

```
            end
```


Appendix B.3 (cont'd)

```

elseif m == 2
    if ( s(k) >= l(1) ) && ( s(k) <= l(4) )
        phi(m) = (s(k)+l(2))^2*(s(k)-l(4))^2/((l(2)+l(2))^2*(l(2)-l(4))^2);
        dphi_ds(m) = (2*(s(k)+l(2))*(s(k)-l(4))^2+2*(s(k)+l(2))^2*(s(k)-
l(4)))/((l(2)+l(2))^2*(l(2)-l(4))^2);
    else
        phi(m) = 0.0;
        dphi_ds(m)=0.0;
    end
elseif m == j-1
    if ( s(k) >= l(j-3) ) && ( s(k) <= l(j) )
        phi(m) = (s(k)-l(j-3))^2*(s(k)-2*l(j)+l(j-1))^2/((l(j-1)-l(j-3))^2*(l(j-1)-l(j))^2);
        dphi_ds(m) = (2*(s(k)-l(j-3))*(s(k)-2*l(j)+l(j-1))^2+2*(s(k)-l(j-3))^2*(s(k)-2*l(j)+l(j-
1)))/((l(j-1)-l(j-3))^2*(l(j-1)-l(j))^2);
    else
        phi(m) = 0.0;
        dphi_ds(m)=0.0;
    end
elseif m == j
    if ( s(k) >= l(j-2) ) && ( s(k) <= l(j) )
        phi(m) = (s(k)-l(j-2))^2*(s(k)-2*l(j)+l(j-2))^2/((l(j)-l(j-2))^4);
        dphi_ds(m) = (2*(s(k)-l(j-2))*(s(k)-2*l(j)+l(j-2))^2+2*(s(k)-l(j-2))^2*(s(k)-2*l(j)+l(j-
2)))/((l(j)-l(j-2))^4);
    else
        phi(m) = 0.0;
        dphi_ds(m)=0.0;
    end
else
    if ( s(k) >= l(m-2) ) && ( s(k) <= l(m+2) )
        phi(m) = (s(k)-l(m-2))^2*(s(k)-l(m+2))^2/((l(m)-l(m-2))^2*(l(m)-l(m+2))^2);
        dphi_ds(m) = (2*(s(k)-l(m-2))*(s(k)-l(m+2))^2+2*(s(k)-l(m-2))^2*(s(k)-
l(m+2)))/((l(m)-l(m-2))^2*(l(m)-l(m+2))^2);
    else
        phi(m) = 0.0;
        dphi_ds(m)=0.0;
    end

end
end

n_phi=phi/(sum(phi)); %Normalize
n_dphi_ds=((dphi_ds*sum(phi))-(phi*sum(dphi_ds)))/(sum(phi)^2); %normalize

for m=1:j

```

Appendix B.3 (cont'd)

```
    for n=1:3
        Xsarray(1,m,n)=X(n,m)*n_phi(m);
        Xstanarray(1,m,n)=X(n,m)*n_dphi_ds(m);
    end
end

for n=1:3
    Xs(1,k,n)=sum(Xsarray(1,:,n));
    Xstan(1,k,n)=sum(Xstanarray(1,:,n));
end
end

for j=1:(length(Xs)-1)
    Lbp2(j)=(((Xs(1,(j+1),1)-Xs(1,j,1))^2)+((Xs(1,(j+1),2)-Xs(1,j,2))^2)+((Xs(1,(j+1),3)-
Xs(1,j,3))^2))^(1/2);
end

Lbp3 = (((Xs(1,length(Xs),1)-Xs(1,1,1))^2)+((Xs(1,length(Xs),2)-
Xs(1,1,2))^2)+((Xs(1,length(Xs),3)-Xs(1,1,3))^2))^(1/2);

tort(i) = sum(Lbp2(:)) / Lbp3;

figure('Color',[1 1
1]);scatter3(A{i,1}(:,1),A{i,1}(:,2),A{i,1}(:,3),1,'CDData',A{i,1}(:,3),'marker','.');
hold on;
% scatter3(B{i,1}(:,1),B{i,1}(:,2),B{i,1}(:,3));
% plot3(B{i,1}(:,1),B{i,1}(:,2),B{i,1}(:,3));
plot3(Xs(:,1),Xs(:,2),Xs(:,3),'k','LineWidth',2);
tort_string = sprintf('Tortuosity = %f',tort(i));
title(tort_string);
axis image;

B{i,5}(:,:) = Xs(1,:);

clear j k l m n Lbp Lbp2 Lbp3 dphi_ds n_dphi_ds n_phi phi
```

Appendix B.4. step_3.m, the section of the Matlab code which calculates the normal vectors

```
%% Find N1, N2, N3 and perpendicular vector planes at each point s along the centerline.
```

```
%% Normal to centerline basis
```

```
%N2: is a unit vector that is a projection of the x axis unit vector perpendicular to vector N1.
```

```
%N3: is a unit vector that is the result of the cross product of N1 X N2.
```

```
N1=zeros(1,length(s),3); %Xstan vectors as unit vectors: the unit tangent vector at each s along the centerline approximation.
```

```
for j=1:length(Xstan)
```

```
    for k=1:3
```

```
        N1(1,j,k)= Xstan(1,j,k)/(sqrt((Xstan(1,j,1)^2)+(Xstan(1,j,2)^2)+(Xstan(1,j,3)^2)));
```

```
    end
```

```
end
```

```
graphN1=zeros(1,2,3); % A vector from the nth point along s, to the coordinates of the N1 vector added to the nth point along s.
```

```
figure;
```

```
for j=1:length(Xs)
```

```
    for k=1:3
```

```
        graphN1(1,.,k)=[Xs(1,j,k),(Xs(1,j,k)+N1(1,j,k))];
```

```
    end
```

```
    plot3(graphN1(1,.,1),graphN1(1,.,2),graphN1(1,.,3),'r');
```

```
    hold on
```

```
end
```

```
%% N2 Calculations: the projection of the x axis onto the perpendicular plane at point s along the centerline
```

```
k=zeros(1,2,3); %serves as a unit vector in the x direction.
```

```
k(1,2,1)=1;
```

```
N2_num = zeros(1,length(N1),3); %the numerator of the equation to compute N2
```

```
N2_den = zeros(1,length(N1)); %the denominator of the equation needed to compute N2
```

```
N2=zeros(1,length(N1),3);
```

```
for j=1:length(N1) %This for loop calculates N2 for each s
```

```
    for m=1:3
```

```
        N2_num(1,j,m)=(k(1,2,m)-
```

```
(((k(1,2,1)*N1(1,j,1))+k(1,2,2)*N1(1,j,2))+k(1,2,3)*N1(1,j,3))*N1(1,j,m));
```

Appendix B.4 (cont'd)

```
end

N2_den(j)=sqrt((N2_num(1,j,1)^2)+(N2_num(1,j,2)^2)+(N2_num(1,j,3)^2));

for m=1:3
    N2(1,j,m)=N2_num(1,j,m)/N2_den(j);
end
end

for j=length(N2) %makes N2 vectors into unit vectors
    N2_den(j)=sqrt((N2(1,j,1)^2)+(N2(1,j,2)^2)+(N2(1,j,3)^2));
    for m=1:3
        N2(1,j,m)=N2(1,j,m)/N2_den(j);
    end
end

for j=1:length(Xs) %Graphs each N2 at it's respective s
    for m=1:3
        graphN2(1,:,m)=[Xs(1,j,m),(Xs(1,j,m)+N2(1,j,m))];
    end
    plot3(graphN2(1,:,1),graphN2(1,:,2),graphN2(1,:,3),'b')
end

%% N3 Calculations

N3=zeros(1,length(N2),3); %the result of the cross product between N1 and N2

for j=1:length(N2) %calculates N3
    N3(1,j,1)=(N1(1,j,2)*N2(1,j,3))-(N1(1,j,3)*N2(1,j,2));
    N3(1,j,2)=-((N1(1,j,1)*N2(1,j,3))-(N1(1,j,3)*N2(1,j,1)));
    N3(1,j,3)=(N1(1,j,1)*N2(1,j,2))-(N1(1,j,2)*N2(1,j,1));
end

for j=1:length(Xs) %graphs N3 at it's respective s
    for m=1:3
        graphN3(1,:,m)=[Xs(1,j,m),(Xs(1,j,m)+N3(1,j,m))];
    end
    plot3(graphN3(1,:,1),graphN3(1,:,2),graphN3(1,:,3),'g')
end

%Manipulates and labels the first figure properly.
grid on
axis image
title('Approximated Centerline with N1, N2, and N3 Vectors at each point s','fontsize',12)
```

Appendix B.4 (cont'd)

```
xlabel('X direction (mm)')
ylabel('Y direction (mm)')
zlabel('Z direction (mm)')
```

```
%% Perpendicular vector determination
```

```
perp=zeros(length(A{i,1}),length(s),3); %a structured array that contains x,y,z coordinates of
perpendicular vectors going from a designated s to a known point on the surface
```

```
for j=1:length(N1) %Performs the dot product between the tangent vector at each s with the
vector going from that point s to each known surface point to determine where the dot product is
close to zero. This indicates the vectors are perpendicular and the information for that vector is
stored in perp.
```

```
    for m=1:length(A{i,1})
        k=[A{i,1}(m,1)-Xs(1,j,1), A{i,1}(m,2)-Xs(1,j,2),A{i,1}(m,3)-Xs(1,j,3)];
        if norm(k(3))<15
            dotprod=(N1(1,j,1)*k(1))+(N1(1,j,2)*k(2))+(N1(1,j,3)*k(3));
            h=norm(k);
            if dotprod/h<.01 && dotprod/h>-.01
                for n=1:3
                    perp(m,j,n)=A{i,1}(m,n)-Xs(1,j,n);
                end
            end
        end
    end
end
end
```

```
for j=1:length(s) %Eliminates all of the dot products that did not result in perpendicular vectors
to vastly decrease the size of the perp vector and store it as perp2
```

```
    k=0;
    for m=1:length(A{i,1})
        if perp(m,j,:)~=0
            k=k+1;
            for n=1:3
                perp2(k,j,n)=perp(m,j,n);
            end
        else
            end
    end
end
```

```
k=size(perp2);
```

```
figure
```

Appendix B.4 (cont'd)

for m=1:k(1)%Graphs the perpendicular perp2 vectors at their respective s

```
for j=1:k(2)
    if perp2(m,j,1)==0 && perp2(m,j,2)==0 && perp2(m,j,3)==0
    else
        for n=1:3
            graphperp(:,n)=[Xs(1,j,n),(Xs(1,j,n)+perp2(m,j,n))];
        end
        plot3(graphperp(:,1),graphperp(:,2),graphperp(:,3),'g')
        hold on
    end
end
end
```

axis image

%% Radii Checks

radius=zeros(k(1),k(2)); %the magnitude or radius of a given perp2 vector at a given s

for m=1:k(2) %This for loop finds the magnitude, or radius, of each particular perpendicular vector

```
for j=1:k(1)
    radius(j,m)=sqrt((perp2(j,m,1)^2)+(perp2(j,m,2)^2)+(perp2(j,m,3)^2));
end
end
```

% radius_script

```
for m=1:k(2)
    for j=1:k(1)
        if radius(j,m)==0
            radius(j,m)=NaN;
        end
    end
end
```

for j=1:k(2) %check of radius irregularities

```
for m=1:k(1)
    if radius(m,j)>(min(radius(:,j))+5)
        perp2(m,j,:)=0;
    end
end
```

Appendix B.4 (cont'd)

```
end
```

```
clear radius
```

```
for m=1:k(2)
    for j=1:k(1)
        radius(j,m)=sqrt((perp2(j,m,1)^2)+(perp2(j,m,2)^2)+(perp2(j,m,3)^2));
    end
end
```

```
meanR=zeros(1,length(s)); %the mean radius at a given s
```

```
k=size(perp2);
for m=1:length(s)% Finds the mean radius at each s
    h=0;
    for j=1:k(1)
        if radius(j,m)~=0
            h=h+1;
        end
    end
    meanR(m)=sum(radius(:,m))/h;
end
```

```
maxR_all(i) = max(meanR(:));
```

```
figure;
```

```
for m=1:k(1)%Graphs the perpendicular perp2 vectors at their respective s
    for j=1:k(2)
        if perp2(m,j,1)==0 && perp2(m,j,2)==0 && perp2(m,j,3)==0
            else
                graphperp(:,,1)=[Xs(1,j,1),(Xs(1,j,1)+perp2(m,j,1))];
                graphperp(:,,2)=[Xs(1,j,2),(Xs(1,j,2)+perp2(m,j,2))];
                graphperp(:,,3)=[Xs(1,j,3),(Xs(1,j,3)+perp2(m,j,3))];
                plot3(graphperp(:,,1),graphperp(:,,2),graphperp(:,,3),'g')
                hold on
            end
        end
    end
end
```

```
l=0;
```

```
for m=1:k(1)%Graphs the perpendicular perp2 vector endpoints at their respective s
    for j=1:k(2)
```

Appendix B.4 (cont'd)

```
if perp2(m,j,1)==0 && perp2(m,j,2)==0 && perp2(m,j,3)==0
else
    l=l+1;
    raw_str(1,1,i)=(Xs(1,j,1)+perp2(m,j,1));
    raw_str(1,2,i)=(Xs(1,j,2)+perp2(m,j,2));
    raw_str(1,3,i)=(Xs(1,j,3)+perp2(m,j,3));
    hold on
end
end
end

figure; subplot(1,2,1)
plot3(Xs(1,:,1),Xs(1,:,2),Xs(1,:,3),'k');
hold on;
scatter3(Xs(1,:,1),Xs(1,:,2),Xs(1,:,3),5,'k');
scatter3(A{i,1}(:,1),A{i,1}(:,2),A{i,1}(:,3),1,'CData',A{i,1}(:,3),'marker','!');
title('Raw (x,y,z) data');axis image;hold off;
subplot(1,2,2)
plot3(Xs(1,:,1),Xs(1,:,2),Xs(1,:,3),'k');
hold on;
scatter3(Xs(1,:,1),Xs(1,:,2),Xs(1,:,3),5,'k');
scatter3(raw_str(:,1,i),raw_str(:,2,i),raw_str(:,3,i),1,'CData',raw_str(:,3,i),'marker','!')
title('s Normal Plane (x,y,z) data');axis image; hold off;

clear N2_den N2_num dotprod graphN1 graphN2 graphN3 graphperp h j k l m n perp raw_str
```


Appendix B.5. step_4.m of the developed centerline generation algorithm

```
%% Find the magnitude of each individual perpendicular vector at a given s, and plot the mean radius with respect to s.
```

```
theta=0:pi/20:(2*pi); %contains the vector with angle values for the parametric computation of the circles
```

```
circ=zeros(1,length(theta),3); %contains information on the mean radius and orientation of the plane at a particular s so that a circle can be plotted to approximate the surface.
```

```
figure;
```

```
for j=1:length(meanR) %Plots circles of uniform radii corresponding to the radius at the particular perpendicular point.
```

```
    for m=1:length(theta)
```

```
        circ(1,m,1)=(meanR(j)*cos(theta(m))*N2(1,j,1))+(meanR(j)*sin(theta(m))*((N1(1,j,2)*N2(1,j,3))-N1(1,j,3)*N2(1,j,2)))+Xs(1,j,1);
```

```
        circ(1,m,2)=(meanR(j)*cos(theta(m))*N2(1,j,2)-meanR(j)*sin(theta(m))*((N1(1,j,1)*N2(1,j,3))-N1(1,j,3)*N2(1,j,1)))+Xs(1,j,2);
```

```
        circ(1,m,3)=(meanR(j)*cos(theta(m))*N2(1,j,3))+(meanR(j)*sin(theta(m))*((N1(1,j,1)*N2(1,j,2))-N1(1,j,2)*N2(1,j,1)))+Xs(1,j,3);
```

```
    end
```

```
    plot3(circ(1,:,1)',circ(1,:,2)',circ(1,:,3)')
```

```
    hold on
```

```
end
```

```
%Manipulates and labels the second figure properly.
```

```
axis image
```

```
grid on
```

```
title('Representation of Surface with Perpendicular Cross-sections A1','fontsize',12)
```

```
xlabel('X direction (mm)')
```

```
ylabel('Y direction (mm)')
```

```
zlabel('Z direction (mm)')
```

```
%Graphs the mean radius with respect to distance s along the centerline.
```

```
figure
```

```
plot(meanR,s)
```

```
%Manipulates and labels the third figure properly.
```

```
axis image
```

```
grid on
```

```
title('Mean radius with respect to s','fontsize',12)
```

```
xlabel('Mean radius (mm)')
```

```
ylabel('Longitudinal direction s (mm)')
```

```
clear j m
```

Appendix B.6. step_5.m of the developed centerline algorithm

```
perp2dotN=zeros(length(perp2),length(s),3); %contains dot product of perp2 with N2 and N3
depending on the 2nd or 3rd structured array in. The first structured array is empty
theta=zeros(length(perp2),length(s)); %contains the angle theta in radians that the perpendicular
vector makes with the N2 vector.
```

```
k=size(perp2);
```

```
for m=1:k(2)%a series of conditions and inverse tangent function formulas to determine which
angle theta should be assigned to which perpendicular vector. The perpendicular plane was
divided up into four different regions that had their own conditions and formulas.
```

```
for j=1:k(1)
```

```
perp2norm =
[perp2(j,m,1)/norm([perp2(j,m,1),perp2(j,m,2),perp2(j,m,3)]),perp2(j,m,2)/norm([perp2(j,m,1),p
erp2(j,m,2),perp2(j,m,3)]),perp2(j,m,3)/norm([perp2(j,m,1),perp2(j,m,2),perp2(j,m,3)]];
N2norm = [N2(1,m,1),N2(1,m,2),N2(1,m,3)];
N3norm = [N3(1,m,1),N3(1,m,2),N3(1,m,3)];
```

```
%
perp2dotN(j,m,2)=(N2(1,m,1))*(perp2(j,m,1)/norm([perp2(j,m,1),perp2(j,m,2),perp2(j,m,3)]))+
(N2(1,m,2))*(perp2(j,m,2)/norm([perp2(j,m,1),perp2(j,m,2),perp2(j,m,3)]))+
(N2(1,m,3))*(perp2(j,m,3)/norm([perp2(j,m,1),perp2(j,m,2),perp2(j,m,3)]));
```

```
%
perp2dotN(j,m,3)=(N3(1,m,1))*(perp2(j,m,1)/norm([perp2(j,m,1),perp2(j,m,2),perp2(j,m,3)]))+
(N3(1,m,2))*(perp2(j,m,2)/norm([perp2(j,m,1),perp2(j,m,2),perp2(j,m,3)]))+
(N3(1,m,3))*(perp2(j,m,3)/norm([perp2(j,m,1),perp2(j,m,2),perp2(j,m,3)]));
```

```
perp2dotN(j,m,2)=dot(N2norm,perp2norm);
perp2dotN(j,m,3)=dot(N3norm,perp2norm);
perp2dotN(j,m,4)=dot(-N2norm,perp2norm);
perp2dotN(j,m,5)=dot(-N3norm,perp2norm);
```

```
if radius(j,m)~=0
```

```
if perp2dotN(j,m,2) == 1
theta(j,m) = 0;
```

```
elseif perp2dotN(j,m,3) == 1
theta(j,m) = pi/2;
```

```
elseif perp2dotN(j,m,4) == -1
theta(j,m) = pi
```

```
elseif perp2dotN(j,m,5) == -1
```

Appendix B.6 (cont'd)

```

    theta(j,m) = 3*(pi/2);

elseif perp2dotN(j,m,2) > 0 && perp2dotN(j,m,3) > 0
    theta(j,m) = acos(perp2dotN(j,m,2));

elseif perp2dotN(j,m,2) < 0 && perp2dotN(j,m,3) > 0
    theta(j,m) = acos(perp2dotN(j,m,2));

elseif perp2dotN(j,m,2) > 0 && perp2dotN(j,m,3) < 0
    theta(j,m) = -acos(perp2dotN(j,m,2)) + (2*pi);

elseif perp2dotN(j,m,2) < 0 && perp2dotN(j,m,3) < 0
    theta(j,m) = -acos(perp2dotN(j,m,2)) + (2*pi);

else
end
else
end
end
end
end

%% Graph r(theta) along an s axis in 3D, fit an approximated surface over it

j=size(perp2);
snew=zeros(j(1),j(2)); %new array s that has an s value in each place holder that a radius of a
perp vector would appear.
for m=1:j(2)
    snew(:,m)=s(m);
end
num_data=0;

% figure

for j=1:length(s) %Graph the radius wrt theta along an s axis to represent the 3D surface with a
straightened centerline and split about the N2 vector.
    for m=1:length(perp2)
        if theta(m,j)~=0
            num_data=num_data+1;
            % plot3((theta(m,j)),snew(m,j),radius(m,j),'r')
            A{i,4}(num_data,1)=snew(m,j);
            A{i,4}(num_data,2)=theta(m,j);
            A{i,4}(num_data,3)=radius(m,j);
        }
    }
% hold on
End

```

Appendix B.6 (cont'd)

```
    end
end

% %Manipulates and labels the fourth figure properly.
% title('Raw data', 'fontsize', 12)
% xlabel('Angle theta (rad)')
% ylabel('Longitudinal distance s (mm)')
% zlabel('Radius (mm)')
% set(gca, 'XTick', 0:pi/4:2*pi)
% grid on

%% Clearing variables

clear N2norm N3norm j k m perp2dotN perp2norm
```

Appendix B.7. step_6a of the developed approximation code to determine fitting coefficients

```

function [LSE] = step6a(beta)

global s num_data A i n_eta n_theta

n_node = (n_eta+1)*(n_theta);
node = zeros(n_node,2);
dy = s(end)/n_eta;
dx = (2*pi)/n_theta;

count = 0;
for m=1: n_eta+1
    if m== (n_eta+1)
        y_node = s(end);
    else
        y_node = (m-1)*dy;
    end
    for j=1:n_theta

        x_node = (j-1)*dx;
        count = count+1;
        node(count, 1) = x_node;
        node(count, 2) = y_node;
    end
end

K = zeros(n_node, n_node);
F = zeros(n_node, 1);

for p=1:num_data
    zeta = A{i,4}(p,1);
    theta = A{i,4}(p,2);
    for k = 1: n_node
        x0_k=[node(k,2), node(k,1)];

        ds = abs(zeta-x0_k(1));
        dtheta = min( abs(theta-x0_k(2)), 2*pi-abs(theta-x0_k(2)));
        phi_k = exp( -beta(1)*ds^2-beta(2)*dtheta^2);

        F(k,1)=F(k,1)+phi_k*A{i,4}(p,3);
    end
    for n=1:n_node
        x0_n=[node(n,2), node(n,1)];

        ds = abs(zeta-x0_n(1));
        dtheta = min( abs(theta-x0_n(2)), 2*pi-abs(theta-x0_n(2)));
    end
end

```

Appendix B.7 (cont'd)

```

    phi_n = exp( -beta(1)*ds^2-beta(2)*dtheta^2);

    K(k,n)=K(k,n)+phi_k*phi_n;
end
end
end

alpha = K\F;

n_plot_theta =length(s);
n_plot_s = length(s);
s2=0;
theta=0;
data_predict = zeros(size(A{1,4},1), size(A{1,4},2));
count=0;

for m=1: length(A{i,4})
    s2=A{i,4}(m,1);
    theta=A{i,4}(m,2);
    approx=0.0;
    for k=1:n_node
        x0=[node(k,2), node(k,1)];
        ds2 = abs(s2-x0(1));
        dtheta2 = min( abs(theta-x0(2)), 2*pi-abs(theta-x0(2)));
        phi_k = exp( -beta(1)*ds2^2-beta(2)*dtheta2^2);
        approx = approx+ alpha(k)*phi_k;
    end
    if approx < 0

approx = 0;
    end
    count=count+1;
    data_predict(count, 1) = theta;
    data_predict(count, 2) = s2;
    data_predict(count, 3) = approx;
end

C{i,1}(:,1)=data_predict(:,2);
C{i,1}(:,2)=data_predict(:,1);
C{i,1}(:,3)=data_predict(:,3);
C{i,1}(1,4)=n_eta;
C{i,1}(1,5)=n_theta;

D{i,1} = zeros(size(A{1,4},1), size(A{1,4},2));

```

Appendix B.7 (cont'd)

```
D{i,1}(:,1) = A{i,4}(:,1);
```

```
D{i,1}(:,2) = A{i,4}(:,2);
```

```
D{i,1}(1,4)=n_eta;
```

```
D{i,1}(1,5)=n_theta;
```

```
for j = 1 : length(A{i,4})
```

```
    D{i,1}(j,3) = C{i,1}(j,3) - A{i,4}(j,3);
```

```
end
```

```
abs_err = abs(mean(D{i,1}(:,3)));
```

```
D{i,1}(1,6)=abs_err;
```

```
LSE = sum(D{i,1}(:,3).^2);
```

Appendix B.8. step_6 of the developed approximation code

```
%%

global s num_data A i n_eta n_theta
n_eta = 10;
n_theta = 10;
options = optimset('Display','iter');
beta0 = [.9/100 1.5];
[beta, fval] = fminsearch(@step6a,beta0,options)

% eta_shapes = [1,2,3,4,5,6,7,8,9,10];
% theta_shapes = [1,2,3,4,5,6,7,8,9,10];
%
% for iii = 1:length(eta_shapes)
%   for jjj = 1:length(theta_shapes)
%     global s num_data A i n_eta n_theta
%     n_eta = eta_shapes(iii);
%     n_theta = theta_shapes(jjj);
%     options = optimset('Display','iter');
%     beta0 = [.9/100 1.5];
%     [beta, fval] = fminsearch(@step6a,beta0,options)
%     kkk(iii,jjj)= fval
%   end
% end

%% Surface Approximation

%Number of base functions.

C_count = 0;

for n_eta = n_eta
  for n_theta = n_theta

    C_count = C_count + 1;

    n_node = (n_eta+1)*(n_theta);
    node = zeros(n_node,2);
    dy = s(end)/n_eta;
    dx = (2*pi)/n_theta;

    count = 0;
    for m=1: n_eta+1
      if m== (n_eta+1)
```


Appendix B.8 (cont'd)

```

        y_node = s(end);
    else
        y_node = (m-1)*dy;
    end
    for j=1:n_theta

        x_node = (j-1)*dx;
        count = count+1;
        node(count, 1) = x_node;
        node(count, 2) = y_node;
    end
end

K = zeros(n_node, n_node);
F = zeros(n_node, 1);

for p=1:num_data
    zeta = A{i,4}(p,1);
    theta = A{i,4}(p,2);
    for k = 1: n_node
        x0_k=[node(k,2), node(k,1)];

        ds = abs(zeta-x0_k(1));
        dtheta = min( abs(theta-x0_k(2)), 2*pi-abs(theta-x0_k(2)));
        phi_k = exp( -beta(1)*ds^2-beta(2)*dtheta^2);

        F(k,1)=F(k,1)+phi_k*A{i,4}(p,3);
    for n=1:n_node
        x0_n=[node(n,2), node(n,1)];

        ds = abs(zeta-x0_n(1));
        dtheta = min( abs(theta-x0_n(2)), 2*pi-abs(theta-x0_n(2)));
        phi_n = exp( -beta(1)*ds^2-beta(2)*dtheta^2);

        K(k,n)=K(k,n)+phi_k*phi_n;
    end
    end
end

alpha = K\F;

% Working method for approximated surface generation

% n_plot_theta =length(s);

```

Appendix B.8 (cont'd)

```
% n_plot_s = length(s);
% ds = s(end)/n_plot_s;
% dtheta = 2*pi/n_plot_theta;
% s2=0;
% theta=0;
% count = 0
% data_predict = zeros((n_plot_theta+1)*(n_plot_s+1), 3);

% for m=1: 1
%   for j=1: n_plot_theta+1
%     s2= (m-1)*ds;
%     theta=(j-1)*dtheta;
%     approx=0.0;
%     for k=1:n_node
%       x0=[node(k,2), node(k,1)];
%       ds2 = abs(s2-x0(1));
%       dtheta2 = min( abs(theta-x0(2)), 2*pi-abs(theta-x0(2)));
%       %       phi_k = basis_cyl(s2, theta, x0, [beta1, beta2]);
%       phi_k = exp( -beta1*ds2^2-beta2*dtheta2^2);
%       approx = approx+ alpha(k)*phi_k;
%     end
%     if approx < 0
%       approx = 0;
%     end
%     count=count+1;
%     data_predict(count, 1) = theta;
%     data_predict(count, 2) = s2;
%     data_predict(count, 3) = approx;
%   end
% end

% My method

n_plot_theta =length(s);
n_plot_s = length(s);
s2=0;
theta=0;
data_predict = zeros(size(A{1,4},1), size(A{1,4},2));
count=0;

for m=1: length(A{i,4})
  s2=A{i,4}(m,1);
  theta=A{i,4}(m,2);
  approx=0.0;
```

Appendix B.8 (cont'd)

```
for k=1:n_node
    x0=[node(k,2), node(k,1)];
    ds2 = abs(s2-x0(1));
    dtheta2 = min( abs(theta-x0(2)), 2*pi-abs(theta-x0(2)));
    phi_k = exp( -beta(1)*ds2^2-beta(2)*dtheta2^2);
    approx = approx+ alpha(k)*phi_k;
end
if approx < 0
    approx = 0;
end
count=count+1;
data_predict(count, 1) = theta;
data_predict(count, 2) = s2;
data_predict(count, 3) = approx;
end
```

```
C{i,C_count}(:,1)=data_predict(:,2);
C{i,C_count}(:,2)=data_predict(:,1);
C{i,C_count}(:,3)=data_predict(:,3);
C{i,C_count}(1,4)=n_eta;
C{i,C_count}(1,5)=n_theta;
```

%Plots the known data and the approximated surface to see how good the fit is.

```
figure
plot3(A{i,4}(:,1), A{i,4}(:,2), A{i,4}(:,3),'r','MarkerSize',4)
grid on
hold on;
plot3(C{i,C_count}(:,1), C{i,C_count}(:,2), C{i,C_count}(:,3),'b','MarkerSize',4)
str_title = sprintf('Approximated (blue) vs. raw (red) for n eta = %d & n theta =
%d',n_eta,n_theta);
title(str_title,'fontsize',12,'fontname','Times')
xlabel('s','fontsize',12,'fontname','Times')
ylabel('\theta (deg)','fontsize',12,'fontname','Times')
zlabel('r (mm)','fontsize',12,'fontname','Times')
```

% Statistics of fit

```
D{i,C_count} = zeros(size(A{i,4},1), size(A{i,4},2));
D{i,C_count}(:,1) = A{i,4}(:,1);
D{i,C_count}(:,2) = A{i,4}(:,2);
D{i,C_count}(1,4)=n_eta;
D{i,C_count}(1,5)=n_theta;
```

Appendix B.8 (cont'd)

```

for j = 1 : length(A{i,4})
    D{i,C_count}(j,3) = C{i,C_count}(j,3) - A{i,4}(j,3);
end

figure
plot3(D{i,C_count}(:,1), D{i,C_count}(:,2), D{i,C_count}(:,3),'g.','MarkerSize',4)
grid on
title('Residuals plot of approximation fit','fontsize',12)
xlabel('s','fontsize',12,'fontname','Times')
ylabel('\theta (deg)','fontsize',12,'fontname','Times')
zlabel('r (mm)','fontsize',12,'fontname','Times')

abs_err = abs(mean(D{i,C_count}(:,3)))
D{i,C_count}(1,6)=abs_err;

clear n_node node dy dx count y_node y_node x_node K F beta1 beta2 hhh zeta theta x0_k
ds dtheta phi_k x0_n phi_n str_hhh alpha n_plot_theta n_plot_s s2 theta data_predict approx x0
ds2 dtheta2 phi_k

end
end

%% Surface Approximation take 2

% %Number of base functions.
%
% C_count = 0;
%
% for n_eta = n_eta
%   for n_theta = n_theta
%
%       C_count = C_count + 1;
%
%       n_node = (n_eta+1)*(n_theta);
%       node = zeros(n_node,2);
%       dy = s(end)/n_eta;
%       dx = (2*pi)/n_theta;
%
%       count = 0;
%       for m=1: n_eta+1
%           if m== (n_eta+1)
%               y_node = s(end);
%           else
%               y_node = (m-1)*dy;

```

Appendix B.8 (cont'd)

```

%     end
%     for j=1:n_theta
%
%         x_node = (j-1)*dx;
%         count = count+1;
%         node(count, 1) = x_node;
%         node(count, 2) = y_node;
%     end
% end
%
% K = zeros(n_node, n_node);
% F = zeros(n_node, 1);
%
% for p=1:num_data
%     zeta = A{i,4}(p,1);
%     theta = A{i,4}(p,2);
%     for k = 1: n_node
%         x0_k=[node(k,2), node(k,1)];
%
%         ds = abs(zeta-x0_k(1));
%         dtheta = min( abs(theta-x0_k(2)), 2*pi-abs(theta-x0_k(2)));
%         phi_k = exp( -beta(1)*ds^2-beta(2)*dtheta^2);
%
%         F(k,1)=F(k,1)+phi_k*A{i,4}(p,3);
%         for n=1:n_node
%             x0_n=[node(n,2), node(n,1)];
%
%             ds = abs(zeta-x0_n(1));
%             dtheta = min( abs(theta-x0_n(2)), 2*pi-abs(theta-x0_n(2)));
%             phi_n = exp( -beta(1)*ds^2-beta(2)*dtheta^2);
%
%             K(k,n)=K(k,n)+phi_k*phi_n;
%         end
%     end
% end
%
% alpha = K\F;
%
% % Working method for approximated surface generation
%
% % n_plot_theta =length(s);
% % n_plot_s = length(s);
% % ds = s(end)/n_plot_s;
% % dtheta = 2*pi/n_plot_theta;

```

Appendix B.8 (cont'd)

```

%     % s2=0;
%     % theta=0;
%     % count = 0
%     % data_predict = zeros((n_plot_theta+1)*(n_plot_s+1), 3);
%
%     % for m=1: 1
%     %     for j=1: n_plot_theta+1
%     %         s2= (m-1)*ds;
%     %         theta=(j-1)*dtheta;
%     %         approx=0.0;
%     %         for k=1:n_node
%     %             x0=[node(k,2), node(k,1)];
%     %             ds2 = abs(s2-x0(1));
%     %             dtheta2 = min( abs(theta-x0(2)), 2*pi-abs(theta-x0(2)));
%     %             phi_k = exp( -beta1*ds2^2-beta2*dtheta2^2);
%     %             approx = approx+ alpha(k)*phi_k;
%     %         end
%     %         if approx < 0
%     %             approx = 0;
%     %         end
%     %         count=count+1;
%     %         data_predict(count, 1) = theta;
%     %         data_predict(count, 2) = s2;
%     %         data_predict(count, 3) = approx;
%     %     end
% end
%
% My method
%
n_plot_theta =length(s);
n_plot_s = length(s);
ds = 1;
theta_div = 200; %Some even number, div per x-sec from 0 - 2*pi
dtheta = (2*pi) / theta_div;
data_predict = zeros(length(s)*(theta_div), length(s)*(theta_div));
count=0;
%
% for j = 1 : length(s)
%     s2 = j-1;
% for m = 1 : theta_div
%     theta = dtheta*m;
%     approx=0.0;
%     for k=1:n_node
%         x0=[node(k,2), node(k,1)];

```

Appendix B.8 (cont'd)

```

%      ds2 = abs(s2-x0(1));
%      dtheta2 = min( abs(theta-x0(2)), 2*pi-abs(theta-x0(2)));
%      phi_k = exp( -beta(1)*ds2^2-beta(2)*dtheta2^2);
%      approx = approx+ alpha(k)*phi_k;
%      end
%      if approx < 0
%          approx = 0;
%      end
%      count=count+1;
%      data_predict(count, 1) = theta;
%      data_predict(count, 2) = s2;
%      data_predict(count, 3) = approx;
%      end
%      end

%      C{i,C_count}(:,1)=data_predict(:,2);
%      C{i,C_count}(:,2)=data_predict(:,1);
%      C{i,C_count}(:,3)=data_predict(:,3);
%      C{i,C_count}(1,4)=n_eta;
%      C{i,C_count}(1,5)=n_theta;
%
%      %Plots the known data and the approximated surface to see how good the fit is.
%
%      figure
%      plot3(A{i,4}(:,1), A{i,4}(:,2), A{i,4}(:,3),'r','MarkerSize',4)
%      grid on
%      hold on;
%      plot3(C{i,C_count}(:,1), C{i,C_count}(:,2), C{i,C_count}(:,3),'b','MarkerSize',4)
%      str_title = sprintf('Approximated (blue) vs. raw (red) for n eta = %d & n theta =
%d',n_eta,n_theta);
%      title(str_title,'fontsize',12,'fontname','Times')
%      xlabel('s (mm)','fontsize',12,'fontname','Times')
%      ylabel('\theta (deg)','fontsize',12,'fontname','Times')
%      zlabel('r (mm)','fontsize',12,'fontname','Times')
%
%      % Statistics of fit
%
%      clear n_node node dy dx count y_node y_node x_node K F beta1 beta2 hhh zeta theta
x0_k ds dtheta phi_k x0_n phi_n str_hhh alpha n_plot_theta n_plot_s s2 theta data_predict
approx x0 ds2 dtheta2 phi_k
%
%      end
%      end
clear abs_err j k m n n_eta n_theta p

```

Appendix B.9. ecc_testing.m code developed for automatic eccentricity testing

```
sc = 0;
k = 0;

for j = 1:length(A{i,4})

    if j == length(A{i,4})

        k = k+1;
        x_img(k,1) = A{i,4}(j,2);
        x_img(k,2) = A{i,4}(j,3);

        x_img(:, :) = sortrows(x_img(:, :), 1);
        x_img(k+1, :) = x_img(1, :);

        kk = 0;

        for l = 1:length(x_img)
            for m = 1:length(x_img)
                kk = kk + 1;

                x_img_1(kk) = x_img(l,1);
                x_img_2(kk) = x_img(l,2);
                x_img_3(kk) = x_img(m,1);
                x_img_4(kk) = x_img(m,2);

                R_d(kk) = sqrt((x_img_2(kk)^2) + (x_img_4(kk)^2) -
(2*x_img_2(kk)*x_img_4(kk)*cos(x_img_1(kk)-x_img_3(kk))));
            end
        end

        [R_max(sc+1), I_R] = max(R_d(:));

        x_img_5 = x_img_1(I_R) + (pi/2);
        x_img_6 = x_img_1(I_R) - (pi/2);

        if x_img_5 > (2*pi)
            x_img_5 = x_img_5 - (2*pi);
        elseif x_img_5 < 0
            x_img_5 = x_img_5 + (2*pi);
        end

        if x_img_6 > (2*pi)
            x_img_6 = x_img_6 - (2*pi);
        elseif x_img_6 < 0
```


Appendix B.9 (cont'd)

```

    x_img_6 = x_img_6 + (2*pi);
end

for l = 1:length(x_img)
    t_1(l) = (abs(x_img_5 - x_img(l))) / x_img(l);
    t_2(l) = (abs(x_img_6 - x_img(l))) / x_img(l);
end

[t_1_val,t_1_ind] = min(t_1(:));
[t_2_val,t_2_ind] = min(t_2(:));

R_min(sc+1) = sqrt((x_img(t_1_ind,2)^2) + (x_img(t_2_ind,2)^2) -
(2*x_img(t_1_ind,2)*x_img(t_2_ind,2)*cos(x_img(t_1_ind,1)-x_img(t_2_ind,1))));

figure('Color',[1 1 1]);
polar(x_img(:,1),x_img(:,2),'b');
axis image;
hold on;
polar([x_img_1(I_R) x_img_3(I_R)],[x_img_2(I_R) x_img_4(I_R)],'r')
polar([x_img(t_1_ind,1) x_img(t_2_ind,1)],[x_img(t_1_ind,2) x_img(t_2_ind,2)],'g')

clear x_img x_img_1 x_img_2 x_img_3 x_img_4 x_img_5 x_img_6 I_R R_d t_1 t_2
t_1_val t_2_val t_1_ind t_2_ind

elseif A{i,4}(j,1) == sc

    k = k+1;
    x_img(k,1) = A{i,4}(j,2);
    x_img(k,2) = A{i,4}(j,3);

elseif A{i,4}(j,1) ~= sc

    x_img(:,:) = sortrows(x_img(:,:),1);
    x_img(k+1,:) = x_img(1,:);

    kk = 0;

    for l = 1:length(x_img)
        for m = 1:length(x_img)
            kk = kk + 1;

            x_img_1(kk) = x_img(l,1);
            x_img_2(kk) = x_img(l,2);
            x_img_3(kk) = x_img(m,1);

```

Appendix B.9 (cont'd)

```
x_img_4(kk) = x_img(m,2);
```

```
    R_d(kk) = sqrt((x_img_2(kk)^2) + (x_img_4(kk)^2) -  
(2*x_img_2(kk)*x_img_4(kk)*cos(x_img_1(kk)-x_img_3(kk))));  
    end  
end
```

```
[R_max(sc+1),I_R] = max(R_d(:));
```

```
x_img_5 = x_img_1(I_R) + (pi/2);  
x_img_6 = x_img_1(I_R) - (pi/2);
```

```
if x_img_5 > (2*pi)  
    x_img_5 = x_img_5 - (2*pi);  
elseif x_img_5 < 0  
    x_img_5 = x_img_5 + (2*pi);  
end
```

```
if x_img_6 > (2*pi)  
    x_img_6 = x_img_6 - (2*pi);  
elseif x_img_6 < 0  
    x_img_6 = x_img_6 + (2*pi);  
end
```

```
for l = 1:length(x_img)  
    t_1(l) = (abs(x_img_5 - x_img(l))) / x_img(l);  
    t_2(l) = (abs(x_img_6 - x_img(l))) / x_img(l);  
end
```

```
[t_1_val,t_1_ind] = min(t_1(:));  
[t_2_val,t_2_ind] = min(t_2(:));
```

```
R_min(sc+1) = sqrt((x_img(t_1_ind,2)^2) + (x_img(t_2_ind,2)^2) -  
(2*x_img(t_1_ind,2)*x_img(t_2_ind,2)*cos(x_img(t_1_ind,1)-x_img(t_2_ind,1))));
```

```
%    figure('Color',[1 1 1]);  
%    polar(x_img(:,1),x_img(:,2),'b');  
%    axis image;  
%    hold on;  
%    polar([x_img_1(I_R) x_img_3(I_R)],[x_img_2(I_R) x_img_4(I_R)],'r')  
%    polar([x_img(t_1_ind,1) x_img(t_2_ind,1)],[x_img(t_1_ind,2)  
x_img(t_2_ind,2)],'g')
```

Appendix B.9 (cont'd)

```
clear x_img x_img_1 x_img_2 x_img_3 x_img_4 x_img_5 x_img_6 I_R R_d t_1 t_2  
t_1_val t_2_val t_1_ind t_2_ind
```

```
    k=1;  
    sc = sc+1;  
    x_img(k,1) = A{i,4}(j,2);  
    x_img(k,2) = A{i,4}(j,3);
```

```
end
```

```
end
```

```
ecc = R_max ./ R_min;
```

```
sc = 0;
```

```
for j = 1:length(A{i,4})  
    if A{i,4}(j,1) == sc  
        A{i,4}(j,6) = ecc(sc+1);  
    elseif A{i,4}(j,1) ~= sc  
        sc = sc+1;  
        A{i,4}(j,6) = ecc(sc+1);  
    end  
end
```

```
clear k kk sc l m R_d
```

Appendix B.10. surf_curv.m code developed for automatic curvature determination

```
%% post fitting curvature

sc = -1;
count = 0;

for j = 1 : length(s)

    sc = sc+1;

    for k = 1 : theta_div

        count = count+1;

        if k == 1

            R1 = C{i,C_count}((sc*theta_div)+theta_div,3);
            R2 = C{i,C_count}((sc*theta_div)+k,3);
            R3 = C{i,C_count}((sc*theta_div)+k+1,3);
            t1 = C{i,C_count}((sc*theta_div)+theta_div,2);
            t2 = C{i,C_count}((sc*theta_div)+k,2);
            t3 = C{i,C_count}((sc*theta_div)+k+1,2);

        elseif k == theta_div

            R1 = C{i,C_count}((sc*theta_div)+k-1,3);
            R2 = C{i,C_count}((sc*theta_div)+k,3);
            R3 = C{i,C_count}((sc*theta_div)+1,3);
            t1 = C{i,C_count}((sc*theta_div)+k-1,2);
            t2 = C{i,C_count}((sc*theta_div)+k,2);
            t3 = C{i,C_count}((sc*theta_div)+1,2);

        else

            R1 = C{i,C_count}((sc*theta_div)+k-1,3);
            R2 = C{i,C_count}((sc*theta_div)+k,3);
            R3 = C{i,C_count}((sc*theta_div)+k+1,3);
            t1 = C{i,C_count}((sc*theta_div)+k-1,2);
            t2 = C{i,C_count}((sc*theta_div)+k,2);
            t3 = C{i,C_count}((sc*theta_div)+k+1,2);

        end

        x1 = R1*cos(t1);
        x2 = R2*cos(t2);
```

Appendix B.10 (cont'd)

$$x3 = R3*\cos(t3);$$

$$y1 = R1*\sin(t1);$$

$$y2 = R2*\sin(t2);$$

$$y3 = R3*\sin(t3);$$

$$m1 = (y2-y1)/(x2-x1);$$

$$m2 = (y3-y2)/(x3-x2);$$

$$xc = (((m1*m2)*(y1-y3)) + (m2*(x1+x2)) - (m1*(x2+x3))) / (2*(m2-m1));$$

$$yc = ((-1/m1)*(xc-((x1+x2)/2))) + ((y1+y2)/2);$$

$$R = \text{sqrt}(((x2-xc)^2) + ((y2-yc)^2));$$

$$C\{i,C_count\}(count,7) = 1/R;$$

clear R1 R2 R3 t1 t2 t3 x1 x2 x3 y1 y2 y3 m1 m2 xc yc R

end

end

APPENDIX C

Results of centerline and surface approximation algorithm performance

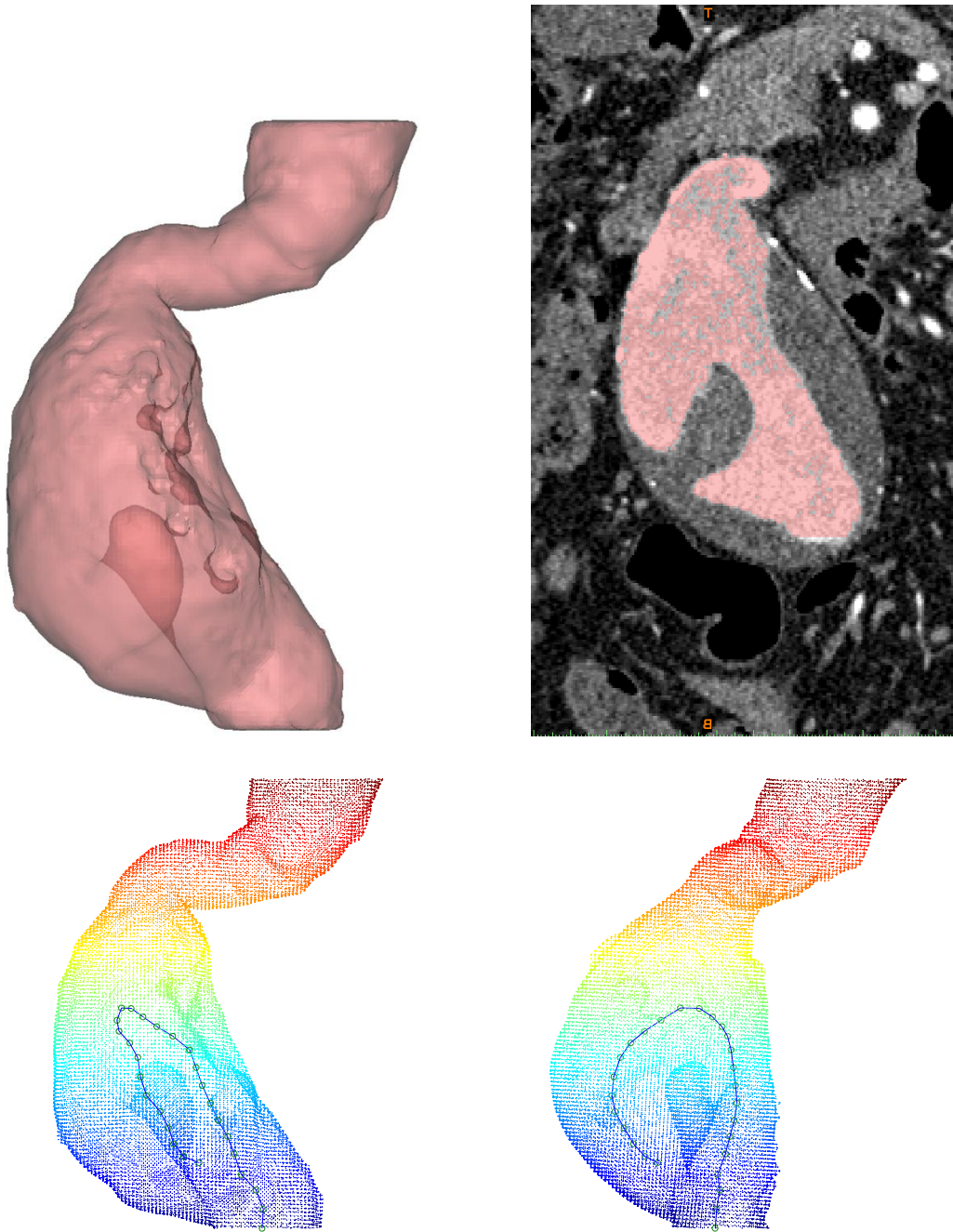


Figure C.1. A 3-D model of the lumen for D3 as seen in the x-z plane (upper-left), a coronal, or x-z, slice from scan D3 (upper-right), an x-z (bottom-left), and a y-z (bottom-right) view of the centerline algorithm results for scan D3. It is clear that scan D3 features a geometric anomaly. This anomaly is highly unusual and tends to force the centerline generation to follow the observed path regardless of input parameters.

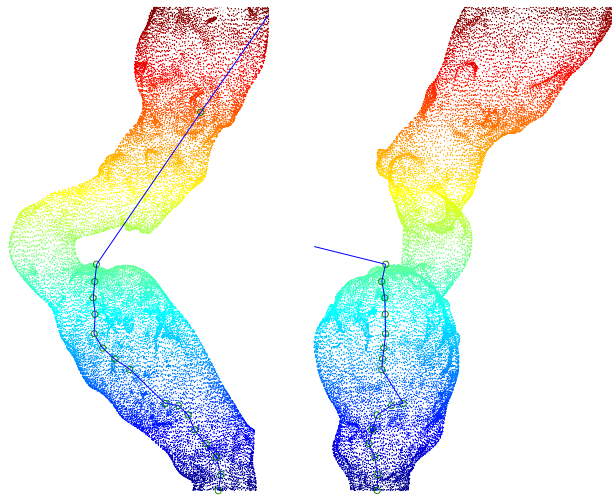


Figure C.2. An x - z (left) and y - z (right) view of the centerline algorithm results from scan F5. If the final approximation of a centerline point differs greatly from the initial guess, the vector between the previous centerline point and current centerline point becomes more extreme. In the case when the vector points directly at a vessel boundary the algorithm will tend to fail. This failure occurs because the minimum distance vector is nearly parallel to the axis normal to the projection plane used for translations, resulting in near-zero translational adjustment vectors. The algorithm assumes that at any given two points the vector between them is relatively parallel to the centerline of the vessel.

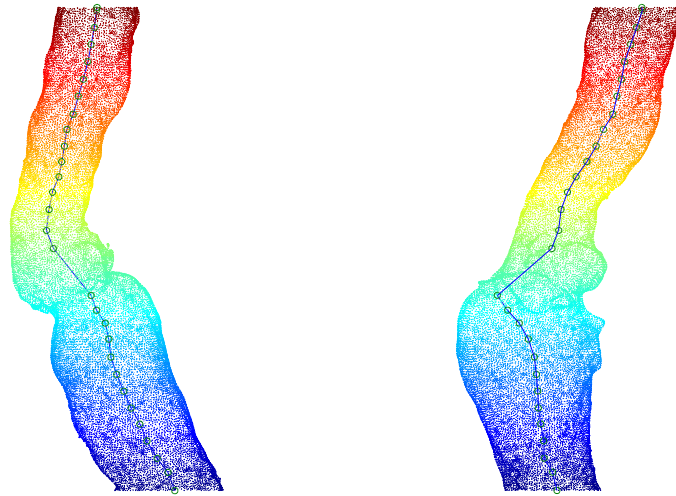


Figure C.3. An x-z (left) and y-z (right) view of the centerline algorithm results from scan H5. If the final approximation of a centerline point differs greatly from the initial guess, the vector between the previous centerline point and current centerline point becomes more extreme. In the case when the vector points directly at a vessel boundary the algorithm will tend to fail. This failure occurs because the minimum distance vector is nearly parallel to the axis normal to the projection plane used for translations, resulting in near-zero translational adjustment vectors. The algorithm assumes that at any given two points the vector between them is relatively parallel to the centerline of the vessel. For this case the algorithm was able to recover, but it resulted in a large erroneous region before recovery.

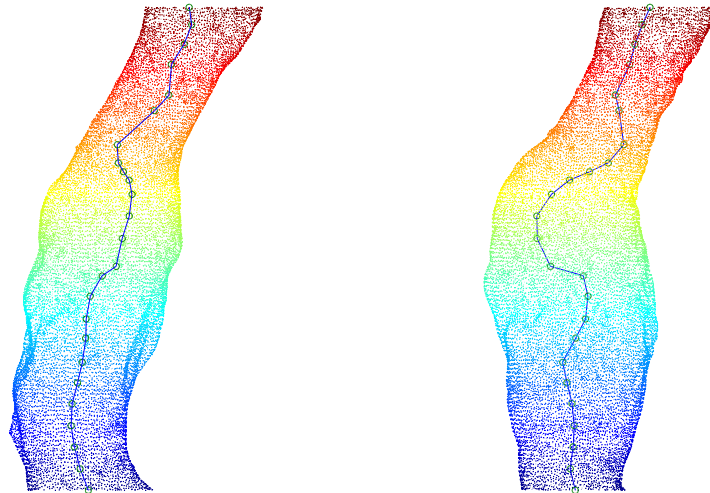


Figure C.4. An x-z (left) and y-z (right) view of the centerline algorithm results from scan K3. It is unclear why the centerline fluctuated from its expected center, but it is clearly erroneous and requires adjustment of operating parameters.

Table C.1. SSE values from surface approximations sorted first by N_η and then by N_θ

combo #	N_η	N_θ	SSE
1	1	1	56956.98
2	1	2	56108.11
3	1	3	56312.28
4	1	4	55796.18
5	1	5	55296.88
6	1	6	55137.28
7	1	7	54892.25
8	1	8	54792.57
9	1	9	54611
10	1	10	54499.47
11	2	1	17815
12	2	2	17125.56
13	2	3	16736.05
14	2	4	16336.73
15	2	5	15430.52
16	2	6	15452.52
17	2	7	15157.9
18	2	8	15176.29
19	2	9	15049
20	2	10	15038.77
21	3	1	11652.39
22	3	2	10549.91
23	3	3	10432.27
24	3	4	9682.665
25	3	5	8776.14
26	3	6	8765.256
27	3	7	8547.275
28	3	8	8489.009
29	3	9	8269.801
30	3	10	8283.601
31	4	1	6487.158
32	4	2	6042.208
33	4	3	5676.069
34	4	4	5211.81
35	4	5	4139.079
36	4	6	4108.915
37	4	7	3904.917
38	4	8	3854.168
39	4	9	3747.15

Table C.1 (cont'd)

40	4	10	3703.919
41	5	1	5955.562
42	5	2	5603.217
43	5	3	5077.259
44	5	4	4528.495
45	5	5	3557.47
46	5	6	3509.808
47	5	7	3253.571
48	5	8	3216.315
49	5	9	3089.596
50	5	10	3044.364
51	6	1	5932.707
52	6	2	5311.066
53	6	3	5100.357
54	6	4	4378.236
55	6	5	3290.206
56	6	6	3269.365
57	6	7	2946.388
58	6	8	2868.631
59	6	9	2752.81
60	6	10	2713.908
61	7	1	6082.858
62	7	2	5466.559
63	7	3	5097.665
64	7	4	4436.855
65	7	5	3181.129
66	7	6	3249.602
67	7	7	2767.998
68	7	8	2699.992
69	7	9	2554.182
70	7	10	2480.305
71	8	1	5563.773
72	8	2	4903.801
73	8	3	4671.616
74	8	4	3896.41
75	8	5	2684.641
76	8	6	2635.93
77	8	7	2306.582
78	8	8	2204.442
79	8	9	2035.634
80	8	10	1974.096

Table C.1 (cont'd)

81	9	1	5612.163
82	9	2	5180.029
83	9	3	4673.011
84	9	4	3833.785
85	9	5	2583.552
86	9	6	2499.712
87	9	7	2132.18
88	9	8	1986.855
89	9	9	1846.959
90	9	10	1729.718
91	10	1	5579.099
92	10	2	5131.247
93	10	3	4651.369
94	10	4	3779.547
95	10	5	2608.741
96	10	6	2532.217
97	10	7	2078.223
98	10	8	1951.817
99	10	9	1823.693
100	10	10	1673.866

Table C.2. SSE approximations sorted based on SSE values

combo #	N_{η}	N_{θ}	SSE
1	1	1	56956.98
2	1	3	56312.28
3	1	2	56108.11
4	1	4	55796.18
5	1	5	55296.88
6	1	6	55137.28
7	1	7	54892.25
8	1	8	54792.57
9	1	9	54611
10	1	10	54499.47
11	2	1	17815
12	2	2	17125.56
13	2	3	16736.05
14	2	4	16336.73
15	2	6	15452.52
16	2	5	15430.52
17	2	8	15176.29
18	2	7	15157.9
19	2	9	15049
20	2	10	15038.77
21	3	1	11652.39
22	3	2	10549.91
23	3	3	10432.27
24	3	4	9682.665
25	3	5	8776.14
26	3	6	8765.256
27	3	7	8547.275
28	3	8	8489.009
29	3	10	8283.601
30	3	9	8269.801
31	4	1	6487.158
32	7	1	6082.858
33	4	2	6042.208
34	5	1	5955.562
35	6	1	5932.707
36	4	3	5676.069
37	9	1	5612.163
38	5	2	5603.217
39	10	1	5579.099
40	8	1	5563.773

Table C.2 (cont'd)

41	7	2	5466.559
42	6	2	5311.066
43	4	4	5211.81
44	9	2	5180.029
45	10	2	5131.247
46	6	3	5100.357
47	7	3	5097.665
48	5	3	5077.259
49	8	2	4903.801
50	9	3	4673.011
51	8	3	4671.616
52	10	3	4651.369
53	5	4	4528.495
54	7	4	4436.855
55	6	4	4378.236
56	4	5	4139.079
57	4	6	4108.915
58	4	7	3904.917
59	8	4	3896.41
60	4	8	3854.168
61	9	4	3833.785
62	10	4	3779.547
63	4	9	3747.15
64	4	10	3703.919
65	5	5	3557.47
66	5	6	3509.808
67	6	5	3290.206
68	6	6	3269.365
69	5	7	3253.571
70	7	6	3249.602
71	5	8	3216.315
72	7	5	3181.129
73	5	9	3089.596
74	5	10	3044.364
75	6	7	2946.388
76	6	8	2868.631
77	7	7	2767.998
78	6	9	2752.81
79	6	10	2713.908
80	7	8	2699.992
81	8	5	2684.641

Table C.2 (cont'd)

82	8	6	2635.93
83	10	5	2608.741
84	9	5	2583.552
85	7	9	2554.182
86	10	6	2532.217
87	9	6	2499.712
88	7	10	2480.305
89	8	7	2306.582
90	8	8	2204.442
91	9	7	2132.18
92	10	7	2078.223
93	8	9	2035.634
94	9	8	1986.855
95	8	10	1974.096
96	10	8	1951.817
97	9	9	1846.959
98	10	9	1823.693
99	9	10	1729.718
100	10	10	1673.866

REFERENCES

REFERENCES

- [1] C. Porth, *Pathophysiology : concepts of altered health states*, 7th ed. Lippincott Williams & Wilkins, 2005.
- [2] M. Jessup and S. Brozena, "Heart Failure," *New England Journal of Medicine*, vol. 348, no. 20, pp. 2007–2018, 2003.
- [3] R. W. Schrier and W. T. Abraham, "Hormones and Hemodynamics in Heart Failure," *New England Journal of Medicine*, vol. 341, no. 8, pp. 577–585, 1999.
- [4] W. D. Clouse, J. W. Hallett Jr, H. V. Schaff, M. M. Gayari, D. M. Ilstrup, and L. J. Melton III, "Improved prognosis of thoracic aortic aneurysms," *JAMA: The Journal of the American Medical Association*, vol. 280, no. 22, pp. 1926–1929, 1998.
- [5] H. W. Kniemeyer, T. Kessler, P. U. Reber, H. B. Ris, H. Hakki, and M. K. Widmer, "Treatment of Ruptured Abdominal Aortic Aneurysm, a Permanent Challenge or a Waste of Resources? Prediction of Outcome Using a Multi-organ-dysfunction Score," *European Journal of Vascular and Endovascular Surgery*, vol. 19, no. 2, pp. 190–196, Feb. 2000.
- [6] T. Mussivand, "Mechanical Circulatory Devices for the Treatment of Heart Failure," *Journal of Cardiac Surgery*, vol. 14, no. 3, pp. 218–228, 1999.
- [7] F. A. Lederle, S. E. Wilson, G. R. Johnson, D. B. Reinke, F. N. Littooy, C. W. Acher, D. J. Ballard, L. M. Messina, I. L. Gordon, E. P. Chute, and others, "Immediate repair compared with surveillance of small abdominal aortic aneurysms," *New England Journal of Medicine*, vol. 346, no. 19, pp. 1437–1444, 2002.
- [8] T. F. US Preventive Services, "Screening for Abdominal Aortic Aneurysm: Recommendation Statement," *Annals of Internal Medicine*, vol. 142, no. 3, pp. 198–202, Feb. 2005.
- [9] J. L. Cronenwett, "Variables that affect the expansion rate and rupture of abdominal aortic aneurysms," *Annals of the New York Academy of Sciences*, vol. 800, no. 1, pp. 56–67, 1996.
- [10] K. Halliday and A. Al-Kutoubi, "Draped Aorta: CT Sign of Contained Leak of Aortic Aneurysms," *Radiology*, vol. 199, no. 1, pp. 41–43, 1996.
- [11] C. Dubost, M. Allary, and N. Oeconomos, "Resection of an aneurysm of the abdominal aorta: reestablishment of the continuity by a preserved human arterial graft, with result after five months," *Archives of Surgery*, vol. 64, no. 3, p. 405, 1952.

- [12] J. C. Parodi, J. C. Palmaz, and H. D. Barone, "Transfemoral intraluminal graft implantation for abdominal aortic aneurysms," *Annals of vascular surgery*, vol. 5, no. 6, pp. 491–499, 1991.
- [13] G. Martufi, E. S. Di Martino, C. H. Amon, S. C. Muluk, and E. A. Finol, "Three-Dimensional Geometrical Characterization of Abdominal Aortic Aneurysms: Image-Based Wall Thickness Distribution," *J. Biomech. Eng.*, vol. 131, no. 6, p. 061015, 2009.
- [14] R. Limet, N. Sakalihassan, and A. Albert, "Determination of the expansion rate and incidence of rupture of abdominal aortic aneurysms," *J Vasc Surg*, vol. 14, no. 4, pp. 540–548, Oct. 1991.
- [15] K. Myers, T. Devine, C. Barras, and G. Self, "Endoluminal Versus Open repair for abdominal aortic aneurysms," in *2nd Virtual Congress of Cardiology*, 2001.
- [16] D. Drury, J. A. Michaels, L. Jones, and L. Ayiku, "Systematic review of recent evidence for the safety and efficacy of elective endovascular repair in the management of infrarenal abdominal aortic aneurysm," *British Journal of Surgery*, vol. 92, no. 8, pp. 937–946, Aug. 2005.
- [17] "Long-Term Outcomes of Immediate Repair Compared with Surveillance of Small Abdominal Aortic Aneurysms," *New England Journal of Medicine*, vol. 346, no. 19, pp. 1445–1452, 2002.
- [18] J. T. Powell, "Final 12-year follow-up of Surgery versus Surveillance in the UK Small Aneurysm Trial," *British Journal of Surgery*, vol. 94, no. 6, pp. 702–708, Jun. 2007.
- [19] C. D. Karkos, U. Mukhopadhyay, I. Papakostas, J. Ghosh, G. J. L. Thomson, and R. Hughes, "Abdominal Aortic Aneurysm: the Role of Clinical Examination and Opportunistic Detection," *European Journal of Vascular and Endovascular Surgery*, vol. 19, no. 3, pp. 299 – 303, 2000.
- [20] D. H. J. Wang, M. S. Makaroun, M. W. Webster, and D. A. Vorp, "Effect of intraluminal thrombus on wall stress in patient-specific models of abdominal aortic aneurysm," *Journal of Vascular Surgery*, vol. 36, no. 3, pp. 598–604, Sep. 2002.
- [21] U. S. A. T. Participants, "Long-term outcomes of immediate repair compared with surveillance of small abdominal aortic aneurysms," *N. Engl. J. Med*, vol. 346, pp. 1445–1452, 2002.
- [22] R. C. Darling, C. R. Messina, D. C. Brewster, and L. W. Ottinger, "Autopsy study of unoperated abdominal aortic aneurysms. The case for early resection," *Circulation*, vol. 56, no. 3 Suppl, 1977.
- [23] G. Giannoglou, G. Giannakoulas, J. Soulis, Y. Chatzizisis, T. Perdikides, N. Melas, G. Parcharidis, and G. Louridas, "Predicting the Risk of Rupture of Abdominal Aortic

Aneurysms by Utilizing Various Geometrical Parameters: Revisiting the Diameter Criterion,” *Angiology*, vol. 57, no. 4, pp. 487–494, Aug. 2006.

- [24] M. L. Raghavan and D. A. Vorp, “Toward a biomechanical tool to evaluate rupture potential of abdominal aortic aneurysm: identification of a finite strain constitutive model and evaluation of its applicability,” *Journal of biomechanics*, vol. 33, no. 4, pp. 475–482, 2000.
- [25] B. J. Doyle, A. Callanan, P. E. Burke, P. A. Grace, M. T. Walsh, D. A. Vorp, and T. M. McGloughlin, “Vessel asymmetry as an additional diagnostic tool in the assessment of abdominal aortic aneurysms,” *Journal of Vascular Surgery*, vol. 49, no. 2, pp. 443–454, 2009.
- [26] M. L. Raghavan, D. A. Vorp, M. P. Federle, M. S. Makaroun, and M. W. Webster, “Wall stress distribution on three-dimensionally reconstructed models of human abdominal aortic aneurysm,” *Journal of Vascular Surgery*, vol. 31, no. 4, pp. 760–769, 2000.
- [27] E. Georgakarakos, C. V. Ioannou, Y. Kamarianakis, Y. Papaharilaou, T. Kostas, E. Manousaki, and A. N. Katsamouris, “The role of geometric parameters in the prediction of abdominal aortic aneurysm wall stress,” *European Journal of Vascular and Endovascular Surgery*, vol. 39, no. 1, pp. 42–48, 2010.
- [28] L. Speelman, A. Bohra, E. M. H. Bosboom, G. W. H. Schurink, F. N. van de Vosse, M. S. Makaroun, and D. A. Vorp, “Effects of wall calcifications in patient-specific wall stress analyses of abdominal aortic aneurysms,” *Journal of Biomechanical Engineering*, vol. 129, pp. 105–109, 2007.
- [29] J. Shum, G. Martufi, E. Martino, C. B. Washington, J. Grisafi, S. C. Muluk, and E. A. Finol, “Quantitative Assessment of Abdominal Aortic Aneurysm Geometry,” *Ann Biomed Eng*, vol. 39, no. 1, pp. 277–286, Oct. 2010.
- [30] M. Xenos, S. Rambhia, Y. Alemu, S. Einav, J. J. Ricotta, N. Labropoulos, A. Tassiopoulos, and D. Bluestein, “Mimics Based Image Reconstruction Augments Diagnosis and Management of Vascular Pathologies: A Study of Ruptured Abdominal Aortic Aneurysms.”
- [31] D. Bluestein, K. Dumont, M. De Beule, J. Ricotta, P. Impellizzeri, B. Verheghe, and P. Verdonck, “Intraluminal thrombus and risk of rupture in patient specific abdominal aortic aneurysm - FSI modelling,” *Comp. Methods in Biomechanics & Biomedical Eng.*, vol. 12, no. 1, pp. 73–81, Feb. 2009.
- [32] M. F. Fillinger, M. L. Raghavan, S. P. Marra, J. L. Cronenwett, and F. E. Kennedy, “In vivo analysis of mechanical wall stress and abdominal aortic aneurysm rupture risk,” *J Vasc Surg*, vol. 36, no. 3, pp. 589–597, 2002.

- [33] B. Wolters, M. C. M. Rutten, G. W. H. Schurink, U. Kose, J. De Hart, and F. N. Van De Vosse, "A patient-specific computational model of fluid–structure interaction in abdominal aortic aneurysms," *Medical engineering & physics*, vol. 27, no. 10, pp. 871–883, 2005.
- [34] J. H. Leung, A. R. Wright, N. Cheshire, J. Crane, S. A. Thom, A. D. Hughes, and Y. Xu, "Fluid structure interaction of patient specific abdominal aortic aneurysms: a comparison with solid stress models," *BioMedical Engineering OnLine*, vol. 5, no. 1, p. 33, 2006.
- [35] Y. Papaharilaou, J. A. Ekaterinaris, E. Manousaki, and A. N. Katsamouris, "A decoupled fluid structure approach for estimating wall stress in abdominal aortic aneurysms," *Journal of biomechanics*, vol. 40, no. 2, pp. 367–377, 2007.
- [36] A. Borghi, N. B. Wood, R. H. Mohiaddin, and X. Y. Xu, "3D geometric reconstruction of thoracic aortic aneurysms," *Biomedical engineering online*, vol. 5, no. 1, p. 59, 2006.
- [37] D. A. Steinman, J. S. Milner, C. J. Norley, S. P. Lownie, and D. W. Holdsworth, "Image-based computational simulation of flow dynamics in a giant intracranial aneurysm," *American journal of neuroradiology*, vol. 24, no. 4, pp. 559–566, 2003.
- [38] J. P. V. Geest, D. H. Wang, S. R. Wisniewski, M. S. Makaroun, and D. A. Vorp, "Towards a noninvasive method for determination of patient-specific wall strength distribution in abdominal aortic aneurysms," *Annals of Biomedical Engineering*, vol. 34, pp. 1098–1106, 2006.
- [39] D. A. Vorp and J. P. Geest, "Biomechanical determinants of abdominal aortic aneurysm rupture," *Arterioscler. Thromb. Vasc. Biol.*, vol. 25, pp. 1558–1566, 2005.
- [40] B. J. Doyle, T. J. Corbett, A. Callanan, M. T. Walsh, D. A. Vorp, and T. M. McGloughlin, "An experimental and numerical comparison of the rupture locations of an abdominal aortic aneurysm," *Journal Information*, vol. 16, no. 3, 2009.
- [41] J. Swedenborg and P. Eriksson, "The Intraluminal Thrombus as a Source of Proteolytic Activity," *Annals of the New York Academy of Sciences*, vol. 1085, no. 1, pp. 133–138, Nov. 2006.
- [42] Y. G. Wolf, W. S. Thomas, F. J. Brennan, W. G. Goff, M. J. Sise, and E. F. Bernstein, "Computed tomography scanning findings associated with rapid expansion of abdominal aortic aneurysms," *J Vasc Surg*, vol. 20, no. 4, pp. 529–538, Oct. 1994.
- [43] J. W. Hinnen, O. H. . Koning, M. J. . Visser, and H. J. Van Bockel, "Effect of intraluminal thrombus on pressure transmission in the abdominal aortic aneurysm," *Journal of vascular surgery*, vol. 42, no. 6, pp. 1176–1182, 2005.
- [44] D. A. Vorp, M. L. Raghavan, and M. W. Webster, "Mechanical wall stress in abdominal aortic aneurysm: influence of diameter and asymmetry," *Journal of Vascular Surgery*, vol. 27, no. 4, pp. 632–639, 1998.

- [45] P. N. Watton, N. A. Hill, and M. Heil, “A mathematical model for the growth of the abdominal aortic aneurysm,” *Biomechanics and Modeling in Mechanobiology*, vol. 3, no. 2, pp. 98–113, Sep. 2004.
- [46] C. Kleinstreuer and Z. Li, “Analysis and computer program for rupture-risk prediction of abdominal aortic aneurysms,” *Biomed Eng Online*, vol. 5, p. 19, 2006.
- [47] M. S. Sacks, D. A. Vorp, M. L. Raghavan, M. P. Federle, and M. W. Webster, “In vivo three-dimensional surface geometry of abdominal aortic aneurysms,” *Annals of biomedical engineering*, vol. 27, no. 4, pp. 469–479, 1999.
- [48] J. Shum, A. Xu, I. Chatnuntawech, and E. A. Finol, “A Framework for the Automatic Generation of Surface Topologies for Abdominal Aortic Aneurysm Models,” *Annals of Biomedical Engineering*, vol. 39, no. 1, pp. 249–259, Sep. 2010.
- [49] G. Choi, C. P. Cheng, N. M. Wilson, and C. A. Taylor, “Methods for Quantifying Three-Dimensional Deformation of Arteries due to Pulsatile and Nonpulsatile Forces: Implications for the Design of Stents and Stent Grafts,” *Annals of Biomedical Engineering*, vol. 37, no. 1, pp. 14–33, Nov. 2008.
- [50] C. B. Washington, J. Shum, S. C. Muluk, and E. A. Finol, “The Association of Wall Mechanics and Morphology: A Case Study of Abdominal Aortic Aneurysm Growth,” *Journal of biomechanical engineering*, vol. 133, p. 104501, 2011.
- [51] A. Long, L. Rouet, J. S. Lindholt, and E. Allaire, “Measuring the Maximum Diameter of Native Abdominal Aortic Aneurysms: Review and Critical Analysis,” *European Journal of Vascular and Endovascular Surgery*, Feb. 2012.
- [52] B. S. Ferket, N. Grootenboer, E. B. Colkesen, J. J. Visser, M. R. H. M. van Sambeek, S. Spronk, E. W. Steyerberg, and M. G. M. Hunink, “Systematic review of guidelines on abdominal aortic aneurysm screening,” *J Vasc Surg*, Feb. 2011.
- [53] J. T. Powell, M. J. Sweeting, L. C. Brown, S. M. Gotensparre, F. G. Fowkes, and S. G. Thompson, “Systematic review and meta-analysis of growth rates of small abdominal aortic aneurysms,” *British Journal of Surgery*, vol. 98, no. 5, pp. 609–618, May 2011.
- [54] R. Acharya, R. Wasserman, J. Stevens, and C. Hinojosa, “Biomedical imaging modalities: a tutorial,” *Computerized Medical Imaging and Graphics*, vol. 19, no. 1, pp. 3–25, 1995.
- [55] Olaf T. von Ramm and Stephen W. Smith, “Three-dimensional Imaging System,” U.S. Patent 469443415-Sep-1987.
- [56] J. A. Ten Bosch, E. V. Rouwet, C. T. . Peters, L. Jansen, H. J. . Verhagen, M. H. Prins, and J. A. . Teijink, “Contrast-enhanced ultrasound versus computed tomographic angiography

for surveillance of endovascular abdominal aortic aneurysm repair,” *Journal of Vascular and Interventional Radiology*, vol. 21, no. 5, pp. 638–643, 2010.

- [57] N. Grøndal, M. B. Bramsen, M. D. Thomsen, C. B. Rasmussen, and J. S. Lindholt, “The Cardiac Cycle is a Major Contributor to Variability in Size Measurements of Abdominal Aortic Aneurysms by Ultrasound,” *European Journal of Vascular and Endovascular Surgery*, 2011.
- [58] A. Abbas, A. Smith, M. Cecelja, and M. Waltham, “Assessment of the accuracy of AortaScan for detection of abdominal aortic aneurysm (AAA),” *European Journal of Vascular and Endovascular Surgery*, 2011.
- [59] *Mimics Medical Imaging Software*. Leuven, Belgium: Materialise, Inc.
- [60] S. Zeinali-Davarani, L. G. Raguin, D. A. Vorp, and S. Baek, “Identification of in vivo material and geometric parameters of a human aorta: toward patient-specific modeling of abdominal aortic aneurysm,” *Biomechanics and Modeling in Mechanobiology*, vol. 10, no. 5, pp. 689–699, Nov. 2010.
- [61] *MATLAB*. MathWorks, 2010.
- [62] S.-W. Lee, L. Antiga, J. D. Spence, and D. A. Steinman, “Geometry of the Carotid Bifurcation Predicts Its Exposure to Disturbed Flow,” *Stroke*, vol. 39, no. 8, pp. 2341–2347, Jun. 2008.
- [63] J. B. Thomas, “Variation in the Carotid Bifurcation Geometry of Young Versus Older Adults: Implications for Geometric Risk of Atherosclerosis,” *Stroke*, vol. 36, no. 11, pp. 2450–2456, Oct. 2005.
- [64] D. A. Steinman, J. B. Thomas, H. M. Ladak, J. S. Milner, B. K. Rutt, and J. D. Spence, “Reconstruction of carotid bifurcation hemodynamics and wall thickness using computational fluid dynamics and MRI,” *Magnetic Resonance in Medicine*, vol. 47, no. 1, pp. 149–159, Jan. 2002.